UNIVERSITÀ
DEGLI STUDI
DI PADOVA

Sede Amministrativa: Università degli Studi di Padova

Dipartimento di Ingegneria Industriale

SCUOLA DI DOTTORATO DI RICERCA IN: INGEGNERIA INDUSTRIALE
INDIRIZZO: INGEGNERIA CHIMICA, DEI MATERIALI E DELLA PRODUZIONE
CICLO XXVII

HOT BULK DAMAGE MODELLING OF PRECIPITATION HARDENED AA6082 ALUMINIUM ALLOY

Direttore della Scuola: Ch.mo Prof. Paolo Colombo
Coordinatore d'indirizzo: Ch.mo Prof. Enrico Savio
Supervisore: Ch.ma Prof.ssa Stefania Bruschi

Dottorando: Michele Francesco Novella

Ai miei genitori

TABLE OF CONTENTS

ACKNOWLEDGEMENTS

First of all I want to express my sincerest gratitude to my Supervisor, Prof. Stefania Bruschi, whose help in these years has been fundamental and whose advice and scientific insight have been a needful landmark.
And second, but not in importance, I want to say thanks to Prof. Andrea Ghiotti, not only for his leadership and his capability to bring out the best of me, but also because for many aspects he taught me what being a good engineer means.
A big thanks to my colleagues, for their selfless support and for the fundamental recreational moments at lunch during these years.
My gratitude goes naturally to the two pillars of my life: my family and my friends. Thank you for having always made me feel that you were there.
My last thanks goes to Lisa, the most beautiful surprise of these years, because she has shown me it is not as I thought.

Michele Francesco Novella

Padova, January 2015

ABSTRACT

Among the bulk metal forming processes hot forging is often the only option if large reductions of the forging load are required or if the material formability needs to be significantly increased or even if specific thermally-induced microstructural changes are needed to take place during the deformation process. Moreover it still retains at some extent the positive features of the cold forging processes: high production rates, complex final shapes attainable and little to no material waste.

Hot forging is therefore used for the production of large parts, with complex shapes and especially when using materials characterized by low formability and high toughness at room temperature or if particular microstructural characteristics are required. It is worth to be underlined that these are often the features of the innovative metal alloys that have been increasingly being used in the last decade and namely: Mg alloys, Al alloys, Ti alloys and superalloys.

Finite Element metal forming numerical simulation has become an increasingly important process optimization tool, due to the growing computational power available at reduced costs, which spread it in the industrial world. Its use allows reducing process design time and prototyping costs as well as long and expensive plant downtimes for process variable tuning.

For all these reasons hot forging has become a strategic process and its accurate numerical simulation is encountering great industrial interest. One of its main targets is the determination of the maximum strain that the material can undergo during the deformation process, since it is strictly related with both the final shape and the surface

quality of the manufactured part. In this sense hot formability modelling provides a meaningful example of a topic which is both of great scientific and industrial interest.
From the scientific point of view ductile damage modelling has been developed at first for cold processes, for which crack formation is usually a major issue. Last decade research efforts focused on the development of more advanced fracture criteria, keeping into account a complete characterization of the stress state dependency of formability. However the complex analytical formulation of these criteria and their expensive experimental calibration kept them de facto away from practical industrial use. On the other hand hot formability modelling was traditionally addressed by direct application of the conventional cold fracture criteria, under the implicit assumption of isothermal conditions. This approach has evident limits since it does not account for temperature influence on material formability and it does not even provide any physical insight on the different fracture mechanisms that can develop as temperature changes. In recent years some research efforts have been performed on a deeper investigation upon this point: experimental formability campaigns on different metal alloys were carried out in order to assess the temperature and strain rate influence, while some analytical models were proposed in order to describe the damage evolution at high temperature and in particular the onset of the so-called "hot shortness". However these models are still quite simple and can describe only a limited variety of formability trends, losing in accuracy once complex microstructural phenomena take place. Moreover their validation has been done with simple laboratory tests and not with real processes industrial trials in which non-uniform thermo-mechanical conditions are present and the material can evolve through fracture mode-changing regimes.
The objective of this work is the elaboration of a novel approach to hot ductile fracture modelling, capable to represent accurately the formability evolution of a metal alloy as a function of both the main thermo-mechanical variables and its physical and microstructural characteristics, yet providing a tool simple enough to be of industrial utility. To this aim the hot cross wedge rolling of a precipitation hardened aluminium alloy was taken as industrial reference case, since it is an innovative and non-standard forging process which entails variable and non-homogeneous thermo-mechanical conditions. The study case is of remarkable interest since it has a narrow process temperature window, being limited at the top by Mannesmann-type axial cracking onset and at the bottom by unwanted grain coarsening. Moreover the metal alloy used, the AA6082-T6, has the microstructural features, namely the intermetallic precipitates, that make it a good example of a metal alloy of wide industrial use, that during forming can undergo complex microstructural changes.
A hot tensile test campaign was performed on a wide range of thermo-mechanical conditions and the results highlighted an unexpected negative strain rate influence on formability. Fractographic and micro-chemical analysis were then performed in order to

assess the microstructural reasons of this behaviour and finally two approaches to the material formability modelling were proposed and calibrated extending to hot conditions the classic Oyane-Sato fracture criterion. The first one consists on the empirical calibration of the criterion by means of a bi-linear interpolation of the experimental data, while the second one entails a physically-based analytical formulation of the material fracture locus, which has also the advantage of being of easier calibration. These models were then validated on the cross wedge rolling process simulation by comparison with the industrial trials results and the outcomes were critically assessed.

SOMMARIO

Tra i processi di formatura massivi di materiali metallici, la forgiatura a caldo è spesso l'unica opzione nei casi in cui siano richieste forti riduzioni del carico di forgiatura o se la formabilità del materiale deve essere notevolmente aumentata o anche se risulta necessario ottenere durante il processo di deformazione determinate modifiche microstrutturali indotte termicamente. Inoltre essa conserva ancora in certa misura le caratteristiche positive dei processi di forgiatura a freddo: alta produttività, possibilità di realizzare forme finali complesse e scarto di materiale ridotto o inesistente.
La forgiatura a caldo viene quindi utilizzata per la produzione di pezzi di grandi dimensioni, di forma complessa e soprattutto quando si utilizzano materiali caratterizzati da bassa formabilità ed elevata tenacità o se particolari caratteristiche microstrutturali sono richieste. Vale la pena di sottolineare che queste sono spesso le caratteristiche delle leghe metalliche innovative che sono state sempre più utilizzate negli ultimi dieci anni e precisamente: leghe di magnesio, alluminio, titanio e superleghe.
La simulazione numerica agli Elementi Finiti di processi di formatura di materiali metallici è diventata nell'ultimo decennio uno strumento sempre più importante per l'ottimizzazione di processo, grazie alla maggiore potenza di calcolo disponibile a costi ridotti, che ha permesso la sua diffusione nel mondo industriale. Il suo utilizzo permette di ridurre i tempi di progettazione del processo ed i costi di prototipazione ed anche lunghi e costosi tempi di fermo impianto per la taratura delle variabili di processo.
Per tutti questi motivi la forgiatura a caldo è diventata un processo strategico e la sua accurata simulazione numerica incontra grande interesse industriale. Uno dei suoi obiettivi principali è la determinazione della massima deformazione che il materiale può

subire durante il processo deformativo, dal momento che essa è strettamente legata sia con la forma finale che con la qualità superficiale del componente prodotto. In questo senso la modellazione della formabilità a caldo fornisce un esempio significativo di un argomento che è al tempo stesso di grande interesse scientifico e industriale.

Dal punto di vista scientifico la modellazione del danneggiamento duttile dei materiali è stata originariamente sviluppata per le lavorazioni a freddo, per cui la possibile formazione di cricche è un problema di maggior rilievo. Gli sforzi di ricerca nell'ultimo decennio si sono concentrati sullo sviluppo di criteri di frattura più avanzati, che hanno permesso la caratterizzazione completa dell'influenza dello stato tensionale sulla formabilità. Tuttavia la complessa formulazione analitica di questi criteri e la loro costosa calibrazione sperimentale ne hanno di fatto impedito la diffusione in ambito industriale. D'altra parte la modellazione della formabilità a caldo è stata tradizionalmente affrontata tramite la diretta applicazione dei convenzionali criteri di frattura a freddo, sotto l'ipotesi implicita di condizioni isoterme. Questo approccio presenta evidenti limiti, in quanto non tiene conto dell'influenza della temperatura sulla formabilità del materiale, né permette di intuire il senso fisico dei diversi meccanismi di frattura che possono svilupparsi al variare della temperatura. Negli ultimi anni alcuni sforzi si sono fatti per approfondire quest'ultimo punto: campagne sperimentali di formabilità su diverse leghe metalliche sono state eseguite per valutare l'influenza della temperatura e della velocità di deformazione, mentre alcuni modelli analitici sono stati proposti per descrivere l'evoluzione del danneggiamento ad alte temperature ed in particolare l'insorgere della "fragilità a caldo". Tuttavia questi modelli sono ancora abbastanza semplici e possono descrivere solo una varietà limitata di comportamenti del materiale, perdendo in precisione nel caso avvengano fenomeni microstrutturali complessi. Inoltre la loro validazione è stata effettuata con semplici test di laboratorio e non su reali processi industriali in cui si sviluppano condizioni termo-meccaniche non uniformi e il materiale può evolvere attraverso regimi in cui i meccanismi di frattura sono variabili.

L'obiettivo di questo lavoro è l'elaborazione di un nuovo approccio alla modellazione della frattura duttile a caldo, in grado di rappresentare accuratamente l'evoluzione della formabilità di una lega metallica come funzione sia delle principali variabili termo-meccaniche che delle sue caratteristiche fisiche e microstrutturali, restando al contempo uno strumento sufficientemente semplice da essere di utilità industriale. Per questo scopo è stata presa come caso di riferimento industriale la rullatura trasversale a caldo di una lega di alluminio indurita per precipitazione, dal momento che si tratta di un processo di forgiatura non convenzionale ed innovativo e che comporta condizioni termo-meccaniche variabili e non omogenee. Il caso di studio è di notevole interesse poiché è caratterizzato da una stretta finestra di temperatura di processo, limitata superiormente dall'insorgenza di criccatura assiale per effetto Mannesmann ed inferiormente da un indesiderato ingrossamento della grana cristallina. Inoltre, la lega metallica utilizzata, l'AA6082-T6,

ha delle caratteristiche microstrutturali, vale a dire i precipitati intermetallici, che lo rendono un buon esempio di una lega metallica di largo uso industriale, che durante la formatura può subire variazioni microstrutturali complesse.
Una campagna di prove di trazione a caldo è stata eseguita su un ampio spettro di condizioni termo-meccaniche ed i risultati hanno evidenziato un'inattesa influenza negativa della velocità di deformazione sulla formabilità. Analisi frattografiche e micro-chimiche sono quindi state eseguite al fine di valutare le ragioni microstrutturali di questo comportamento ed infine due approcci alla modellazione della formabilità della lega sono stati proposti e calibrati estendendo alle alte temperature il classico criterio di frattura di Oyane-Sato. Il primo consiste nella calibrazione empirica del criterio mediante interpolazione bi-lineare dei dati sperimentali, mentre il secondo si basa su una formulazione analitica physically-based del fracture locus del materiale, che ha anche il vantaggio di essere di più facile calibrazione. I modelli sono stati poi validati sulla simulazione del processo di rullatura trasversale comparandone i risultati con quelli delle prove industriali e valutandoli in modo critico.

LIST OF FIGURES

LIST OF TABLES

LIST OF SYMBOLS

Greek

γ = Xue ratio [-]

δ_{ij} = Kronecker delta [-]

$\dot{\varepsilon}$ = strain rate [s^{-1}]

$\bar{\varepsilon}$ = Von Mises equivalent strain [-]

ε_i = principal component of the strain tensor [-]

ε_{ij} = cartesian component of the strain tensor [-]

η = stress triaxiality factor [-]

θ = Lode angle [°]

μ_{hyd}, μ_{dev} = Xue model variables [-]

μ, λ = Wilkin's constants [-]

ξ, ρ, θ = Haigh Wasteergard coordinates

$\bar{\sigma}$ = Von Mises equivalent stress [MPa]

σ_a =first principal tension in McClintock model [MPa]

σ_b =second principal tension in McClintock model [MPa]

σ_H = hydrostatic pressure [MPa]

σ_i = principal component of the stress tensor [MPa]

σ_{ij} = cartesian component of the stress tensor [MPa]

σ_{yield} = monoaxial yield stress [MPa]

σ_P = peak stress [MPa]

σ_{eff} = effective stress (due to damage) [MPa]

ϕ = potential of dissipation [W/m^3]

Φ = flow stress function surface [-]

χ = relative ratio of the principal deviatoric stresses [-]

Latin

A = Oyane-Sato coefficient [-]

B_1 = Rice and Tracey first coefficient [-]

B_2 = Rice and Tracey second coefficient [-]

D = damage [-]

D^* = critical damage [-]

$\dot{D}$ = damage rate [s^{-1}]

$\dot{D}_{nucl}$ = damage rate due to voids nucleation [s^{-1}]

$\dot{D}_{growth}$ = damage rate due to voids growth [s^{-1}]

D_{coal} = damage trigger value for coalescence onset [-]

$\tilde{D}$ = Tveegard and Needleman's modified damage [-]

D_{Oy} =Oyane-Sato damage formulation [-]

D^*_{Oy} =Oyane-Sato damage trigger value [-]

E_{eff} = effective Young modulus (due to damage) [MPa]

E = Young modulus [MPa]

h_C = damage reduction factor [-]

K = coalescence damage acceleration factor [-]

l_0 = tensile specimen gauge length [mm]

m = strain rate sensitivity coefficient [-]

$\bar{m}$ = Tresca friction coefficient [-]

n = strain hardening coefficient [-]

Q = viscous flow activation energy [J/mol]

q_1, q_2 = Tveegard and Needleman's flow stress function modification coefficients [-]

R = gas universal constant [kJ/molK]

R = gas universal constant [J/molK]

R_V = triaxiality function [-]

s_{ij} = cartesian component of the stress deviator [MPa]

s_i = principal component of the stress deviator [MPa]

S_0, s_0 = Lemaitre's constants [-]

t = time [s]

T_m = grain boundary precipitates eutectic temperature [K]

T_C = hot shortness temperature [K]

T_{hom} = homologous temperature [-]

T = temperature [K]

V = total volume [mm^3]

V_{voids} = voids volume [mm^3]

v = press translation speed [mm/s]

y = strain energy release rate (per unit damage) [J/m^3]

Z = Zenner hollomon parameter [s^{-1}]

I CHAPTER

INTRODUCTION

I.1 CONTEXT

Bulk metal forging is one of the main manufacturing processes categories and it is used to realize a large variety of products, due to its versatility. It usually implies good up to excellent geometrical tolerances, little to no material waste, high production rates as well as the capability of attaining complex final shapes. On the other hand, it also needs high initial investments on equipment and is then not suitable for little production batches. For all these reasons it is used to produce big amounts of finished or semi-finished components in capital intensive industrial sectors such as domestic products, aerospace, electronics and automotive and has then become a key technology of great industrial interest.

If compared to forging processes carried out at room temperature, hot forging typically entails higher tooling costs, higher energy consumption and less precise geometrical accuracy. Yet it is often the only option if large reductions of the forging load, high material formability or thermally-induced microstructural changes are required. Moreover it still retains at some extent the positive features of the cold forging processes: high production rates, complex final shapes attainable and little to no material waste.

Finite Element (FE) numerical simulation, originally applied to this kind of processes in the late 70s, emerged as an essential research tool in the 90s and spread to common industrial use in the 2000s, thanks to the increasing computational power available at reduced costs and to the diffusion of a series of user friendly commercial codes.

Ductile damage modelling is one of the more important aspects in metal forming FE simulations [1] since an accurate prediction of cracks formation is essential both for process design and control and in particular to attain high-quality and defects-free parts. To this aim the concept of *material formability* has been introduced and modelled by *fracture criteria* that were originally developed for cold forging conditions, since material formability was regarded as a major concern at room temperature and also probably because the more variables involved in hot conditions made it more difficult to be modelled.

However in the last decade *hot formability* has gathered increasing industrial and scientific interest due to:

- the increasing use of new metal alloys with particular thermally-induced microstructural features and behaviours, such as the aluminium and titanium alloys;
- the wider diffusion of hot forging processes in order to obtain near-to-net-shape parts with large dimensions and with complex shapes;

- the increasing demand for high-performance components, in particular in the automotive sector, which must then be formed in hot conditions either because of the use of tougher alloys or because of the need of a stricter control on the resulting microstructure.

I.2 INDUSTRIAL AND SCIENTIFIC PROBLEM

Generally speaking, damage evolution in hot conditions is a complex topic in which, in addition to the influence variables typical of cold conditions, other phenomena occur:

- recrystallization, which does not only affect the material rheological behaviour, but also influences the microstructural defects, which are the void nucleation;
- temperature and strain rate influence on material rheology;
- possible phase changes with corresponding sharp formability variations;
- thermally-induced fracture mode changes and in particular the so-called hot shortness, consisting in a sharp formability drop at high temperatures related to grain boundary weakness.

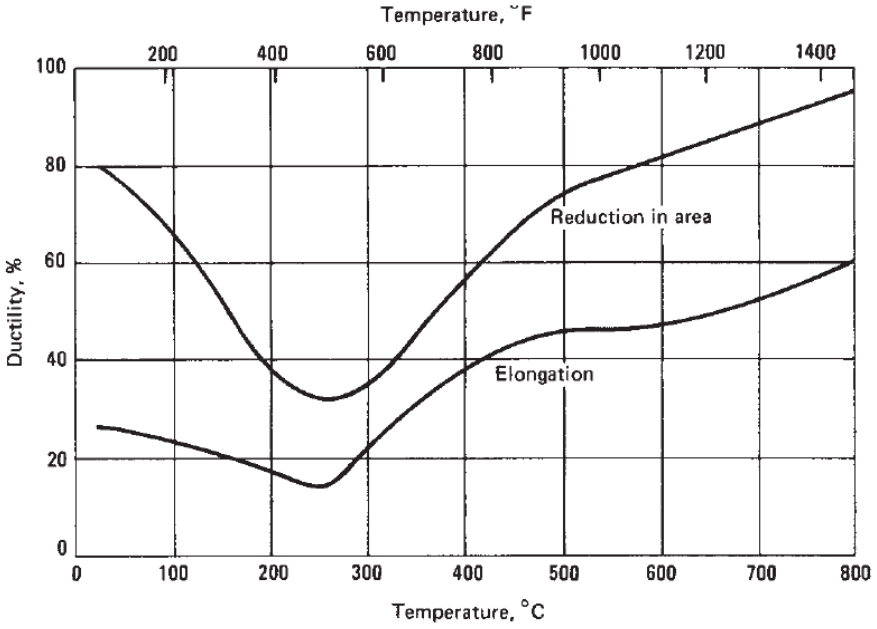

Figure 1. 1 – Elevated-temperature tensile properties of C10100 copper [2].

From the industrial point of view, hot formability has traditionally been faced either by a trial-and-error approach, or by the use of the concept of *formability window*, which

essentially consists in the definition of a temperature range within which it is recommended to process a particular metal alloy. Formability windows can be provided either by charts showing some formability parameters as a function of temperature (see Figure 1.1 which illustrates an example of this for a copper alloy) or simply by the indication of the suggested temperature range, as shown by the table in Figure 1.2 which describes the recommended intervals for a series of aluminium alloys.

Even after the wide introduction of FE simulation in industrial applications, however, a widespread critical aspect has remained the difficulty in obtaining reliable data for fracture criteria calibration, due to the relevant experimental efforts and costs that they can require. This lack of data is usually bypassed by applying a basic cold forging criterion without experimental calibration of the critical damage value. The strategy becomes then to find the process parameters (typically the dies geometries) that allow to reduce the maximum damage level resulting. This approach is acceptable in cold forging conditions, while, if applied to hot forging, can lead to rough approximations since the material formability dependency is totally neglected.

Materials	Forging temperature (°C)
1070	315–405
1100	315–405
2014	420–460
2017	420–470
2024	420–470
3003	315–405
5052	425–470
5056	300–500
6061	300–500
6063	350–450
7075	350–450

Figure 1. 2 – Temperature ranges for hot forging of aluminium alloys [3].

From the scientific point of view, on the other hand, the main efforts have been carried out on ductile damage modelling in cold conditions. After the complete development of the coupled criteria in the 90s, the research in the 2000s was mainly focused on a deeper comprehension of the role played by the deviatoric component of the stress tensor in the damage evolution. This led to the introduction of *fracture locus* concept and to a long series of works that provided different models capable of accurately describing the stress state condition influence on the fracture mode and taking it into account in the damage law formulation. Figure 1.3 provides an example of fracture locus in which the 3D curve represents the values of the strain at fracture which is a function of the stress state.

However these models have a complex analytical formulation and need expensive experimental campaigns for calibration which moreover must use non-standard test types and specimen geometries. This, in addition to the fact that they are still not implemented in the more common commercial FE codes, kept these criteria confined to the research field.

Conversely, research efforts on hot ductile fracture modelling have been much fewer and usually limited to the experimental determination of the strain at fracture as a function of temperature and strain rate (also this relation, though determined experimentally and with no analytical formulation, can be called “fracture locus”). An example of this is illustrated in Figure 1.4.

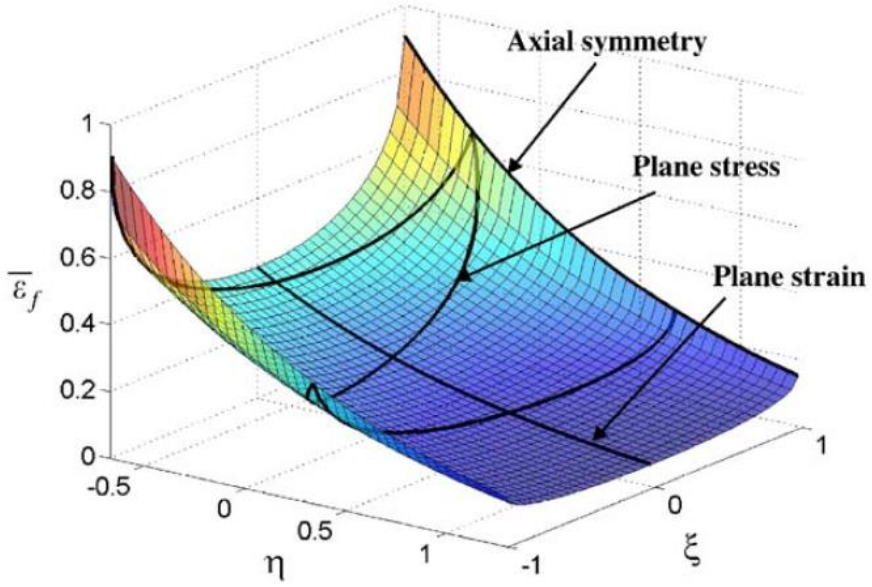

Figure 1. 3 – Representation of the fracture locus in the space of stress triaxiality and the deviatoric state variable [4].

Many works were also devoted to a deep investigation of the microstructural reasons of the formability behaviour of the material and in particular to its fracture mode assessment. However, very few works tried to use these experimental observations for the formulation of a hot damage law.

By definition, every fracture criterion in the vast cold damage modelling literature can be applied to hot conditions simply by writing its coefficients as a function of temperature and possibly of other thermo-mechanical variables, such as the strain rate. However this kind of approach has three important downsides:

- it needs large experimental campaigns and elaborate numerical inverse analysis for calibration in order to attain accurate results, yet having the normal downside of every empirical calibration, namely to provide good interpolation capabilities but poor extrapolation ones;
- it generates an empirical fracture locus which is laborious to be implemented in the FE codes;
- it does not provide any physical insight in what are the driving factors of the material formability behaviour and in particular do not allow to model properly changes in the material fracture mode.

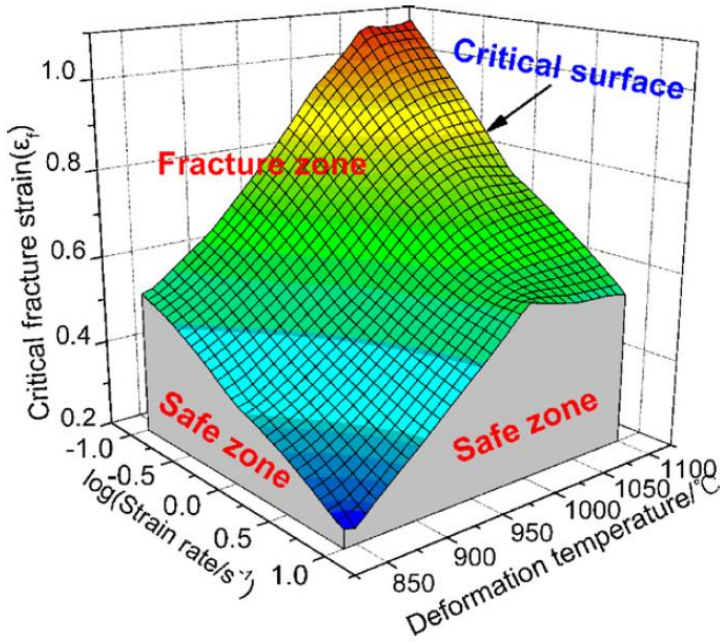

Figure 1. 4 – Critical fracture strain as a function of strain rate and temperature for Ti40 alloy [5].

Only in the last years some works were published which try to extend to hot conditions cold fracture criteria avoiding the merely empirical approach previously described and trying to make use of some physical parameters, such as the Zenner-Hollomon parameter or the thermal activation energy. However all these approaches are still far from giving a good physical insight on the ductile damage phenomenon in hot conditions and have limited representative capability, which make them supposedly not able to model the material behaviour in fracture mode-changing deformation regimes. As a last note, at present no validation of such approaches has been provided on a real

industrial process, while only validations based on simple laboratory tests (as tensile or compression tests) were carried out.

I.3 OBJECTIVE AND WORK ORGANIZATION

The main objective of the present work is the formulation of a new hot fracture criterion with the following characteristics:

- analytical formulation as a function of temperature and strain rate;
- dependency of the material constants on physical characteristics of the material;
- capability of the model to describe complex thermally-induced microstructural phenomena;
- ease of experimental and numerical calibration;
- validation performed on real industrial process.

To this aim the cross wedge rolling carried out at elevated temperatures on AA6082-T6 aluminium round bars was chosen as reference study case. Figure 1.5 illustrates qualitatively typical setups of this forging process.

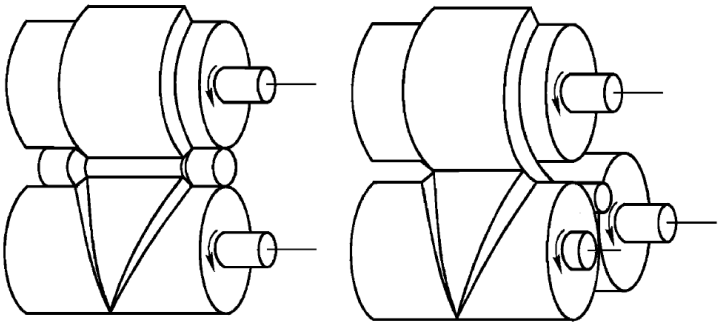

Figure 1. 5 – Cross wedge rolling two-rolls and three-rolls tooling configuration [6].

This study case is particularly interesting due to the following characteristics:

- it actually showed temperature-dependent Mannesmann axial cracking during industrial trials;
- the study case material is both a commonly used alloy for industrial applications and a material with a particular heat treatment which entails precipitated phases at the grain boundaries affecting the material characteristics;

- the uneven deformation and heat exchange conditions that are necessarily linked with this process can cause sharp thermal and strain rate gradients both with respect to time and position. This fact should fully exploit the capabilities of a fracture criterion modelling the thermal variables influence.

After setting up the process numerical model using the commercial code Forge 2011^{TM}, preliminary simulations were run in order to assess the stress and strain rate condition during the process. This has crucial importance both to assess a proper experimental campaign for material characterization and to choose the more suitable modelling of the stress influence on damage evolution.

Later on compression tests for rheology and tensile tests for formability characterization were carried out. The resulting formability behaviour was then assessed and its microstructural driving factors were investigated by microstructural analysis on the tensile specimens performed by SEM fractographic and micro-chemical analysis.

All these experimental data were then used to formulate and calibrate two fracture criteria:

- the former consisting in the empirical interpolation of the experimental data with bi-linear shape functions;
- the latter being the expression of a new physically-based fracture locus.

Both approaches were then implemented in the process numerical model and simulations were run to provide validation by comparison with the industrial trials outcomes. The resulting accuracy of the two models were finally critically discussed.

This thesis is divided into eight chapters: in Chapter 1 the hot bulk formability topic is introduced underlining its scientific and industrial relevance. Chapter 2 is dedicated to an accurate review on the state of the art of fracture mechanics phenomenon and modelling, while in Chapter 3 a synthetic outline of the approach taken to this work is shown. Chapter 4 follows with the description of the process numerical model and preliminary simulations carried out to investigate the thermo-mechanical conditions during the process. In Chapter 5, then the experimental campaign is defined and carried out. Chapter 6 is dedicated to the critical assessment of both the numerical and experimental outcomes that is needed for the formulation of the new fracture criterion that is finally calibrated and implemented in the FE code. Chapter 7 is dedicated to the validation of the developed model and to its application in an example of process parameter map development. The conclusions are finally drawn in Chapter 8.

II CHAPTER

BACKGROUND STUDY AND LITERATURE REVIEW

II.1 INTRODUCTION

In this chapter the analysis of the scientific literature about ductile damage is presented, with particular regard to the hot processing conditions.

In the first part the ductile damage is introduced in the more general frame of the mechanical failure. The physical phenomenon is described and its microstructural reasons and mechanisms are explained as well as the main physical influence variables.

Secondly the concept of *formability* is addressed and discussed: quantitative damage definition methods are described since they are the premise for damage modelling, in particular regarding bulk deformation processes. The fracture criteria developed for cold conditions are introduced and classified and the main strategies to extend damage modelling to hot processing conditions are discussed.

The review continues then with the description of the main works and results carried out in the last years on the hot formability characterization of light alloys.

One last chapter is devoted to the analysis of the reference study case process, the cross wedge rolling. The process is described listing its typical technological features and fields of application illustrating in particular the main research works produced on this topic.

II.2 DUCTILE DAMAGE PHENOMENOLOGY

II.2.1 Mechanical failure

Mechanical failure can be defined as the macroscopic phenomenon by which materials, when subjected to overload (and possibly other environmental variables such as temperature variations, corrosion and others) tend to undergo deformation and at last fail, namely they lose physical integrity. It is then evident how mechanical failure plays a key role in all engineering disciplines [7].

This is obviously a very complex phenomenon, with many influence variables, however the two main driving factors which affect mechanical failure are the material characteristics and the stress system. Under these two categories almost all the influence variables can be classified, as shown in Figure 2.1.

Different fracture mechanisms arise then in different conditions typical of various engineering application. For this reason the mechanical failure has been modelled in different ways. Structural engineering, for example, is primarily concerned by fatigue failure, the mechanisms of which are completely different by those typically arising in metal forming processes. The following chapter will focus on the latter ones.

The mechanical process leading to macroscopic failure has its origins at the microscopic scale and is then closely linked to the material microstructural features. The

microstructural transformations that the material undergoes when subjected to particular mechanical and environmental conditions, which eventually lead to failure are called *fracture mode* [8].

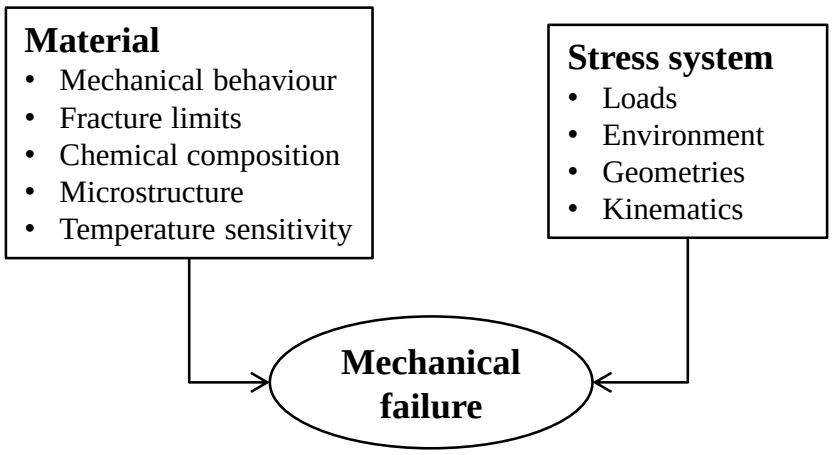

Figure 2. 1 – Mechanical failure driving factors.

Metal forming processes typically entail stress states well beyond the yield point and mono-cyclic loading. In these conditions the main fracture modes that can develop are [7, 8]:

- *ductile fracture*; this is the classic fracture mode of materials that can undergo high strain levels before failure. The mechanism, also known as *micro-void coalescence*, consists in the nucleation of voids at the micro-scale in regions of localized strain discontinuity, such as that associated with second phase particles, inclusions, grain boundaries, and dislocation pile-ups [8]. As the strain in the material increases, the micro-voids grow, coalesce, and eventually form a continuous fracture surface. This type of fracture exhibits numerous cuplike depressions, also known as *dimples*, that are the direct result of the micro-void coalescence. Figure 2.2 highlights two examples of dimpled fracture surfaces: from a qualitative point of view, deeper dimples (as those on the left picture) entail a larger strain capability before failure;
- *cleavage fracture*; this is a low-energy fracture that propagates along well-defined low-index crystallographic planes known as cleavage planes. Due to this fact, cleavage fracture surface is usually *transgranular*. Theoretically, a cleavage fracture should have perfectly matching faces and should be completely flat and featureless. However, metals are usually polycrystalline and contain grain and subgrain boundaries, inclusions, dislocations, and other imperfections that affect

a propagating cleavage fracture so that true, featureless cleavage is seldom observed and the fracture surface results in a series of featured cleavage surfaces, as illustrated in Figure 2.2.

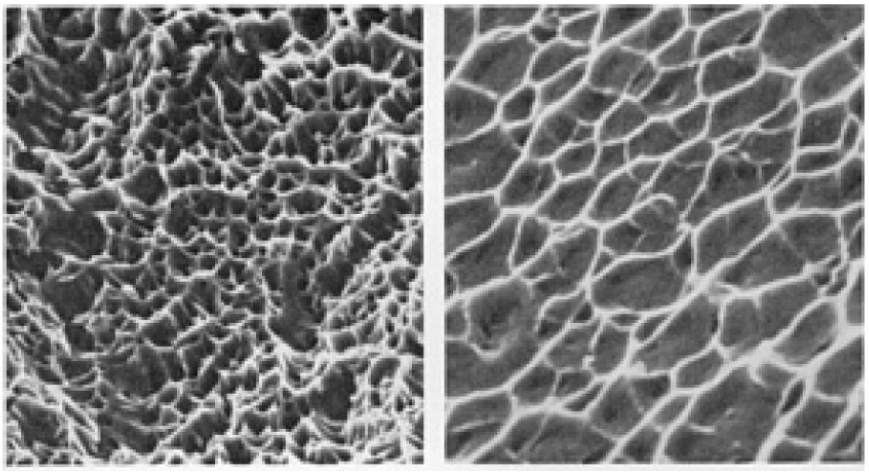

Conical equiaxed dimples Shallow dimples

Figure 2. 2 – Dimpled fracture surfaces, denoting ductile fracture [8].

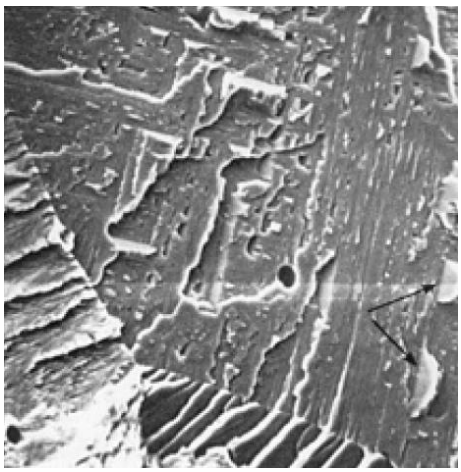

Figure 2. 3 – Polycrystalline-tongue-featured cleavage fracture surface [8].

- *intergranular fracture*; also referred to as *decohesive rupture*, this fracture mode occurs when little or no bulk plastic deformation is exhibited and no dimple rupture, cleavage, or fatigue take place. This type of fracture is generally the result of a reactive environment or a unique microstructure and is associated almost exclusively with rupture along grain boundaries. Grain boundaries contain the lowest melting point constituents of an alloy system. They are also easy paths

for diffusion and sites for the segregation of embrittling or low-melting elements. Thus the presence of these constituents at the grain boundaries can significantly reduce the cohesive strength of the material and promote decohesive rupture. Figure 2.4 shows an example of a decohesion-fractured surface.

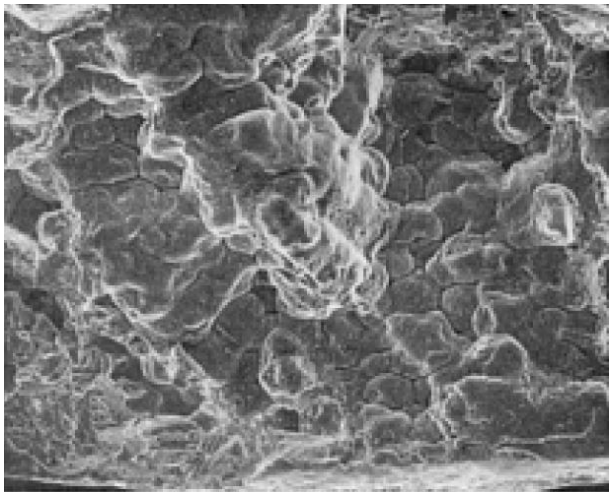

Figure 2. 4 – Intergranular fracture surface [8].

It must be pointed out, anyway, that these three fracture modes can develop alone, or in competition, resulting in mixed-featured fracture surfaces. Figure 2.5 summarizes schematically the micro-mechanisms of these three fracture modes.

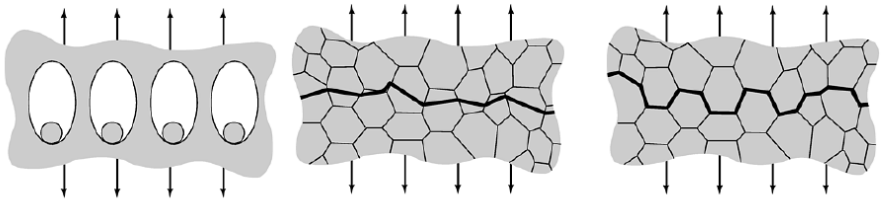

Figure 2. 5 – Main fracture modes for metal forming [7].

As also indicated by the name, ductile fracture is usually observed in materials that have a ductile behaviour, namely that can undergo significant plastic strain before rupture. On the other hand, though in some cases cleavage and intergranular fractures can be preceded by a high degree of plasticity [9], these fracture mechanisms are nevertheless usually associated to a brittle material behaviour.

This is the reasons because ductile fracture is the main fracture mechanisms that has been investigated and modelled for metal forming applications and is then worth to describe it in depth.

The micro-mechanics of ductile fracture is typically made up of three different stages:

- *voids nucleation*; usually at the boundary of a second phase particle or inclusion (stress-controlled process);
- *voids growth*; in terms of increasing volume and changing shape due to the deformation of the surrounding plastic matrix (strain-controlled process);
- voids coalescence, due to the interaction between neighbouring big holes, through which the macroscopic fracture starts and propagates (strain-controlled process).

Figure 2.6 illustrates schematically these three phases during a tensile test.

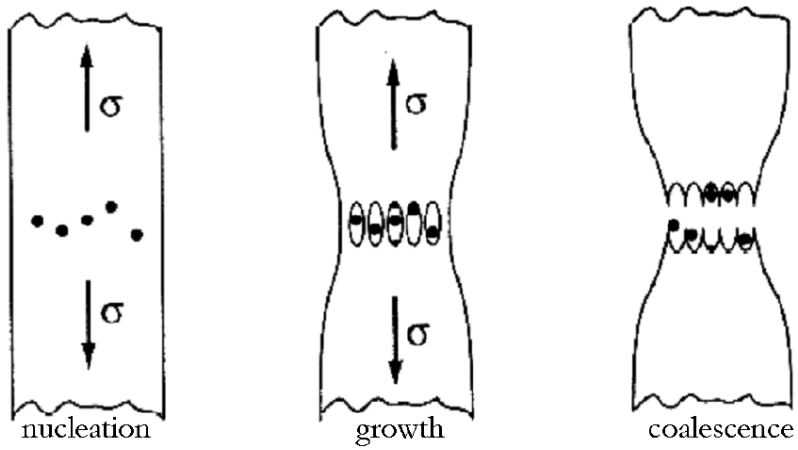

Figure 2. 6 – Ductile fracture stages [10].

From these considerations it results that, while damage initiation needs a minimum amount of stress to be triggered, its evolution is a process closely related to plastic deformation.

II.2.2 Influence variables

Though plastic strain-activated, voids growth and coalescence are very sensitive to the thermo-mechanical state under which the deformation occurs. Experimental evidence shows that, *for a particular material of given compositions*, four are the major influence variables:

- hydrostatic pressure;

- stress tensor deviatoric component;
- temperature;
- strain rate.

Due to the importance that these parameters assume both in the fracture phenomenon and in the fracture modelling, they are debated in the following dedicated paragraphs.

II.2.2.1 Hydrostatic pressure

Probably the most important factor influencing the fracture behaviour of ductile materials, the effect of hydrostatic pressure was firstly recognized and experimentally investigated by Bridgman [11] and later by Margevicius and Lewandowski [12], Liu and Lewandowski [13, 14] and Kao et al. [15].

In his famous work, which is still nowadays a very important source of experimental data on the topic, he carried out a large tensile test campaign putting the experimental apparatus in a pressure controlled chamber. This allowed him carrying out tensile tests with superimposed variable hydrostatic pressure. Twenty different types of steel were tested and each with type several different heat treatments. For each particular steel and heat treatment, tensile tests were performed under several constant levels of hydrostatic pressure ranging from 0 to 2700MPa.

The results clearly highlighted that materials become more ductile as they experience high compressive pressures. This finds its physical meaning in the fact that tensile stresses are the driving factor of void nucleation and growth, while compressive stress tend to inhibit void nucleation and even to close and at some extent cure existing voids and cracks.

The effect of hydrostatic pressure can be conveniently modelled by introducing the *stress triaxiality* defined as follows:

$$\eta = \frac{\sigma_H}{\bar{\sigma}} \tag{2.1}$$

which is the an adimensional quantity function of the hydrostatic stress and the Von Mises equivalent stress:

$$\sigma_H = \frac{\sigma_{xx} + \sigma_{yy} + \sigma_{zz}}{3} = \frac{\sigma_1 + \sigma_2 + \sigma_3}{3} \tag{2.2}$$

$$\bar{\sigma} = \frac{1}{\sqrt{2}} \sqrt{(\sigma_1 - \sigma_2)^2 + (\sigma_1 - \sigma_3)^2 + (\sigma_2 - \sigma_3)^2} \tag{2.3}$$

Stress triaxiality is then a normalized measure of the average value of the normal stresses in one point: positive values indicate a mainly tensile stress state, while negative values a compressive one.

Bao and Wierzbicki [16] analysed the Bridgman experimental results calculating an average triaxiality value and finding a very important outcome: -0.3 triaxiality value is a cut-off below which no mechanical failure is observed, for all the tested materials. This elaboration is summarized in Figure 2.7 in which any point corresponds to one of the Bridgman's experimental conditions.

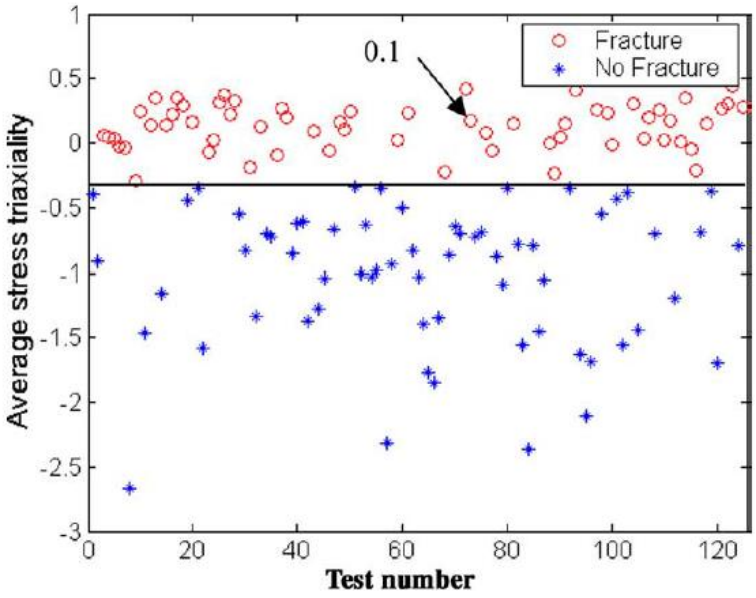

Figure 2. 7 – Triaxiality cut-off value using Bridgman results [16].

Another experimental way to highlight the negative triaxiality influence on strain at fracture consists in analysing the stress state in the post-necking deformation of a tensile test. From the physical point of view, the necking geometry causes the onset of positive radial stresses, which are impressed to the smaller section by the surrounding larger sections which have stopped their deformation due to strain localization.

The first study on this phenomenon was also carried out by Bridgman [11] who provided the following analytical formulation of the stress triaxiality at the bar axis as a function of the necking geometry:

$$\eta = \frac{1}{3} + \ln\left(1 + \frac{a}{2R}\right) \quad (2.4)$$

Figure 2.8 shows the geometrical configuration which Equation (2.4) refers to.

Systematic studies on the geometry influence on stress triaxiality were done by means of tensile tests on notched specimens. In this respect it is worth to remember the work of Hancock and Mackenzie [17] who found that notch presence entails higher triaxiality levels and lower strain at fracture and the work of Johnson and Cook [18] that highlighted the fact that the strain at fracture decreases exponentially with the stress triaxiality. It must be pointed out that the use of notched tensile test specimens allows to obtain high triaxiality values, namely higher than 0.333 (which is the stress triaxiality for a smooth specimen-tensile test during uniform deformation).

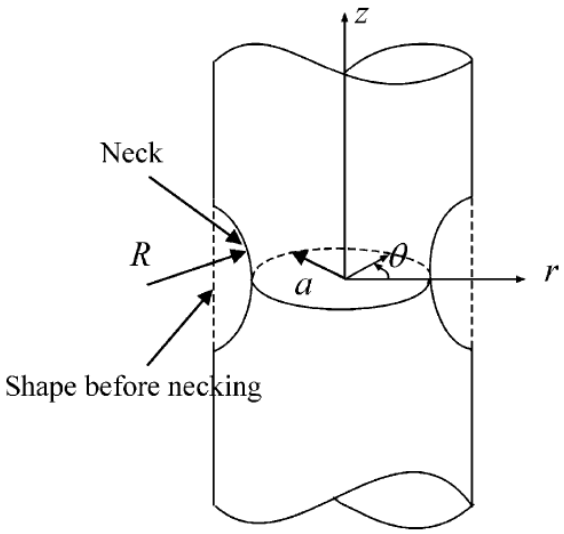

Figure 2. 8 – Tensile necking in a round bar [16].

2.2.2.2 Stress tensor deviatoric component

Recent studies highlighted a more complex influence of stress triaxiality on fracture strain for low to medium stress triaxiality values. The more systematic work in this sense is that of Bao and Wierzbicki, who carried out a series of tests on specimens of different shapes, expressly designed to attain different triaxiality levels [19]:

- upsetting tests, for low triaxiality levels (-0.3÷0);

- shear and combined shear-tensile tests, which are illustrated in Figure 2.9, for medium triaxiality levels (0÷0.4);
- tensile tests on smooth and notched specimens, for high triaxiality levels (0.4÷0.95);

The resulting strains at fracture are shown in Figure 2.10. The authors investigated the reasons of such behaviour and identified two sub-types of ductile fracture [20]:

- *shear failure*; responsible for fracture in the low stress triaxiality range;
- *void coalescence*; which is the mechanism at high triaxiality;

Bao and Wierzbicki then argued that for medium stress triaxiality values, the two mechanisms are both activated being the reason of the non-monotonic trend. The existence of these two sub-types of ductile fracture mode is also confirmed by the work of Barsoum and Faleskog [21] who carried out combined tensile and torsion tests and highlighted that voids coalescence is driven by internal necking at high triaxiality values and by internal shearing at low ones (see Figure 2.11).

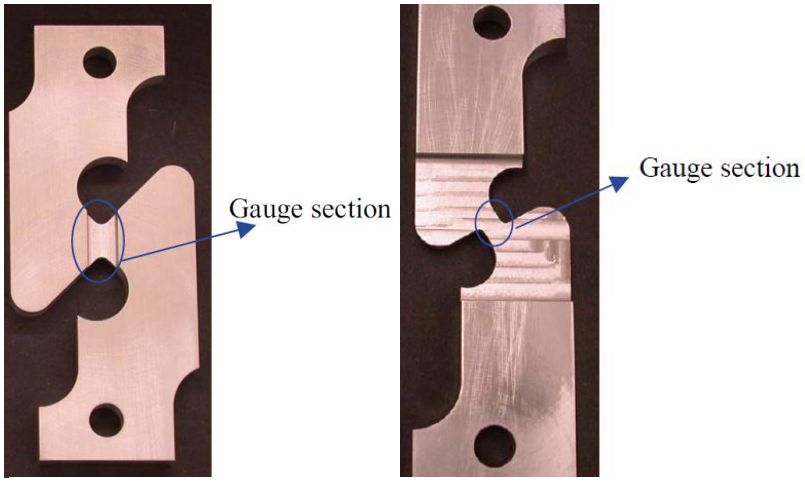

Figure 2. 9 – Shear and combined shear-tensile tests [19].

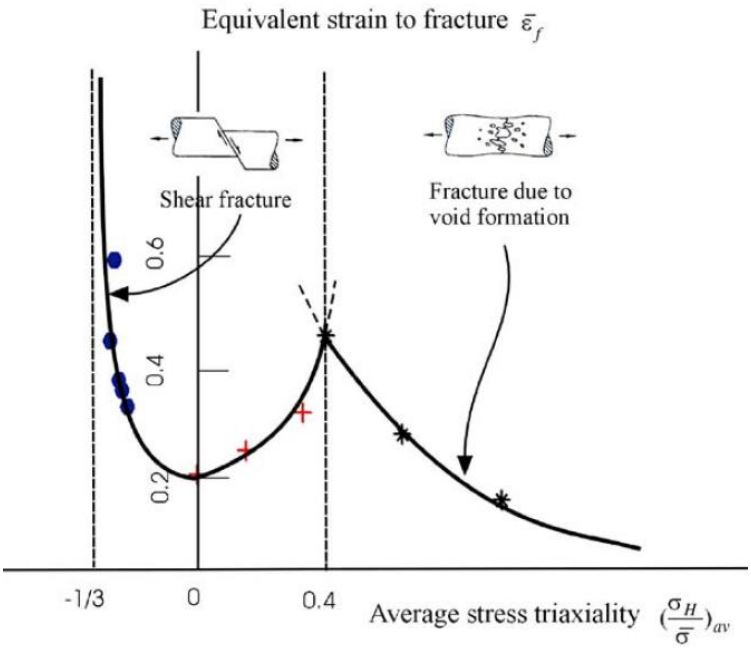

Figure 2. 10 – Bao and Wierzbicki experimental results [19].

These results are apparently in contrast with Bridgman's ones [11] which show a monotonic influence, but they just highlight the fact that the stress state influence on the fracture strain is too complex to be modelled with only one parameter, namely stress triaxiality. Indeed Bridgman's tests were all carried out under simple tension with superimposed hydrostatic pressure (which is also called "generalized tension" state), while Bao and Wierzbicki's results entail different stress states involving also a shear component for low and medium triaxiality values.

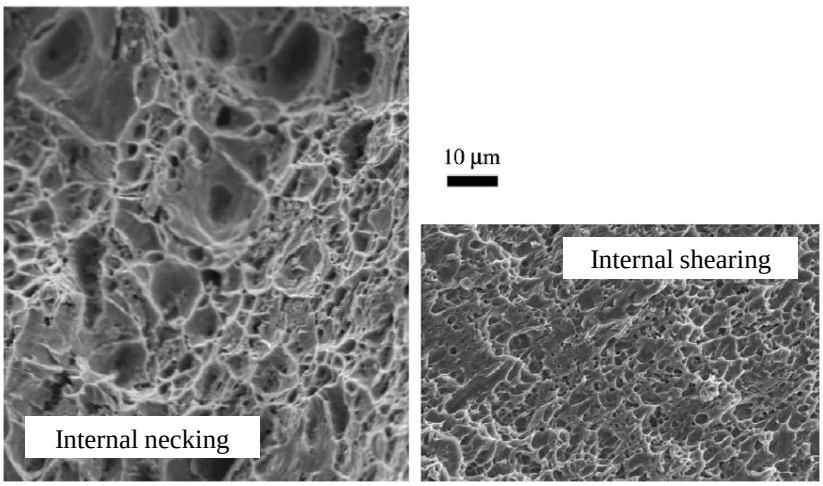

Figure 2. 11 – Void coalescence due to internal necking and internal shearing [21].

The first to introduce a parameter describing the shear stresses influence on strain at fracture was Xue [22]. In his work he argued that the difference between Bridgman's and Bao and Wierzbicki's experimental observations had to be attributed to the deviatoric component of the stress tensor (i.e. the stress deviator):

$$s_{ij} = \sigma_{ij} - \sigma_H \delta_{ij} \tag{2.5}$$

Rotating the stress deviator to its principal coordinate system, he then defined the *relative ratio of the principal deviatoric stresses* as:

$$\chi = \frac{s_2 - s_3}{s_1 - s_3} \tag{2.6}$$

This allows to see the different Bao and Wierzbicki's experimental points as part of different $iso-\chi$ curves, preserving the exponential dependence on stress triaxiality. This formulation allows also to define two limiting $iso-\chi$ curves, namely the upper and the lower bound. Figure 2.12 shows the Xue's result, with the blue line indicating the plane stress state.

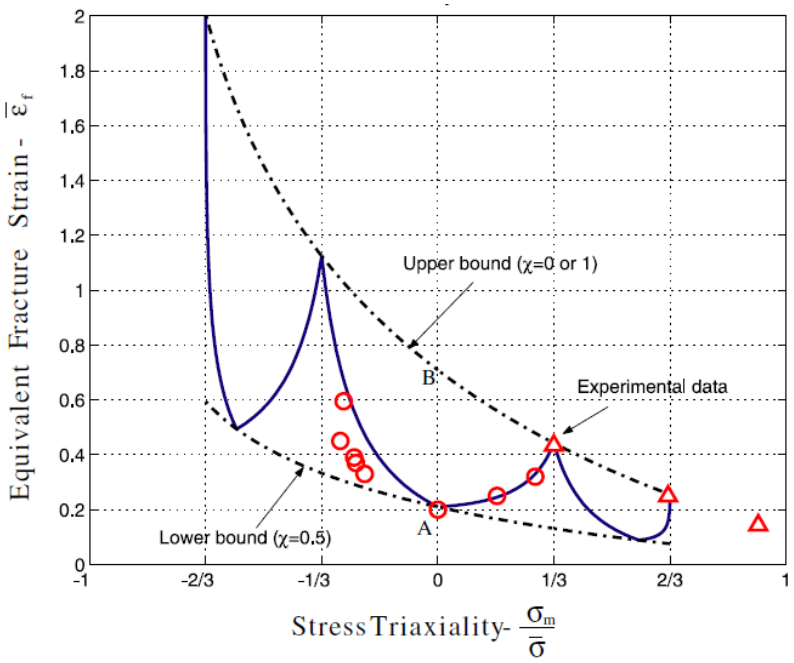

Figure 2. 12 – Upper and lower bound curves according to Xue [22].

Full experimental confirmation of the stress deviator influence on strain at fracture was recently provided by Faleskog and Barsoum [23] who carried out an extensive tensile-torsion test campaign keeping a constant value of the stress triaxiality, while varying the stress deviator by application of different twisting moments on the specimen.

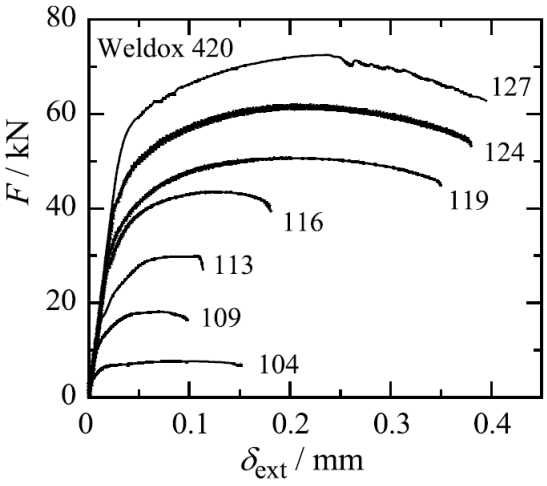

Figure 2. 13 – Stroke at fracture for increasing superimposed twisting moment [23].

The results, highlighted in Figure 2.13, clearly prove the reduction of the stroke at fracture with gradually increasing superimposed twisting moment (from test "127" to test "104").

2.2.2.3 Temperature and strain rate

Temperature and strain rate influences on ductile fracture are here discussed together since these parameters have a remarkable interaction. Moreover in cold conditions their influence on the fracture mechanics is negligible, thus this paragraph explicitly refers to warm and hot processing conditions.

Two important parameters were are classically defined in order to classify quantitatively the temperature and strain rate effect, the *homologous temperature* [24]:

$$T_{\text{hom}} = \frac{T}{T_m} \tag{2.7}$$

and the temperature compensated strain rate, also known as *Zener-Hollomon parameter* [25]:

$$Z = \dot{\varepsilon} \exp\left(\frac{Q}{RT}\right) \tag{2.8}$$

It is worth to underline that thermally-induced phenomena which affect material ductile behaviour have their profound reason in the microstructure physical and chemical evolution. Thus, all the mechanisms below described typically display together interacting and are described separately only for clarity sake.

Temperature and strain rate affect the fracture mechanics of a metal material due to:

- *recrystallization*; most metals undergo grain recrystallization at $0.4 \le T_{\text{hom}} \le 0.6$. This fact has a strong influence both on the material flow rule, since grain recrystallization erases the dislocations history preventing the possibility for strain hardening behaviour, and on the void nucleation mechanism, since voids usually are generated by stress concentration due to dislocation entanglement at inclusions or defects. This last point is one of the main reasons for the strain at fracture to grow with temperature. Also strain rate plays a role in this context affecting the recrystallization kinematics and causing for certain process conditions, the onset of *dynamic recrystallization*;
- *deformation mechanism*; in the same temperature range of recrystallization, $0.4 \le T_{\text{hom}} \le 0.6$, also the microstructural deformation mechanism changes: the

material rheological behaviour gradually passes from elasto-plastic to viscous with increasing temperature. Viscous solid materials behaviour, usually called *creep* [26], is caused by different mechanisms, depending on the Zener-Hollomon parameter value [27]:

- high Z values, namely low temperatures and high strain rates, entail the *dislocation creep* mechanism, which analogously to plastic deformation, occurs by dislocation movement. However, while in cold plastic deformation a dislocation needs a certain minimal stress to overcome an obstacle, in this case the dislocation can evade the obstacle by adding or emitting vacancies, thus allowing time-dependent deformation at constant stress. This creep mechanism, which is the limiting case with cold plastic deformation, usually entails low strain rate sensitivity and thus a reduced diffusion of the necking;
- intermediate Z, corresponding to intermediate temperatures and strain rates, entail the *diffusion creep*, which is driven vacancy direct movement on the crystal lattice, without any interaction with dislocations. In this process grain boundaries are sources and sinks of vacancies. This creep mechanism is associated with higher strain rate sensitivity;
- low Z values, namely high temperatures and low strain rates, entail the *grain boundary sliding* mechanism. In this case the material behaviour is the most similar to purely viscous: due to the higher temperatures the grain can slide one upon another at the grain boundaries. This deformation mechanism is usually present together with the diffusion creep, but its influence is remarkable since it allows to ensure the compatibility of grains which would be violated if only diffusion creep would occur (see Figure 2.14). This deformation mechanism is associated with the highest strain rate sensitivity and thus to the highest attitude to diffuse neccking.

Figure 2.15 highlights the deformation mechanism for an idealised material [26], with also the effect of strain rate highlighted by the dashed lines. It is important to point out that creep deformation, when present without other deformation mechanisms, leads to an intergranular fracture mode [8] which reduces the maximum strain at fracture. However creep deformation is associated to viscous rheological behaviour, which implies remarkable strain rate sensitivity, which in turn significantly increase the capability of the material to undergo have a long diffuse necking and thus reduced strain localizations. This aspect usually overcompensates the reduced strain at fracture, leading to higher total elongation

in tensile test, for instance. Creep can thus be regarded as a positive phenomenon for material formability.

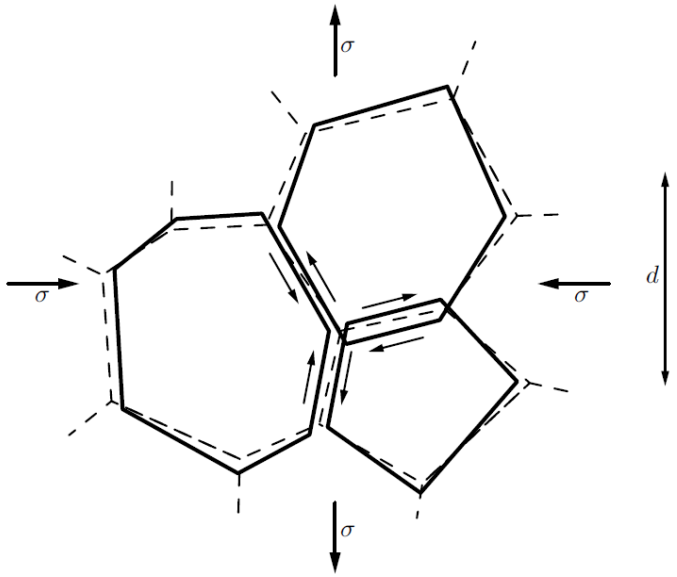

Figure 2. 14 – Grain boundary sliding ensuring the compatibility of grains [26].

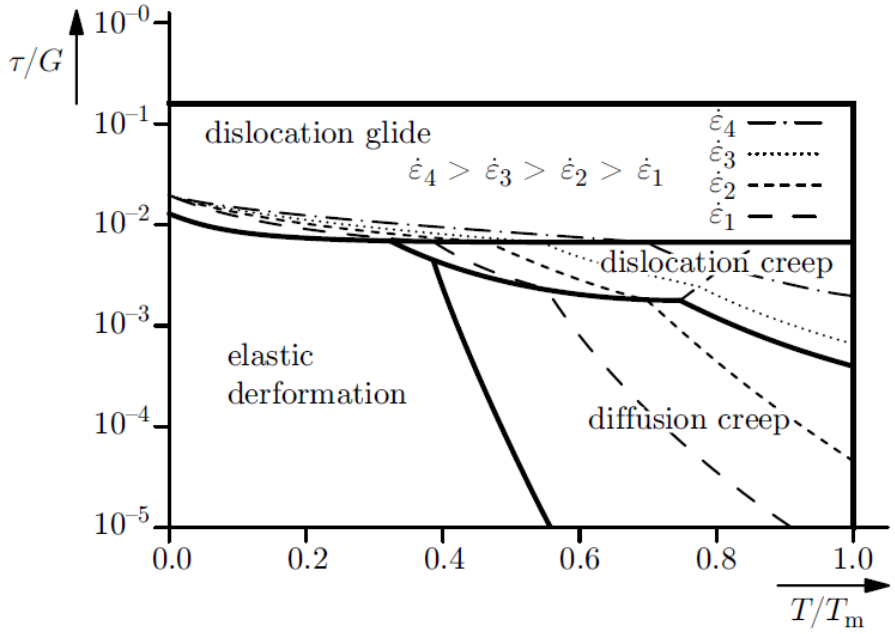

Figure 2. 15 – Effect of strain rate on deformation mechanism map [26].

- *grain boundary*; grain boundaries are the more energetic zones of the microstructure of a metal material and can include metastable structures such as intermetallic precipitates. Thus they are more sensitive to temperature changes which can have strong influence on the fracture mechanism. Rising temperature can cause at first diffusive phenomena between the grains and the boundaries leading finally to actual grain boundary melting, resulting in fast intergranular fracture, also known as *hot shortness*. This phenomenon is well documented by literature (see for instance the works of Chang et al. [28] and that of Alexandrov et al. [29]). The hot shortness onset is found to be anticipated by grain growth speed, as illustrated in Figure 2.16 [7].

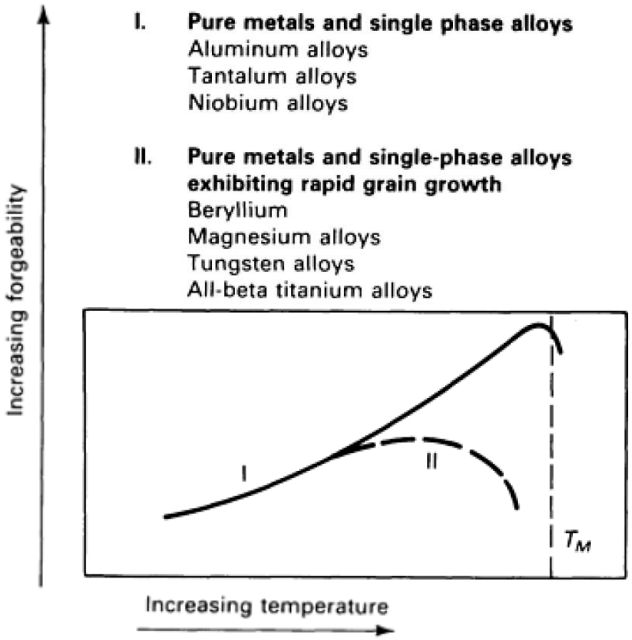

Figure 2. 16 – Single phase-metals hot shortness as a function of grain growth rate [7].

- *phase composition and distribution*; besides the phase changes that can occur at the grain boundaries, the metal alloy can undergo itself phase changes either by simply changing phase (which is the case of steels with the austenitic transformation) or by turning from monophasic to biphasic or vice versa (this is the case for example of some copper alloys, high-chromium stainless steels and Mg-Zn alloys). Depending on the material composition the phase transformation temperatures vary following the phase-diagrams and can cause sharp changes in the material strain at fracture trend. In these cases the effect is very material dependent and cannot be predicted with general models: for instance, if the new

phase composition is brittle, the material strain at fracture can just drop (determining a phase change-induced hot shortness), on the other hand if it is ductile it can have a short downtrend after which ductility restarts growing (this is one of the typical causes of reduced strain at fracture in warm conditions). Figure 2.17 illustrates an example of this.

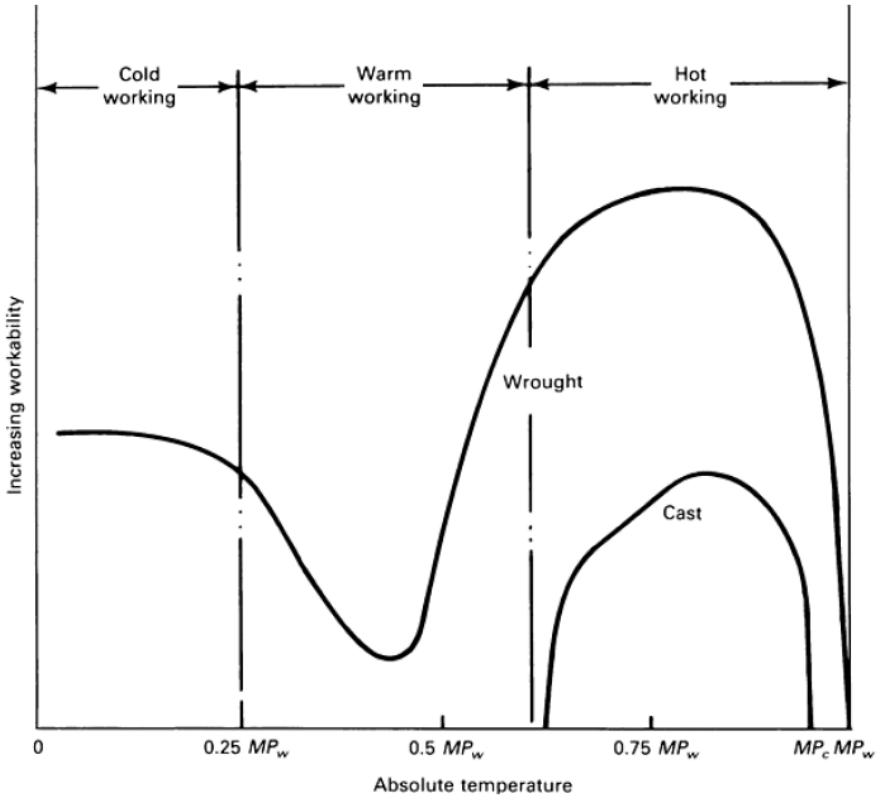

Figure 2. 17 – Typical warm workability drop for a wrought alloy [7].

II.3 DUCTILE DAMAGE MODELLING

II.3.1 Formability

Formability (or workability) is the term that is commonly used to refer to the ease with which metals can be shaped during bulk and sheet forming operations, respectively. In the broadest sense, formability indices provide quantitative estimates of the strength properties of a metal (and therefore the required working loads) and its resistance to failure. However, the latter characteristics (that is, ductility or failure resistance) is usually of primary concern [30, 31].

This ability to deform without fracture is highly variable, as seen in the previous paragraph, but, to be accurately modelled, this concept must first of all be defined in a more precise way.

From the practical *industrial point of view* the target is to achieve a determined final shape with a good, possibly undamaged, microstructure. Thus the requirements for a material to have a good formability are essentially:

- to have a high strain at fracture;
- to be capable of deforming uniformly avoiding strain localization;
- after necking to have the capability of necking diffusion, delaying strong strain localizations.

This approach, if applied to *numerical formability modelling*, can lead to misleading formability definitions for two reasons:

- strain at fracture depends on thermo-mechanical conditions; thus the same amount of strain on the same material can lead to fracture in some process conditions, while letting obtain a sound component in other ones;
- the capability to undergo uniform deformation or to have a diffuse necking are typically *rheology dependent-characteristics*; as a matter of fact they are a function of the strain hardening coefficient n in cold conditions and of the strain rate sensitivity coefficient m in hot conditions. A remarkable example of this fact can be found in creep regime-deformations in which materials usually do not have a high strain at fracture, due to intergranular fracture mode, but can bear a very wide uniform elongation, entailing good formability.

Thus, from the numerical point of view the formability modelling addresses only to describe the material behaviour in terms of fracture mechanics, while rheological characteristics are modelled apart.

Another important distinction is provided by the metal forming process type [30]:

- *sheet metal forming*; in this type of process the part thickness is smaller of at least one order of magnitude, compared with other dimensions. On the one hand this fact often allows to assume simplifying hypothesis for the stress and strain field (although not always, such as in blanking processes). On the other hand it implies harder FE modelling due to the fact that the part thickness is a limiting parameter for mesh size. For all these reasons the use of Forming Limit Diagrams (FLDs) [32] has become the usual industrial standard approach as well as the more used scientific one.

- *bulk metal forming*; in this type of process generally no particular geometrical assumption can be done, thus a full 3D numerical solution is needed [33]. This led to model the fracture evolution by using *fracture criteria.*

The following review is about the scientific production on this second topic.

II.3.2 Fracture criteria

In order to describe the approach to ductile fracture modelling by means of fracture criteria, two fundamentals definitions must be remembered. The first one is that of *Von Mises equivalent strain*:

$$\bar{\varepsilon} = \frac{\sqrt{2}}{3}\sqrt{(\varepsilon_1-\varepsilon_2)^2+(\varepsilon_1-\varepsilon_3)^2+(\varepsilon_2-\varepsilon_3)^2} \quad (2.9)$$

The second one is the definition of *damage*:

$$D = f(\sigma_{ij}, \varepsilon_{ij}, T, \dot{\varepsilon}_{ij}, material\ characteristics) \quad (2.10)$$

Damage is the central concept of FE ductile fracture modelling. It can be qualitatively defined as a volume scalar variable (in case of isotropic damage, which is assumed in this work) that keeps into account how much the void nucleation, growth and coalescence process has advanced affecting material integrity. When material is virgin by definition $D=0$, while the failure is identified by the *damage critical value* D^*.

The shape of the f function consists in the *fracture criterion formulation*, which essentially means defining a proper *analytical damage evolution law*.

On the other hand the definition of D^* must be done experimentally and is usually called *calibration*. Depending on the fracture criterion formulation, its calibration usually entails also the determination of all the other material coefficients in f. Fracture criteria calibration is usually performed in two alternative ways:

- *direct calibration*; which entails a damage definition which can be experimentally measured. The usual approach in this case is to perform a series of formability tests (e.g. tensile tests) interrupted at various stages and to carry out the direct measurement of the damage accumulated. These experimental data are then used to calibrate the criterion. Direct calibration is the more rigorous way for calibration, but usually implies huge experimental efforts;
- *inverse calibration;* which can be applied with any definition of damage and essentially consists on FE simulation inverse analysis on an formability test to

determine the models constants that provide the best data fitting. Though less rigorous, this approach is far less expensive and time consuming.

Another fundamental concept in damage modelling is that of *damage coupling*, which consists in linking the damage evolution with the material rheological behaviour, to take into account the reduced material strength due the void growth. This distinction provides a first macro-categorization of damage models, which can be divide in uncoupled and coupled criteria. Figure 2.18 highlights the effect of damage coupling computation: the flow stress calculated by a FE-simulated tensile test with damage coupling is lower than the uncoupled one because of the reduced load that the specimen can bear due to the void presence.

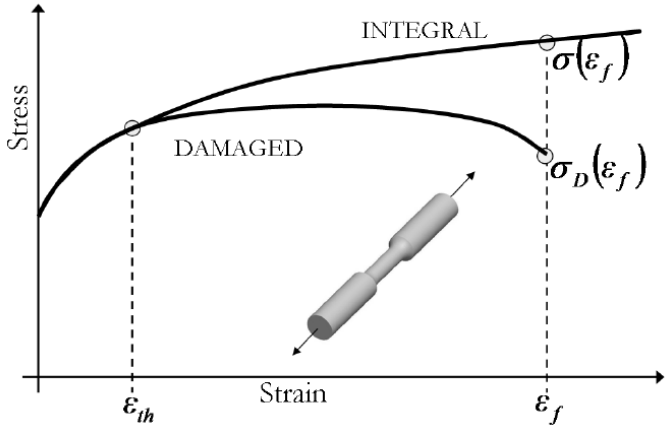

Figure 2. 18 – Coupled and uncoupled tensile test flow curve [10].

Fracture criteria early formulation precedes the computer information age and dates back to the pioneering work of Cockroft and Latham [34] who formulated probably the first (uncoupled) damage criterion. However the complete formalization of some concepts that are at the basis of damage modelling were accomplished with the coupled damage formulation of Lemaitre [35], who set damage evolution in the more general frame of the thermodynamics of the irreversible processes, founding the so called Continuum Damage Mechanics (CDM). One of the most important Lemaitre's assumptions, which is usually neglected from the practical point of view, but on which lies a rigorous representation of the damage phenomenon, is the *strain equivalence principle*:

"Any strain constitutive equation for a damaged material may be derived in the same way as for virgin material except that the usual stress is replaced by the effective stress"

This assumption has two fundamental implications, the second of which can be extended to every fracture criterion:

- it provides the definition of *effective stress* which is the basis for Lemaitre's damage coupling;
- it allows to avoid describing the voids interaction with the material at the micro-scale, assuming that any effect can be represented at the *meso-scale* by the effective stress.

II.3.3 Cold damage modelling

Introducing the review of the main fracture criteria, it is worth to point out that they were originally developed for cold processing conditions and thus they do not take into explicit account temperature and strain rate in the damage law formulation.

Depending on the assumptions which were done in order to model the damage evolution the damage criteria are here divided in five categories:

- Energy based-criteria;
- Void growth-based criteria;
- Porosity-type criteria;
- Continuum Damage Mechanics-based criteria;
- Stress deviator-based criteria.

These five categories are here listed in the chronological order in which they were proposed and can also be classified in the two already mentioned categories of uncoupled and coupled criteria, as shown in Figure 2.19.

UNCOUPLED CRITERIA	ENERGY-BASED	COCKROFT-LATHAM
		BROZZO
		FREUDENTHAL
	VOID GROWTH	MCCLINTOCK
		RICE-TRACEY
		OYANE-SATO
	STRESS DEVIATOR	XUE-WIERZBICKI
		WILKINS
		EXTENDED MOHR-COULOMB
COUPLED CRITERIA	POROSITY-BASED	GURSON
		TVEEGARD&NEEDLEMAN
	CDM	LEMAITRE
		BONORA

Figure 2. 19 – Fracture criteria classification.

II.3.3.1 Energy-based fracture criteria

These are the simplest approaches to damage modelling as well as the first to be developed. Starting from the experimental observation that damage evolution is activated by tensile stresses but its growth is linked with the amount of plastic deformation, these criteria define the damage as an *integral form of a stress in the equivalent plastic strain*. Damage is then somehow related with a *plastic energy* component dissipated by the material during deformation. Therefore fracture occurrence is related to the maximum energy the material can store before failure. These criteria are pretty simple to calibrate experimentally since only the critical damage value D^* has to be determined.

One of the first and well known criteria is the one proposed by Cockroft and Latham [34]:

$$D = \int_0^{\bar{\varepsilon}} \sigma_1 d\bar{\varepsilon} \tag{2.11}$$

in which σ_1 represents the maximum principal component of the stress tensor. In this case the authors proposed as fundamental the role of the first principal stress on material ductility.

Based on this formulations other authors proposed some modifications in order to improve the prediction accuracy. For states of stress different from purely tensile ones, Oh et al. [36] modified the Cockroft-Latham formula by normalizing the maximum principal stresses by the equivalent stress:

$$D = \int_0^{\bar{\varepsilon}} \frac{\sigma_1}{\bar{\sigma}} d\bar{\varepsilon} \quad (2.12)$$

This is one of the more used criteria in case either simple modelling is required or the stress conditions do not vary substantially during deformation: as a matter of fact, when applied to very different stress states this criterion shows evident lacks, as was proved in the already cited [4] in which, being calibrated with upsetting tests, showed overestimating damage predictions for high triaxiality values (see Figure 2.20).

Brozzo et al. [37] proposed a further modification in order to include an explicit dependence on hydrostatic stress:

$$D = \int_0^{\bar{\varepsilon}} \frac{2\sigma_1}{3(\sigma_1 - \sigma_H)} d\bar{\varepsilon} \quad (2.13)$$

while Freudenthal proposed a different formulation [38], replacing σ_1 with the equivalent Von Mises stress. Thus the damage equals the plastic work of deformation per unit volume (generalized plastic work):

$$D = \int_0^{\bar{\varepsilon}} \bar{\sigma} d\bar{\varepsilon} \quad (2.14)$$

All these criteria are simple to be calibrated and provide reasonably good fracture prediction if applied to stress state similar to those used for calibration, but can lead to rough approximation otherwise (*calibration test dependency*).

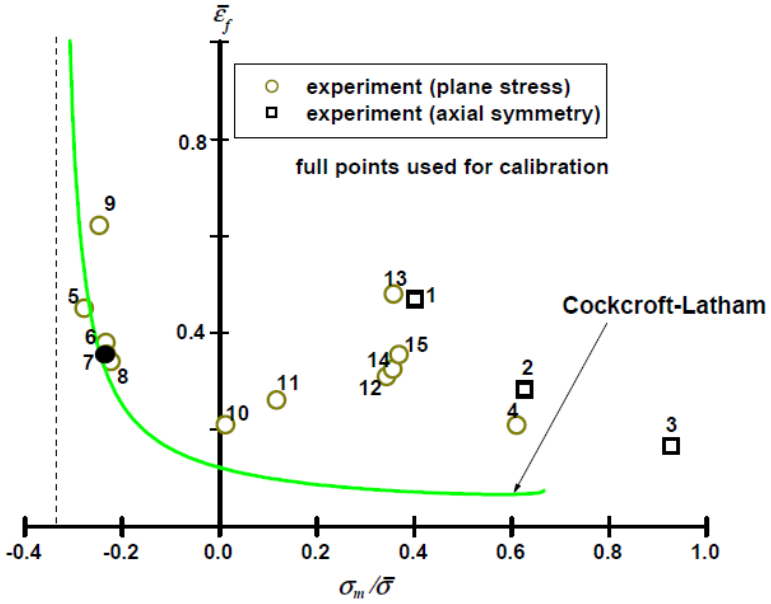

Figure 2. 20 – Fracture criteria classification.

II.3.3.2 Void growth-based criteria

The fracture criteria of this family base their formulation on the modelling of the mechanism of voids growth and coalescence for the onset of fracture.

McClintock [39] developed the first ductile fracture criterion based on this approach: his model consists in an elliptical hole in a material subjected to plane stress conditions. The two principal stresses σ_a and σ_b are supposed parallel to the hole principal axis and the hole is surrounded by a reference cylindrical cell whose dimensions are of the order of the mean spacing between the voids in the actual material. Figure 2.21 shows a schematic representation of this. The fracture is assumed to take place when the hole enlarges up to touching its cell. Under some additional simplifying assumptions the expression of damage becomes:

$$(2.15)\quad D = \int_0^{\bar{\varepsilon}} \left\{ \frac{\sqrt{3}}{2(1-n)} \sinh\left(\frac{(1-\mathrm{n})(\sigma_a + \sigma_b)}{\bar{\sigma}} \right) \right\} d\bar{\varepsilon}$$

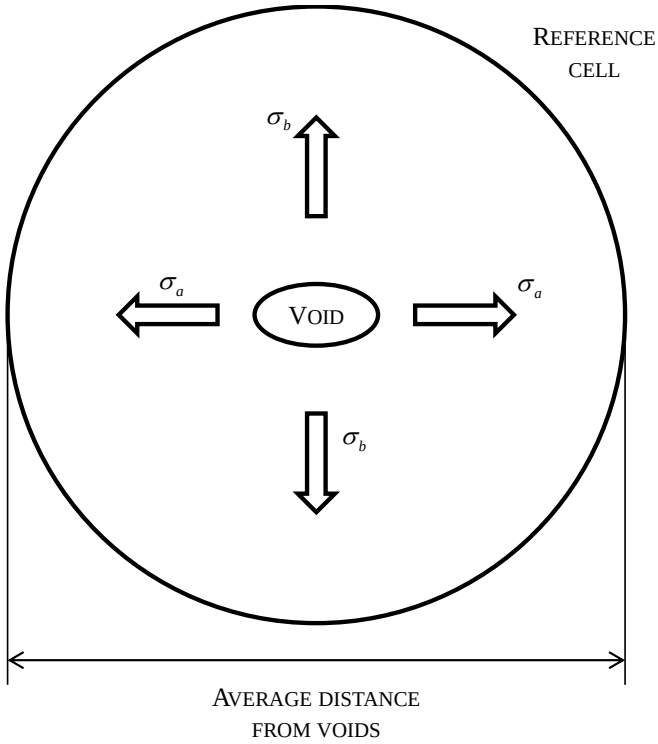

Figure 2. 21 – McClintock's void enlargement model scheme.

It must be pointed out that the model explicitly takes into account the mechanical behaviour of the material by means of the strain hardening coefficient n. In spite of the simplified representation of the single void growth and the states of stress and strains, the model is able to describe the failure condition in numerous experimental conditions and made it possible many observations concerning triaxiality, strain hardening and stress/strain history influences on ductile fracture.

McClintock's work was considered and improved by Rice and Tracey [40] who modelled the enlargement of a spherical void in a general tri-axial remote field. Their study considers the effect of superimposed hydrostatic tensions and first recognize the stress triaxiality as the leading factor for void enlargement. The exponential form derived by Rice and Tracey is the same experimentally obtained by Johnson and Cook and is sometimes classified with their names:

$$(2.16)\quad D = \int_0^{\bar{\varepsilon}} B_1 e^{B_2 \frac{\sigma_H}{\bar{\sigma}}} d\bar{\varepsilon} = \int_0^{\bar{\varepsilon}} B_1 e^{B_2 \eta} d\bar{\varepsilon}$$

in which B_1 and B_2 assume values depending on the equivalent stress assumed (wether Tresca's or Von mises'), but are in the FE practice usually experimentally calibrated for better data fitting.

Finally the results of Oyane's work [41], further developed together with Sato and others [42], is here presented:

$$(2.17)\quad D = \int_0^{\bar{\varepsilon}} \left(1 + A \frac{\sigma_H}{\bar{\sigma}} \right) d\bar{\varepsilon}$$

which was initially derived for porous materials under the assumption that failure onset is triggered by a certain amount of volumetric deformation (i.e. void growth). The A constant must be experimentally calibrated, but Oyane and Sato provided in their work a calibration of the criterion by means of upsetting test and an experimental application of it in an indirect extrusion process, verifying its capabilities when different states of stress (in terms of triaxiality) are deforming the material. Following applications confirmed how this model is suitable for many common situations.

It is interesting to observe that he results of Oyane and Sato's calibration was a value of $A = 3$ which corresponds to assuming that damage evolution stops for triaxiality values $\eta \leq -1/3$, which perfectly fits with Bao and Wierzbicki's elaboration of Bridgman's results [16] already highlighted in Figure 2.7.

Due to this fact and to the vast successive experimental confirmations on different metal forming processes [43-45], this model has become one of the most used due to its simple experimental calibration and its effectiveness in different stress and strain conditions.

II.3.3.3 Porosity-based fracture criteria

The first approach to damage modelling able to provide coupling between damage evolution and stress state is due to the work of Gurson [46]. In his work he considered the material as a porous medium characterized by a *void volume fraction* which is identified with the material damage:

(2.18) $$D = \frac{V_{voids}}{V}$$

(2.19) $$\dot{D} = \frac{dD}{dt}$$

This is a very important assumption since it gives a precise physical meaning to the damage variable and also p*rovides the basis for damage coupling*. It also implies that the critical damage value is always unity:

(2.20) $$D^{*} \equiv 1$$

Gurson modelled then separately the nucleation and the void growth linking them respectively to the plastic equivalent strain and to the volumetric strain:

(2.21) $$\dot{D} = \dot{D}_{nucl} + \dot{D}_{growth}$$

(2.22) $$\dot{D}_{nucl} = A\dot{\bar{\varepsilon}}$$

(2.23) $$\dot{D}_{growth} = (1-D)\sum_{i} \varepsilon_{ii}$$

Damage coupling is finally provided by a modification of the Mises' flow stress surface function:

(2.24) $$\Phi = \left(\frac{\bar{\sigma}}{\sigma_{yield}} \right)^{2} + 2D\cosh\left(\frac{3\sigma_{H}}{2\sigma_{yield}} \right) - 1 - D^{2} = 0$$

in which the assumption that micro-voids do not interact is also implicitly made. This assumption however do not allow to properly model the damage evolution final stages in which void coalescence dominates.

In order to take in to account the evident effect of the coalescence of adjacent voids on crack initiation and propagation, Tvergaard and Needleman [47, 48] introduced an empirical modification of the damage definition to model the damage acceleration in the final deformation stages in which D_{coal} is the limit damage value which triggers damage acceleration, while K is a material constant:

$$\tilde{D} = \begin{cases} D & \text{if } D \le D_{coal} \\ D_{coal} + K(D - D_{coal}) & \text{if } D > D_{coal} \end{cases} \quad (2.25)$$

which is then introduced in the expression of the flow stress function in addition to two empirical coefficients, q_1, q_2:

$$\Phi = \left(\frac{\bar{\sigma}}{\sigma_{yield}} \right)^2 + 2q_1\tilde{D}\cosh\left(q_2 \frac{3\sigma_H}{2\sigma_{yield}} \right) - \left[1 + (q_1\tilde{D})^2 \right] = 0 \quad (2.26)$$

It is worth to point out that q_1 and q_2 are material-dependent constants. Figure 2.22 illustrates the influence of damage on the flow stress surface function.

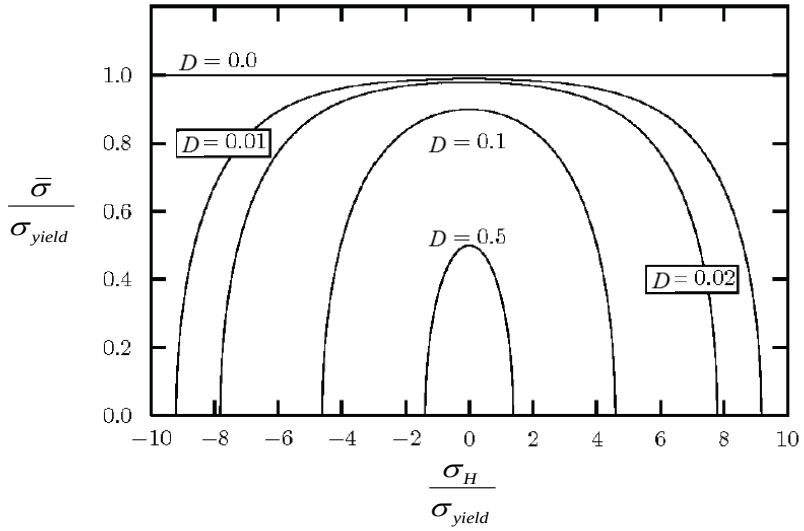

Figure 2. 22 – GTN model flow stress surface function.

The model in Equations (2.25) and (2.26) is then called the GTN model (Gurson - Tvergaard - Needleman) and is the reference model in the porosity-based category.

II.3.3.4 Continuum Damage Mechanics

Continuum Damage Mechanics (CDM) approaches the fracture phenomenon with a thermodynamic method in which damage is treated as a continuum variable which is affected by irreversible processes. As already stated, the reference in this field is the work of Lemaitre [35, 49] and of Lemaitre and Desmorat [50]. In their work the damage is defined at the *mesoscale*, which is a dimension among the macro-scale and the micro-

scale that for metals can be estimated in about 0.1mm^3. At the meso-scale a piece of material can still be considered as a continuum, describing the microstructure by means of average values, yet is small enough to be ragarded as an element with respect to the macro-scale. This material element is called *reference volume element* (RVE). The damage is then defined in the RVE as the relative fraction of section area that is occupied by voids, A_{voids} :

$$D = \frac{A_{voids}}{A_0} \tag{2.27}$$

This damage definition assumes isotropy of damage, but can be generalised to anisotropic damage features. This definition is strictly linked with the *effective stress* concept proposed by Kachanov [51], which provides the *damage coupling*:

$$\sigma_{EFF} = \frac{\sigma A_0}{A_0 - A_{voids}} = \frac{\sigma}{1-D} \tag{2.28}$$

which is the stress calculated using the effective cross section which can bear the load, neglecting the part which is actually occupied by voids. The same approach can be used to evaluate all the effective mechanical variables and parameters, such as the elastic modulus:

$$E_{EFF} = E(1-D) \tag{2.29}$$

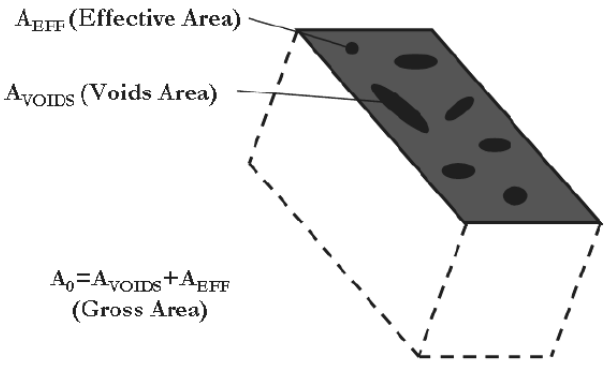

Figure 2. 23 – Lemaitre effective area definition in RVE [50].

At the basis of this model there is the already mentioned fundamental *strain equivalence principle* [35].

By definition undamaged material corresponds to $D = 0$ while the rupture of the element corresponds to a critical value $D = D_C$ (usually comprised in the $0.2 \leq D_C \leq 0.8$ range for metals).

Taking the *free energy as thermodynamic potential* allows to derive the following expression for the *damage strain energy release rate*:

$$(2.30) \quad -y = \frac{\bar{\sigma}^2}{2E(1-D)^2} R_V$$

which is proportional by a factor 2 to the rate of *elastic* energy per unit volume which is released (i.e. dissipated) by the damage development. The term R_V is called the *triaxiality function* and its expression is due to separation of the two terms associated to the shear and the volumetric deformation energies:

$$(2.31) \quad R_V = \frac{2}{3}(1+\nu) + 3(1-2\nu)\left(\frac{\sigma_H}{\bar{\sigma}}\right)^2$$

Finally, in order to derive the constitutive equations to evaluate the dissipative variables, a *potential of dissipation* ϕ is defined so that:

$$(2.32) \quad \dot{D} = -\frac{\partial \phi}{\partial y}$$

Assuming plastic and isotropic material behaviour, the potential can be expressed in the following way:

$$(2.33) \quad \phi = \frac{S_0}{(s_0+1)}\left(\frac{-y}{S_0}\right)^{s_0+1} \dot{\bar{\varepsilon}}$$

leading to the final expression of the *damage rate*:

$$\dot{D} = \left(\frac{-y}{S_0} \right)^{s_0} \dot{\bar{\varepsilon}} \quad (2.34)$$

in which the *damage strength* S_0 and the *damage exponent* s_0 are material and temperature dependent parameters. In view of the square of stress triaxiality term in triaxiality function, moreover, there is no difference between material degradation under tensile or compressive state of stress. In order to fix this the damage rate expression in Equation 2.34 is used only for positive values of stress triaxiality. For negative values of stress triaxiality, the formulation is reduced by a h_C factor usually assume equal to 0.2:

$$\dot{D} = \left(\frac{-h_C y}{S_0} \right)^{s_0} \dot{\bar{\varepsilon}} \quad (2.35)$$

One of the more significant improvements taken to the Lemaitre work has been provided by Bonora [52] who proposed a nonlinear model for ductile fracture developed from experimental observations. A general nonlinear damage dependency from plastic deformation was established when a new exponent that determines the shape of the damage evolution with plastic strain was introduced.

Probably the most comprehensive and rigorous approach to ductile fracture modelling, the CDM has however two limitations:

- it generally shows a higher *mesh size dependency* if compared with uncoupled approaches, as also reported by Bouchard et al. [53];
- it does not take into account the extensive experimental evidences highlighted in the last years about the stress deviator influence on ductile fracture.

II.3.3.5 Stress deviator-based fracture criteria

One of the first works modelling the influence of the stress deviator on the fracture evolution is that of Wilkins et al. [54] in the early 80s, in which the following damage law was postulated:

$$(2.36)\quad D = \int_0^{\bar{\varepsilon}} \frac{1}{(1-a\sigma_H)^{\lambda}} (2-A)^{\mu} d\bar{\varepsilon}$$

For fracture to occur the model requires that the critical damage value is reached over a critical dimension R_C. In the expression of Equation (2.36) μ, λ and a are material constants, while A is a function of the stress deviator defined as follows:

$$(2.37)\quad A = \max\left(\frac{s_2}{s_1}, \frac{s_2}{s_3}\right)$$

with $s_1 \geq s_2 \geq s_3$. It is worth to remark that the model dependence on the hydrostatic and deviatoric components of the stress tensor is defined in a separable form.

After the Wilkin's work, the studies on stress-deviator-dependent fracture criteria did not attract big attention until the already mentioned work by Wierzbicki and Bao [19]. The large number of experimental data provided proved to be very useful for new models calibration and validation, focusing back the attention on the theme. Moreover, with the experimental contributions of Barsoum and Faleskog [21, 23], it has become clear that a simple monotonic stress triaxiality dependence was not capable of describing accurately the material ductility in a wide range of stresses, generating *calibration-test-dependent fracture criteria*.

A first attempt to model the new experimental outcome was done in the same work [19] in which the authors proposed to model the equivalent strain at fracture as a function of triaxiality by means of three parabolic functions, one for each triaxiality zone, as illustrated in Figure 2.24. However, this approach to the problem shows evident lacks:

- it is too empirical, avoiding to model the stress deviator influence, which is the deep reason of the non-monotonic behaviour of the formability;
- it needs expensive experimental campaign for calibration.

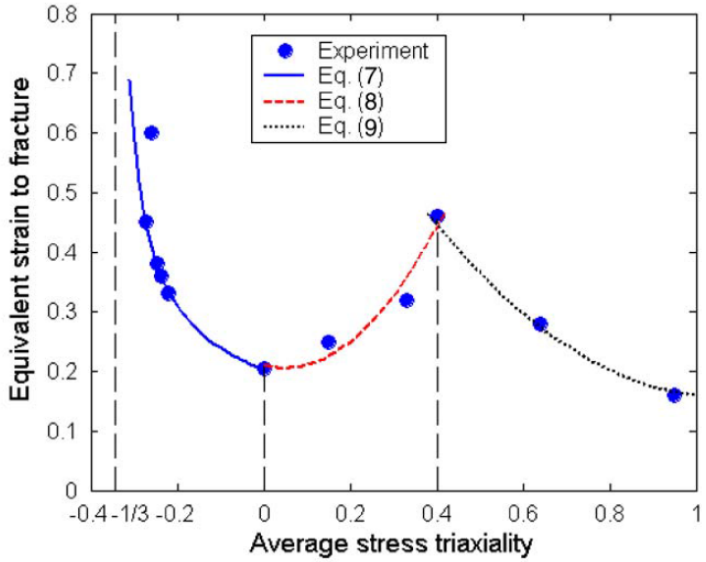

Figure 2. 24 – Fracture locus interpolation with three functions [19].

The already mentioned work of Xue [22], later on developed and validated with Wierzbicki [55] was the first to provide an organic formulation of the formability dependence on the stress deviator. By this formulation a *complete stress state characterization* is possible by means of the so-called *cylindrical decomposition*, which makes use of the Haigh-Wasteegard stress coordinates, schematically illustrated in Figure 2.25. Xue wrote the strain at fracture as a separable function of the hydrostatic pressure and Lode angle [56]:

$$\varepsilon_f = \varepsilon_f\left(\sigma_{\mathrm{H}},\theta\right) = \varepsilon_{f0}\mu_{hyd}(\sigma_{\mathrm{H}})\mu_{dev}(\theta) \tag{2.38}$$

The damage rate was then defined as:

$$\dot{D} = \frac{\dot{\bar{\varepsilon}}}{\varepsilon_f} \tag{2.39}$$

which is a consequence of the very important, though pretty intuitive, hypothesis made by Xue [22]:

"*The damaging process is self-similar with respect to the ratio of the plastic strain to the fracture strain on any deviatorically proportional loading path at any given pressure*"

This formulation allowed also Xue to provide a damage coupling, although this feature is not used in the more common formulation of the criterion given in [4].

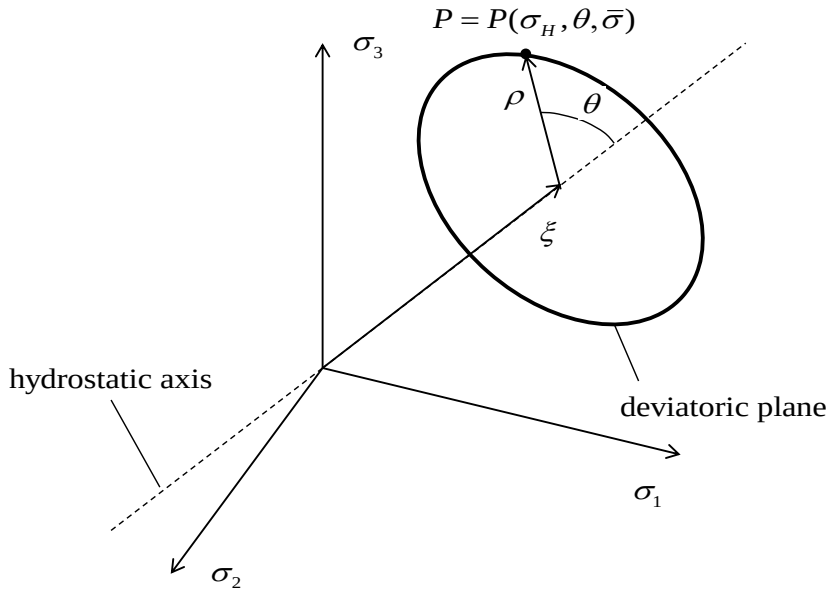

Figure 2. 25 – Haigh-Wasteergard stress space.

The relation between the Haigh-Wasteergard coordinates (ξ, ρ, θ) and the more physical variable used by Xue $(\sigma_H, \bar{\sigma}, \theta)$, as indicated in Figure 2.25, are given:

$$\xi = \sqrt{3}\sigma_H \quad (2.40)$$

$$\rho = \sqrt{\frac{2}{3}}\bar{\sigma} \quad (2.41)$$

while the Lode angle definition remains unvaried.

Xue used a power law influence of the hydrostatic pressure on formability $\mu_{hyd}(\sigma_H)$ with a cut-off value, while the Lode dependency was described on the *strain deviatoric plane* in a parametric formulation. The chosen parameter is γ defined as the ratio of the formability limits previously described (see Figure 2.12 and Equation (2.6)):

$$\gamma = \frac{\varepsilon_f(\chi = 0.5)}{\varepsilon_f(\chi = 0)} \quad (2.42)$$

Figure 2.26 highlights the Lode dependency of formability on the deviatoric plane of strains.

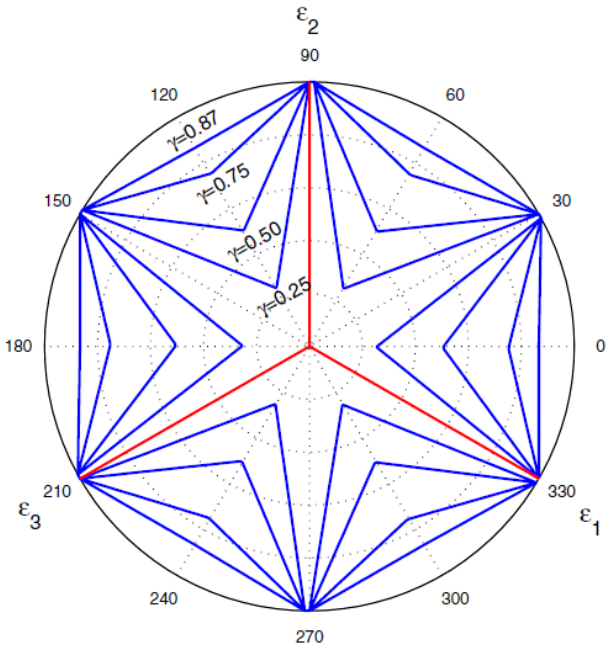

Figure 2. 26 – Lode dependence on the deviatoric plane [22].

Figure 2.27 illustrates the complete fracture locus in space of the main components of the strain tensor.

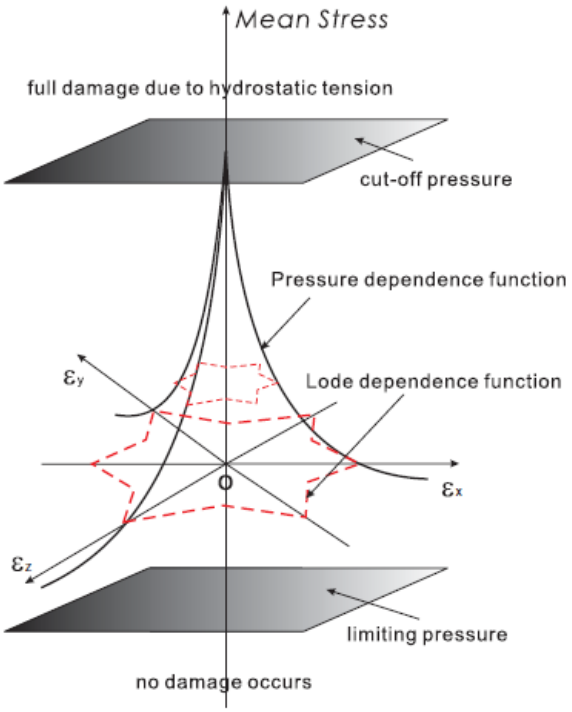

Figure 2. 27 – Fracture locus in the principal strains space [22].

For more practical purposes this formulation was modified as indicated in [4] assuming elliptical Lode-dependency and exponential triaxiality-dependency:

$$(2.43)\quad \varepsilon_f = F(\eta, X) = C_1 e^{-C_2\eta} - (C_1 e^{-C_2\eta} - C_3 e^{-C_4\eta})\left(1 - X^{\frac{1}{n}}\right)^n$$

Equation (2.43) corresponds to the fracture locus shape showed in Figure 1.3 illustrated in Chapter 1. In this formulation a new more practical parameter is used to define the stress deviator influence, usually called *deviatoric parameter*:

$$(2.44)\quad X = \cos(3\theta)$$

The hydrostatic component is as well expressed in terms of triaxiality rather than hydrostatic stress, linking this parameter to the Haigh-Wasteergard coordinates by means of the following relation:

$$(2.45)\quad \eta = \frac{\sqrt{2}\xi}{3\rho}$$

It is finally worth to underline that the n parameter in (2.43) is the strain hardening coefficient. As showed by Coppola et al. in [57], this fact is related to the Tresca maximum shear stress hypothesis for the fracture onset. Validation of this approach to several industrial cases was provided by Bariani et al. [58, 59].

One recent work by Graham et al. [60] provided a full experimental fracture locus calibration in the (η, X, ε_f) space by means of tensile-torsion tests. The resulting surface is shown in Figure 2.28.

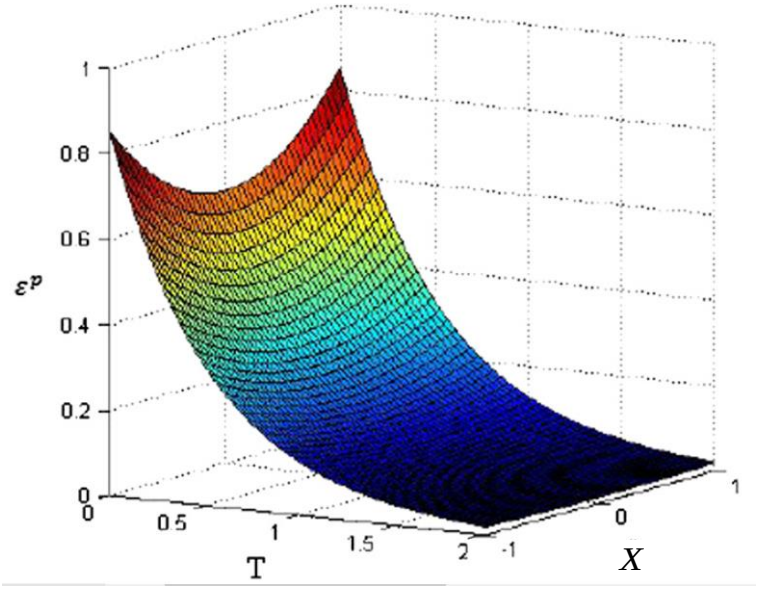

Figure 2. 28 – Fracture locus as determined by Graham et al. [60].

In the last years a series of works providing different analytical expressions of the Lode and triaxiality dependence of the strain at fracture were provided by assuming different criteria for fracture:

- in [61] Bai and Wierzbicki extended to ductile fracture applications the Mohr-Coulomb criterion;
- in [62] Lou et al. proposed a new shear-controlled criterion which was further improved in [63, 64].

In all the cases the resulting fracture loci had a shape similar to that of Figure 2.28, being the analytical formulation of the shear influence on fracture the only remarkable difference.

II.3.4 Hot damage modelling

Research efforts on hot damage numerical modelling have been by far less intense than those on cold ductile damage modelling, probably because of the higher complexity of the phenomenon and also because of the usually misleading perception of the formability as a secondary issue at high temperatures. A review on the little amount of works in literature on this topic is carried out below.

The approach to hot formability analytical modelling always consists in generalizing to the effect of temperature (and other thermal variables, such as strain rate) a standard cold fracture criterion:

$$D_{HOT}\left(\sigma_{ij},\varepsilon_{ij},T,\dot{\varepsilon}_{ij}\right)=D_{COLD}\left(\sigma_{ij},\varepsilon_{ij}\right)f\left(T,\dot{\varepsilon}_{ij}\right) \quad (2.46)$$

Another common practice in these works consists into using the Zener-Hollomon parameter (already defined in Equation (2.8)) to simplify the experimental plan or to the expression of the temperature function:

$$f\left(T,\dot{\varepsilon}_{ij}\right)=g\left(Z\right) \quad (2.47)$$

Zhu et al. [5] in their work provided an extension of the normalized Cockroft and Latham criterion for a Ti alloy at high temperatures. They also found a linear correlation of the material formability with the Zener Hollomon parameter, which is reported in Figure 2.29. They finally plotted a fracture locus (already reported in Figure 1.4) that showed a linear trend.

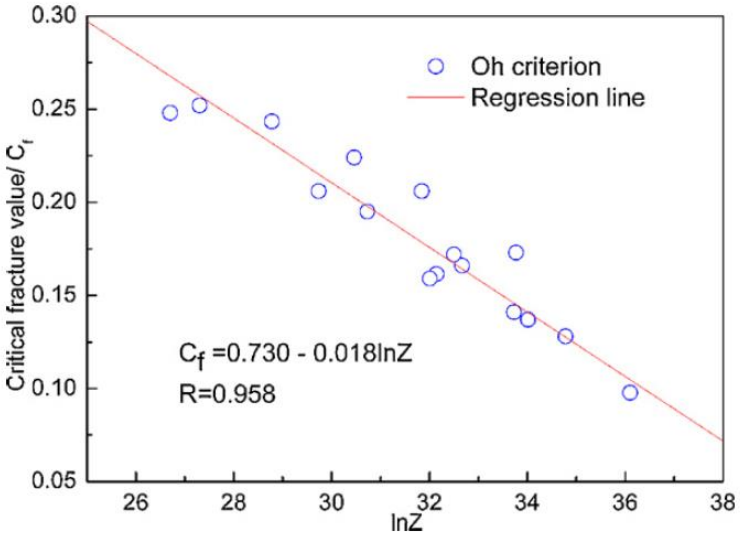

Figure 2. 29 – Linear formability - Zener-Hollomon parameter correlation [5].

However they did not provide any validation of the model, since the work was mainly focused on the optical acquisition system.

Zhang et al. [65] carried out a very similar work on the same alloy using the Oyane-Sato model and finding the same linear dependence.

Alexandrov et al. [29] carried out a tensile test campaign for different temperatures and strain rates in the hot range for three aluminium alloys. Referring also to [66], they found that the linear correlation with the Zener-Hollomon parameter can be established only for temperature below the maximum formability value (i.e. before hot shortness onset), because at higher temperatures the correlation gets scattered and no more linear.

They also calibrated the Oyane-Sato model extended to Zener-Hollomon parameter and provided an interesting calibration technique, but no validation case was provided.

More recently Khan and Liu [67] proposed an interesting extension to high temperatures and strain rates of the fracture criterion they previously proposed for cold conditions [68] based on the magnitude of the stress vector. However their study is not provided with any validation and the damage is expressed in terms of stresses and no link with strain at fracture is explicitly provided, making it difficult to use for practical purposes. Moreover in the tested temperature range the material formability seems to behave linearly without any apparent microstructural effect.

One recent work by He et al. [69], at last, provides an extension of the Oyane-Sato criterion to hot conditions by using an innovative formulation of the strain at fracture dependence on temperature and strain rate:

$$\bar{\varepsilon}_f = K\dot{\varepsilon}^a \left[\exp\left(\left(-\left| \frac{1}{T} - \frac{1}{T_C} \right| \frac{Q}{R} \right) \right) \right]^b \quad (2.48)$$

in which T_C is the *critical temperature*, namely the temperature at which formability reaches a maximum. R is the universal gas constant, while Q is the material viscous flow activation energy, in agreement with the Arrhenius rheological model:

$$\dot{\varepsilon} = A\sigma^N \exp\left(-\frac{Q}{RT} \right) \quad (2.49)$$

The other model constants are empirical coefficients.

He calibrated the model using tensile tests carried out on an alloy steel and found very good correspondence with the material formability behaviour, as shown in Figure 2.30. He's model has an increased capability of representing formability non-linearity, such as the hot shortness onset, however the model formulation is still quite simple since it cannot model interactive effects between strain rate and temperature and the validation of the approach was performed on laboratory hot tensile tests.

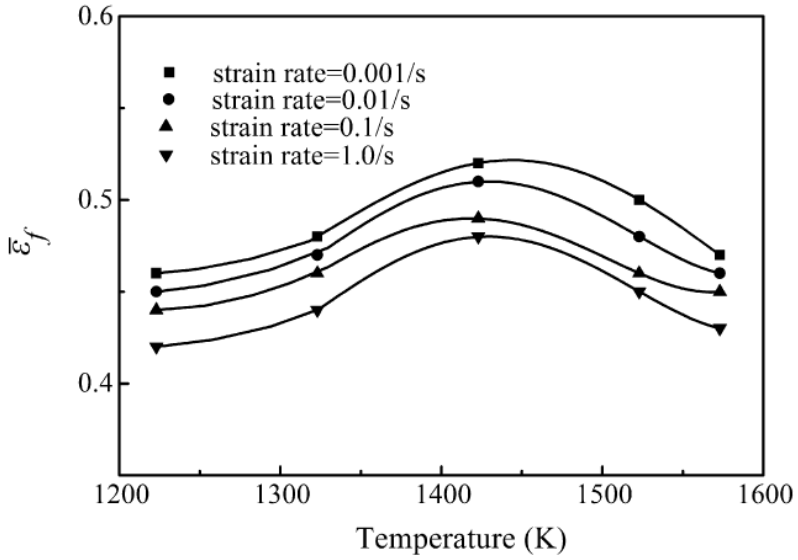

Figure 2. 30 – Temperature and strain rate-dependent formability model fitting [69].

II.4 RELEVANT EXPERIMENTAL OUTCOMES ON THE HOT FORMABILITY OF LIGHT ALLOYS

While it is undoubted that hot formability analytical modelling is a topic that gathered little attention from the research world, the other side of the coin consists in the huge amount of experimental studies on it, both for bulk and for sheet metal processes. In many studies, moreover, accurate microstructural analyses are performed in order to investigate the microstructural reasons of unexpected formability behaviours. Making a complete review of this literature would lead to a long treatment and anyway it is not in the purposes of this work.

Anyway, a brief review on the more interesting works of the last decade on this topic is here done focusing on the experimental evidences about non-linear or counterintuitive formability behaviours of light alloys at high temperatures. This is consistent with the study case material and type of process.

An extended experimental study on the microstructure of AA6082 alloy was carried out by Mrówka-Nowotnik [71, 72, 73]. In this study the effects of the intermetallic precipitates both on the material characteristics and on the fracture mode at room temperature are investigated. The outcomes of greater interest for this work are that the Mg_2Si intermetallic is one of the main responsible for the precipitation hardening effect as well as for the crack formations.

Lassance et al. [71] presented a work modelling at the micro-scale the fracture mechanisms of AA6XXX alloys in cold up to hot conditions. Most part of the work is on the model development, which is not of interest for meso-up-to-macro-scale formability modelling, however in this work two interesting results are provided:

- the material investigated displays a negative strain rate influence for all the temperature range (see Figure 2.31);
- a temperature-induced ductility drop is observed at 570°C and is related with the eutectic melting reaction Al + Si(+Mg_2Si) + b-Al_5FeSi → liquid.

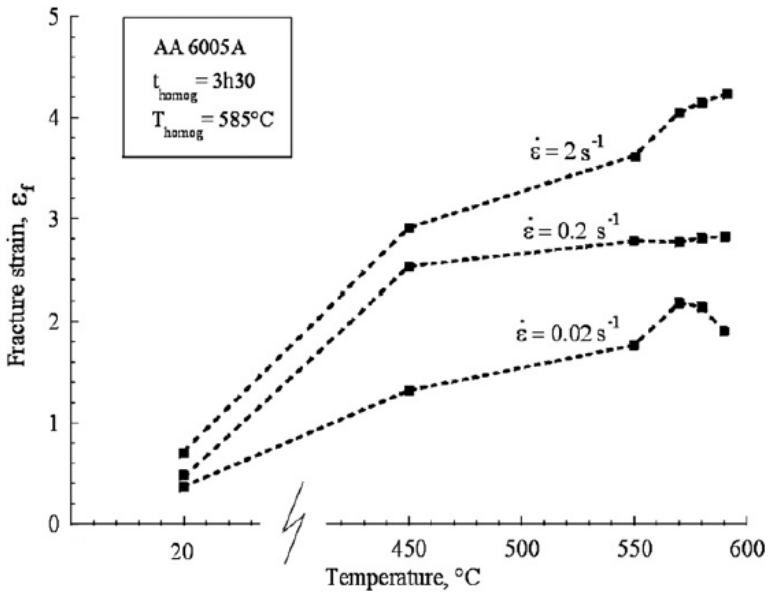

Figure 2. 31 – Negative strain rate influence on AA6005A alloy [71].

Chang et al. [28] carried out a large tensile test campaign on sheet metal specimens of AA5182 alloy spanning the warm and the hot range for different strain rates. Complex strain rate dependency by temperature and strain rate was found:

- at low temperatures (100-350°C) a positive strain rate sensitivity was detected;
- at high temperatures (350-400°C) a negative strain rate sensitivity was detected.

The strain at fracture as a function of the Zener-Hollomon parameter was plotted as a results in Figure 2.32. It is interesting to notice that, as a confirmation of what also found by Alexandrov et al. [29], the Zener-Hollomon linear dependence of formability can be established only for low temperatures or high strain rates (right hand side of the chart in Figure 2.32), namely for high temperature-compensated strain rate values.

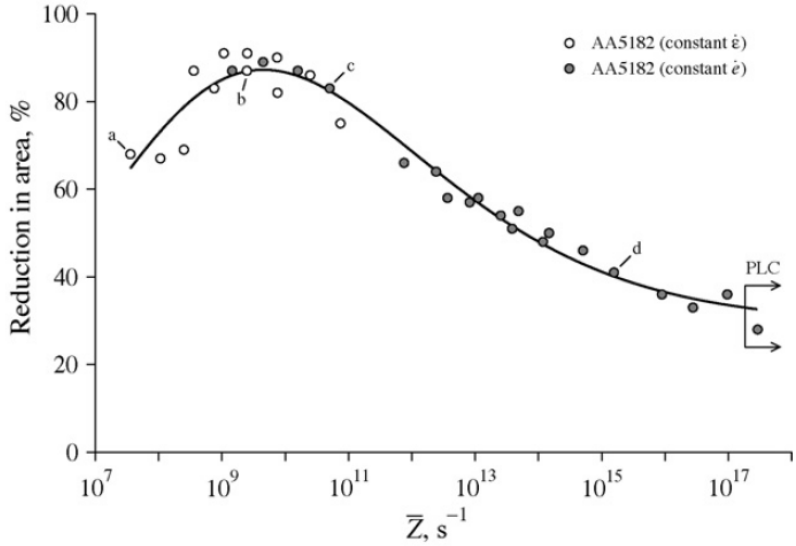

Figure 2. 32 – Strain at fracture as a function of Zener-Hollomon parameter [28].

Bariani et al. [74], finally, found a similar behaviour in the AA5083 alloy.

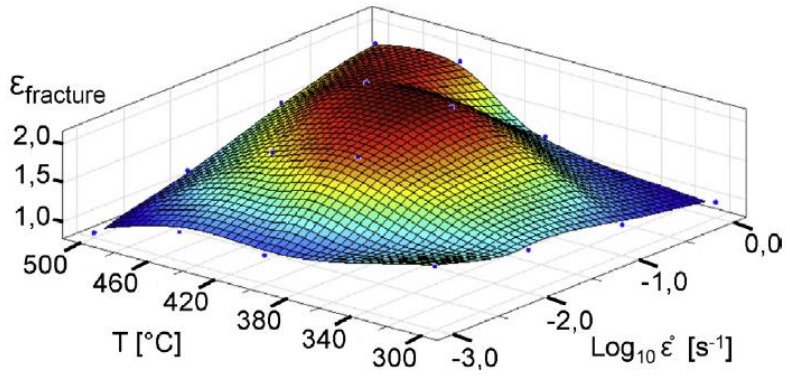

Figure 2. 33 – Fracture locus of AA5083 [74].

II.5 THE CROSS WEDGE ROLLING PROCESS

Cross wedge rolling (CWR) is a metal forming technique used in the manufacturing of stepped rotational parts. In this process, which can be carried out both in cold and in hot conditions, a cylindrical bar is plastically deformed reaching an axisymmetric final shape, by the action of wedge shape dies moving tangentially relative to one another. The dies shape and number can vary, but the three are the most common configurations: flat-

wedge, two-roll or three roll cross wedge rolling, as illustrated in Figure 2.34, taken from the already cited work by Li et al. [6].

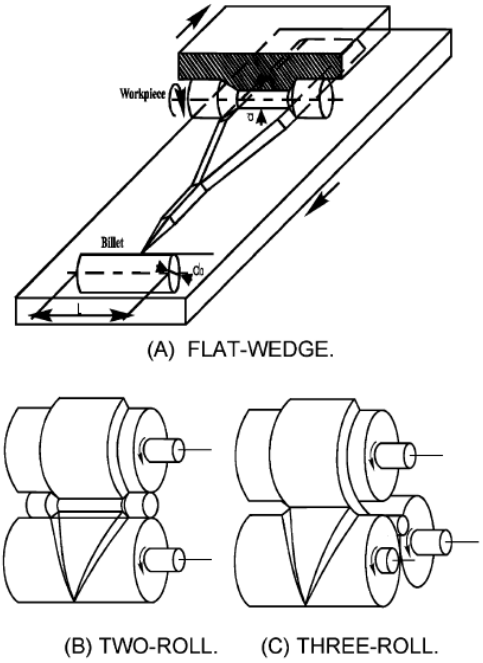

Figure 2. 34 – Most common dies configurations in CWR [6].

Shafts with tapers, steps, shoulders, and walls with almost no draft angles can be made using the CWR technique. It has been reported by Hu et al. [75] that hundreds of different kinds of products—ranging from crankshafts to drill bits—are currently being manufactured by CWR worldwide. Figure 2.35 outlines a sample of cross wedge rolled parts.

Figure 2. 35 – Typical components that can be attained by CWR.

CWR entails significant benefits, if compared with other traditional processes, namely:

- higher toughness products;
- higher production rates;
- lower unit cost, if produced batches are large enough.

Because of these advantages, the CWR technique has become extremely popular, but it is still not adopted by many companies essentially for the difficulties of developing automated CWR tooling design procedures, which is essentially linked to the fact that the deformation and failure mechanisms of CWR are still largely unknown in the industrial world [6].

Johnson and Mamalis [76] identified three main categories of defects in CWR:

- improperly formed workpiece cross-section; which can be for example due to low friction at the rolls-part interface which causes slipping which in turn prevents the part from a correct rotation leading a non axi-symmetric shape. These kind of defects can also be linked with the part necking for excessive stretching;
- surface defects; examples of these defects are folding, grooving or surface cracking, which can be usually all linked to the dies geometry that cause incorrect material flow;
- internal defects; which are the most dangerous since can be difficult to detect and even more difficult to prevent by wise design and that are linked with the so-called Mannesmann effect.

Figure 2.36 [6] illustrates three examples of defects in CWR.

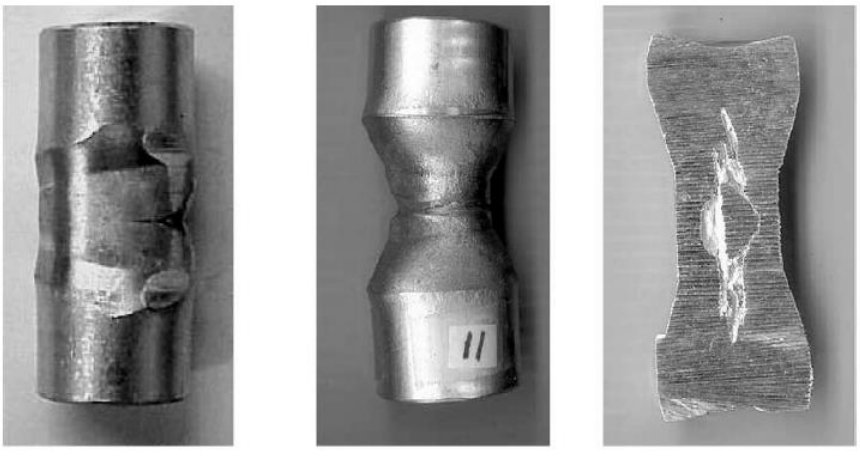

Figure 2. 36 – Three main defects in CWR [6].

In their already mentioned work Li et al. [6] carried out an extensive experimental study on cross wedge rolling to investigate the fracture mechanisms and the main influence parameters, testing more than fifty different operating conditions. In this work the internal cracking was recognized as the more critical issue for this process, since it is the most difficult to predict and control. The authors studied experimentally the effect on internal cracking of three geometrical parameters directly or indirectly linked with dies geometries, namely:

- area reduction;
- forming angle;
- stretching angle.

They finally proposed the definition of a *deformation coefficient* suitable as a guideline for dies design.

Pater, on the other hand, in three successive works [77, 78, 79] developed a theoretical and experimental analysis devoted to the CWR, in which the primary concern is to develop a procedure to predict and avoid improperly formed parts, neglecting the axial cracking. The procedure allows to derive process maps in which a *stable area* is identified in which the process can be carried out safely, while two other areas are identified in which defects appear, namely the *necking area* and the *slipping area* (see Figure 2.37). The approach do not need numerical simulation and was experimentally validated, also with the results of other authors [80].

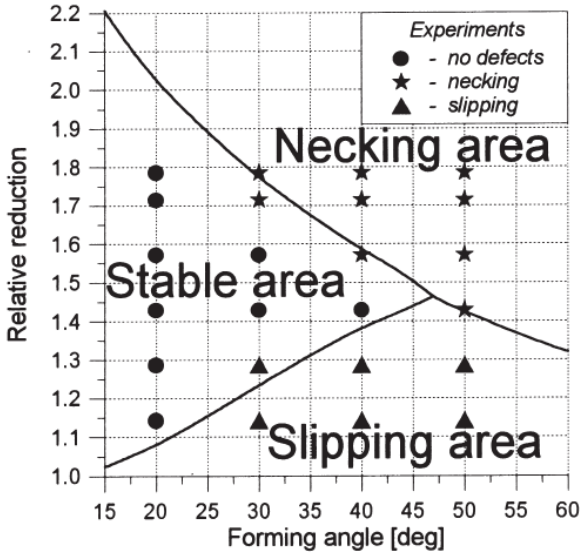

Figure 2. 37 – Effect of forming angle and relative reduction on CWR stability [78].

The limits of the work of Li et al. and of that of Pater is that of many analytical solutions of complex forming processes, namely that their formulations are geometry-dependent and thus cannot be applied in a general case.

In the last years, with the wide spread of FE numerical simulation, a series of studies were published on the CWR numerical simulation.

Fang et al. [81] analysed the stress distribution using a rigid-plastic material model finding that at the bar axis both the maximum principal stress value and the maximum hydrostatic pressure value take place. They finally linked the wedge angle with the force components on the rolls.

In their work Lee et al. [82] modelled the Mannesmann fracture onset on a cold cross wedge rolling case, evaluating different empirical criteria and finally building a process formability map as a function of friction and of the shoulder angle of the wedge, while Liu et al. [83] also modelled a cold cross wedge rolling case using the Oh criterion and providing a validation which is shown in Figure 2.38.

A common outcome of all these works is that Mannesmann effect is responsible for axial crackin entailing tensile (and cyclic) stress states both in the radial and in the axial direction, the importance of these two components depending mainly on the rolls geometries but also by the other process parameters.

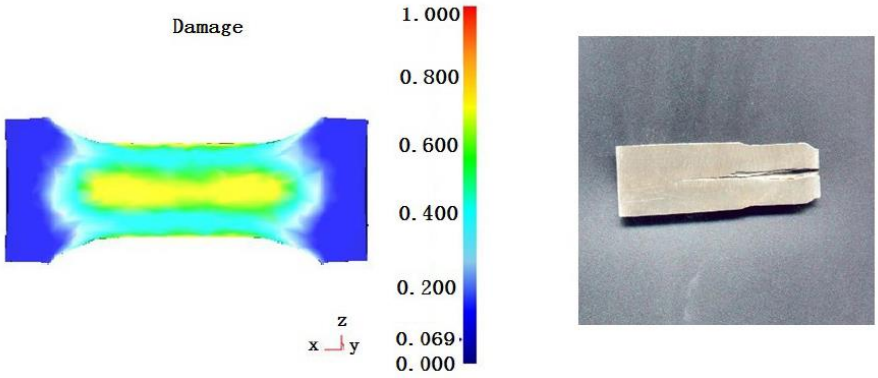

Figure 2. 38 – Validation case of axial cracking prediction provided by Liu et al. [83].

Silva et al. [84], finally, proposed a study applying to a cross wedge rolling process carried out at elevated temperature the Oh criterion, under the assumption of constant temperature. However the model was probably too simplifying since the crack onset was correctly predicted in some process conditions, while in other ones the fracture zone was mis-identified at the bar surface.

At present no work has been found either providing the use of stress deviator dependent criteria, for cold processes, or the use of temperature dependent criteria for hot ones.

III CHAPTER

THE APPROACH

Finite Element numerical simulation has become a key technology for material forming process optimization in particular for crack prediction. However this tool needs both reliable models and accurate experimental calibration to provide useful results. An additional requirement for practical industrial application is the ease of experimental calibration and numerical implementation.

The scientific literature has been mainly concerned on ductile fracture modelling at room temperature while hot formability was faced essentially extending to hot conditions the simplest models developed for cold conditions and adopting a purely empirical approach for temperature and strain rate influence modelling. The few works providing analytical models for hot formability still show the following lacks:

- they model the material formability in quite a simple way, not allowing an accurate representation of the complex microstructural phenomena that can take place at high temperatures;
- they usually do not provide experimental validation of the models proposed and, even when they do, the validation case is always a simple experimental test carried out under simple and homogeneous themo-mechanical conditions.

The main target of this work is indeed to overcome this two lacks, providing a tool:

- capable of predicting hot ductile frecturee in complex and time-variable themo-mechanical conditions and also to describe it with acceptable accuracy in changing-fracture mode regimes;
- easy to be experimentally and numerically calibrated.

To this aim the hot cross wedge rolling process of a precipitation-hardened aluminium alloy showing Mannesmann axial cracking was chosen as reference study case. Its relevance is due to two reasons:

- cross wedge rolling is a process of increasing industrial use due to its interesting technological features;
- the material is a widely used light alloy which has microstructural characteristics (typical also of other materials families) that can imply highly non-linear formability behaviour.

A scheme summarizing the combined numerical-experimental techniques adopted in this research is reported in Fig. 3.1:

- *process FE preliminary simulation*; in order to determine the thermo-mechanical conditions evolution at the crack onset zone in order to identify the best damage modelling strategy as well as the best experimental campaign to calibrate it;

- *experimental campaign*; for the material rheological and formability characterization;
- *damage model development and calibration*; starting from the critical assessment of the experimental outcomes two damage modelling strategies are proposed: the first one is a purely empirical regression on experimental data, while the second one consists in the elaboration of a new physically-based model. Both models are then calibrated: the first one by inverse FE simulations, while the second one by direct calibration;
- *validation*; both models results are critically compared with the results from industrial trials.

The prediction capabilities of the proposed model as well as the possibility for its usage for process maps virtual extrapolation are finally discussed.

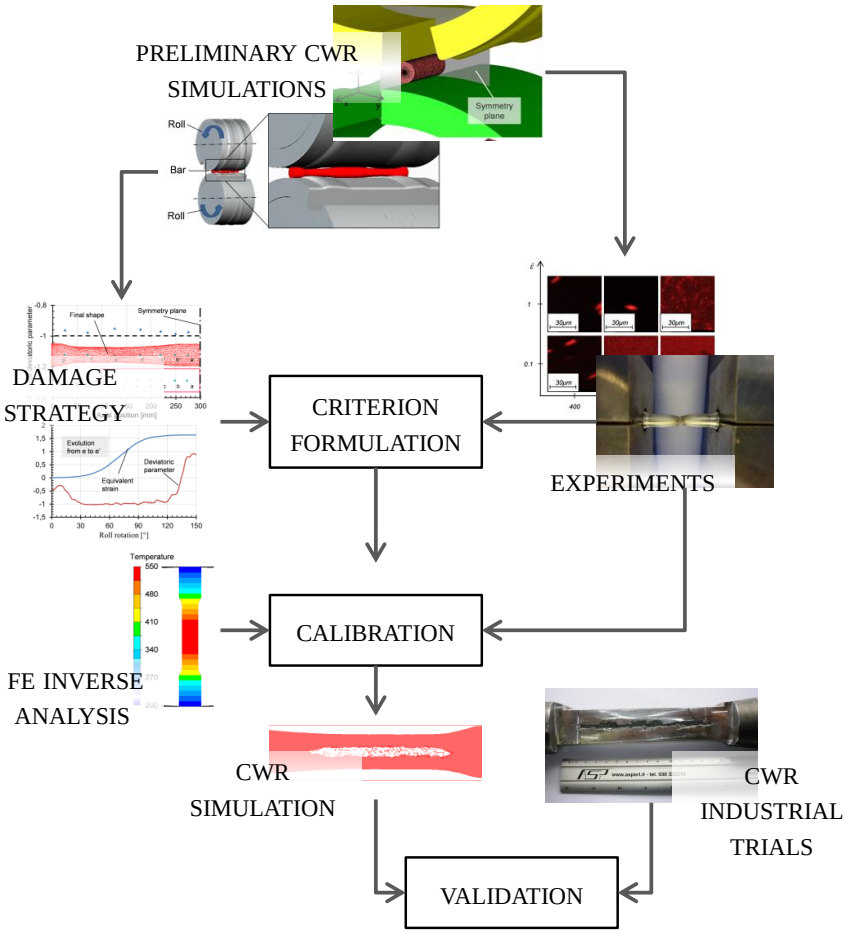

Figure 3. 1 – Schematic flow diagram of the work approach.

IV CHAPTER

CROSS WEDGE ROLLING FINITE

ELEMENT NUMERICAL MODEL

IV.1 INTRODUCTION

This chapter is dedicated to the description of the FE numerical model of the cross wedge rolling process which is the industrial reference case of this work. As stated in the previous chapter about the approach, in this work the FE process simulation is not used only to provide the validation case, but is also to carry out a preliminary numerical campaign to investigate the thermal and mechanical conditions in the part during the process. This is made to provide useful data both for a proper experimental campaign choice and for the new damage model definition.

The first part of the chapter is dedicated to the description of the industrial study case in terms of part and tooling geometries, material and process parameters, focusing also on the crack issues that were detected and on the other process constraints.

In the second part the numerical model is presented in detail: the physical phenomenon modelling assumptions are described in terms of tooling kinematics and stiffness, material characteristics, friction and thermal exchange. Particular attention is also dedicated to the numerical parameters settings such as mesh size and computation time step.

In the last part the results of the preliminary simulations are showed and elaborated. Important conclusions on the stress state are drawn that will be used in the following chapters.

IV.2 THE INDUSTRIAL CASE

IV.2.1 General process description

The industrial reference case consists in the forming of a cylindrical aluminium bar by means of two shaped rolls which rotate in opposite directions, also known as cross wedge rolling and previously described in chapter 2.

The process is the second stage of the forming sequence of a light-weight car suspension component carried out at high temperatures. The production sequence includes:

1. Oven heating up to process temperature;
2. Cross wedge rolling;
3. Bending;
4. Re-heating stage;
5. Forging;

6. CN machining up to final shape.

The cross wedge rolling stage, thus, is used to obtain a semi-finished part for successive forming operations and has been introduced in the process chain in order to reduce the material waste and increase the production rate.

Figure 4.1 shows a schematic illustration of the process setup: the part is formed by two symmetrical wedges on the rolls to reach a double-dog-bone final shape.

IV.2.2 Process parameters and constraints

The material used is the AA6082-T6 alloy, which is one of the most common precipitation hardened magnesium-silicon-base aluminium alloys. Table 4. 1 shows its nominal composition ranges.

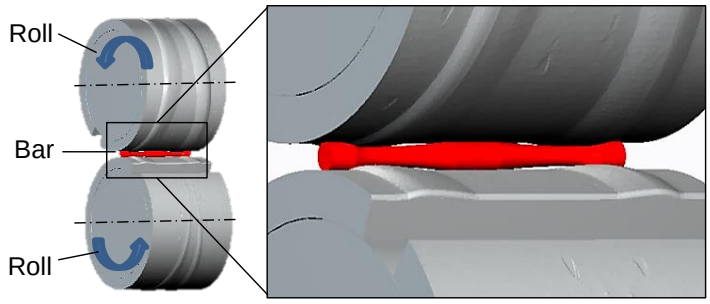

Figure 4. 1 – Reference cross wedge rolling case.

Alloying element	Weight%
Cr	0.0÷0.25
Cu	0.0÷0.1
Fe	0.0÷0.5
Mg	0.6÷1.2
Mn	0.4÷1.0
Si	0.7÷1.3
Al	Balance

Table 4. 1 - AA6082-T6 chemical composition.

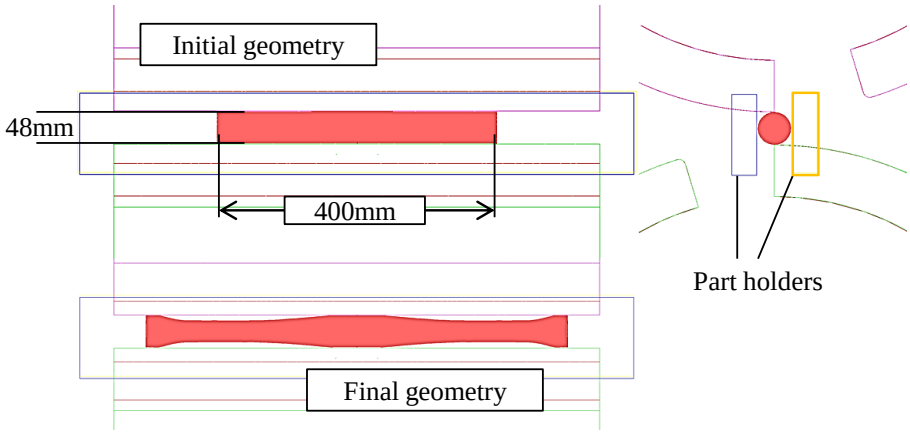

Figure 4. 2 – Schematic illustration of the process.

The raw bars are heated up to process temperature in an electric furnace and then automatically transferred in the cross wedge rolling mill in which they are formed by the rolls. Two bar holders provide to keep the bar in the correct axial position during the process. Figure 4.2 shows the process tooling setup as well the initial and final bar shape.

The two principal process parameters that can be set are:

- *furnace temperature*; which is a critical constraint since a temperature lower than 450°C would cause excessive grain coarsening reducing the mechanical characteristics of the part. On the other hand, processing at higher temperatures has been proven from industrial trials to cause Mannesmann axial cracking, as illustrated in Figure 4.3;

Figure 4. 3 – Axial cracking resulting from cross wedge rolling at 510°C.

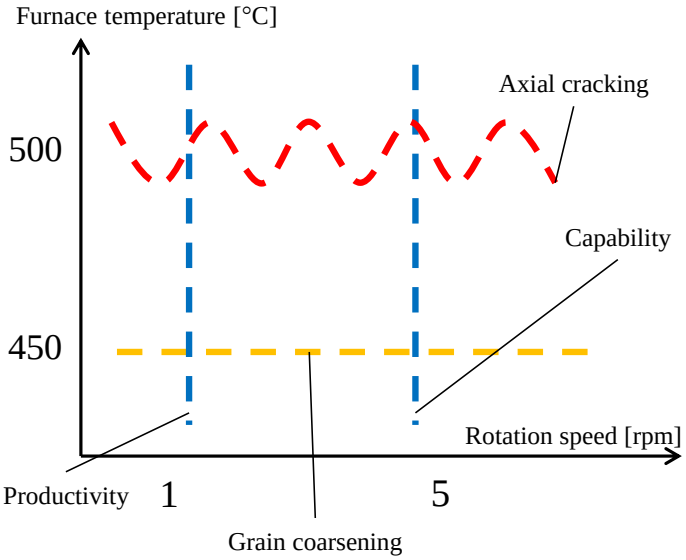

Figure 4. 4 – Process parameters constraints.

- *rolls rotation speed*; which is necessarily linked to the process production rate for its lower limit and to the plant capability for its upper one. The standard rolling speed was comprised in the 2÷4 rpm range.

These constraints imply quite a narrow process window, as illustrated in Figure 4.4.

IV.3 THE NUMERICAL MODEL

The process has been modelled using Forge 2011™ commercial code by Transvalor®. A 3D thermo-mechanical implicit modelled was used and a series of simplifying assumptions were taken in order to properly model the process. Optimal numerical parameters were also established.

IV.3.1 Tooling properties

The following settings have been implemented on tooling:

- *rigid dies*; both the rolls and the holders have been modelled as rigid dies. This is a common assumption for low speed-hot forging and is a fortiori justified by the use of a light alloy;
- *part-die interpenetration*; a maximum part-die interpenetration of 0.1 mm was set following the code provider guidelines [83];

- *die kinematics*; no simplifying assumption had to bet set for die kinematics, since a constant rotation speed is set in the industrial process;
- *dies temperature*; as resulting from in-line measurements, a constant temperature of 240°C was set for the rolls and holders surfaces.

IV.3.2 Part properties

The *material mechanical behaviour* was modelled neglecting the elastic deformation (see Figure 4.5) and using the Hansel-Spittel visco-plastic model. A standard data-base model was used for the preliminary simulations, while, after the rheological experimental campaign, the calibrated material model was used. The full 9-coefficients Hansel-Spittel formulation was used, as indicated in Equation (4.1):

$$\sigma = \mathrm{A}\varepsilon^{m_1 T}\varepsilon^{m_2}\dot{\varepsilon}^{m_3}e^{\frac{m_4}{T}}(1+\varepsilon)^{m_5 T}e^{m_7\varepsilon}\dot{\varepsilon}^{m_8 T}T^{m_9} \tag{4.1}$$

Standard database values for aluminium alloys were assumed for all the other physical constants, as summarized in Table 4. 2.

Physical constant	**Value**
Densitiy [kg/m3]	2800
Specific heat [J/kgK]	1200
Conductivity [W/mK]	250
Emissivity [-]	0.05
Linear thermal expansion [K-1]	23e-6

Table 4. 2 – AA6082-T6 other physical constants.

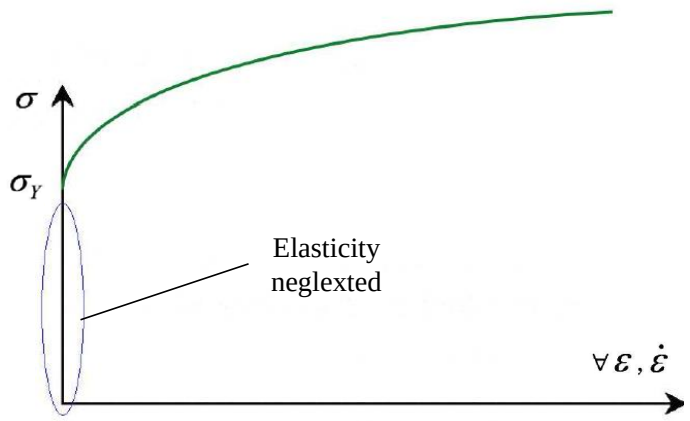

Figure 4. 5 – Visco-plastic material behaviour flow curve [83].

Due to the reduced transfer times, as also confirmed by in-line pyrometer measurements, *the part initial temperature was assumed to be constant and equal to the furnace temperature*.

IV.3.3 Friction and heat transfer model

Friction between tools and part was also modelled making an usual assumption for hot forging [83] which consists in neglecting the Coulomb ramp and assuming pure-Tresca law, as showed in Figure 4.6. Since no sliding at the die-part resulted in the industrial trials, a high friction value of $m = 0.8$ was set.

Heat exchange was also modelled with the suggested parameters [83] for metal-metal pressure contact and no oxide layer, while the ambient temperature was set 40°C and also the dies effusivity was modelled. A standard value for natural convection in cool air was chosen for the ambient heat exchange.

Table 4. 3 summarizes the friction and thermal exchange settings just described and implemented in the numerical model.

Parameter	**Value**
Tresca m coefficient [-]	0.8
Dies exchange coeff. [W/m^{2}K]	4000
Ambient temperature [°C]	40
Dies temperature [°C]	240
Dies effusivity [J/mKs$^{0.5}$]	1.2e+4

Table 4. 3 – Friction and heat exchange settings.

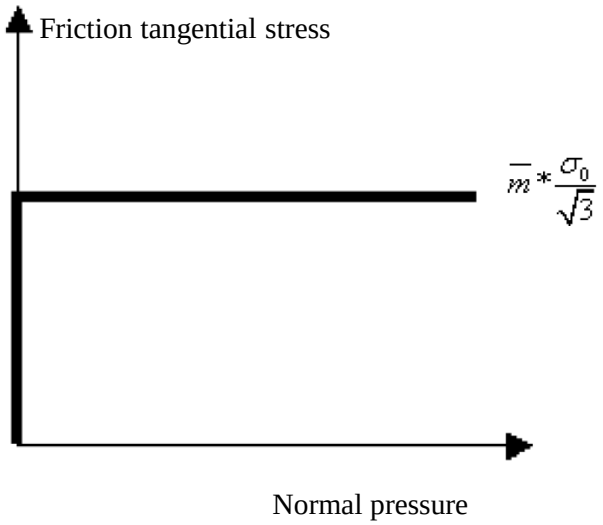

Figure 4. 6 – Tresca friction model.

IV.3.4 Numerical parameters

The two main numerical settings that can heavily affect the simulations results were carefully assessed and implemented:

- *meshing settings*; the standard 3D linear-tetrahedral mesh type was used for the simulation and two concentric refining mesh boxes were set along the bar axis, as illustrated in Figure 4.7. A series of simulations was run refining the mesh size and taking the Cockroft and Latham's damage as a calibrating parameter. Since the damage value increases with reducing mesh size, this calibration is particularly important. The mesh refinement was stopped when a difference of less than 5% was found in the resulting damage value. The results are shown in Figure 4.8;
- computation time step; also numerical time step is a particularly important setting since it can affect the convergence of the solution. Time step is linked with the speed field [33, 83] and must be set in order to avoid node displacement to overcome a certain fraction of the mesh size. The resulting time step was 0.01s.

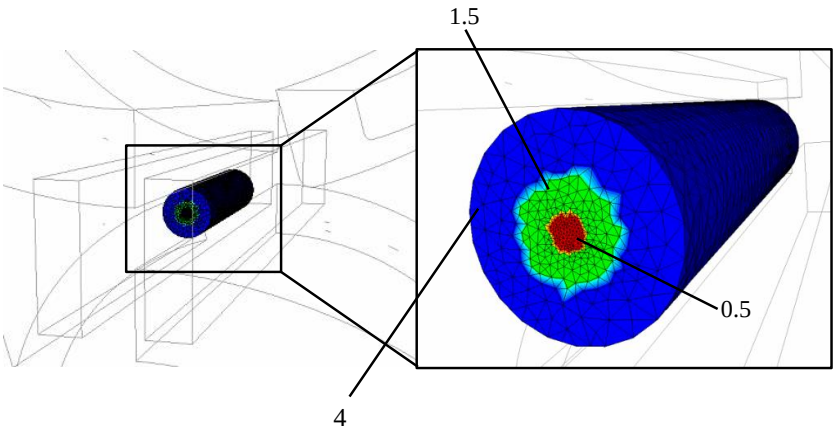

Figure 4. 7 – Optimal mesh refinement boxes.

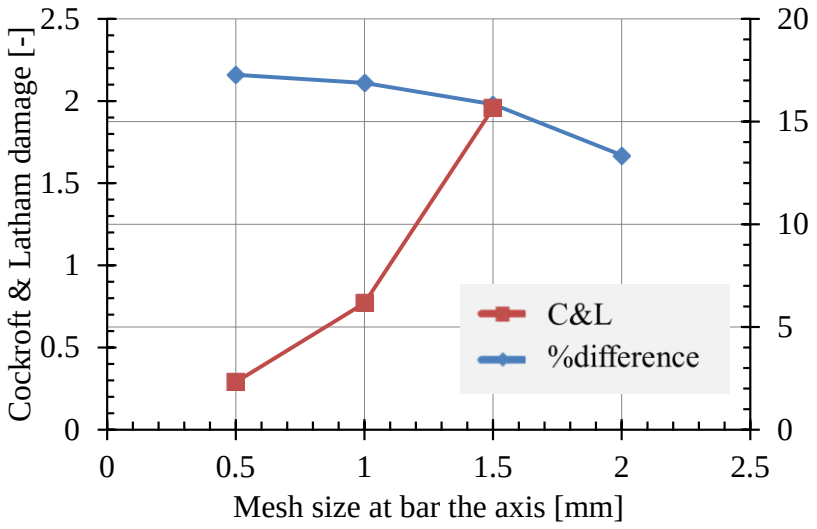

Figure 4. 8 – Mesh refinement optimization parameters.

Two other numerical settings were defined in order to reduce computation time and to monitor more accurately the evolution of the stresses and strain during the process:

- *a plane of symmetry*; allowing to simulate only half of the part domain. This is possible due to the geometries and load symmetrical conditions;
- *seven lagrangian sensors along the bar axis*; in order monitor more accurately the stress and strain distributions during the process simulation.

Figure 4.9 highlights these two settings.

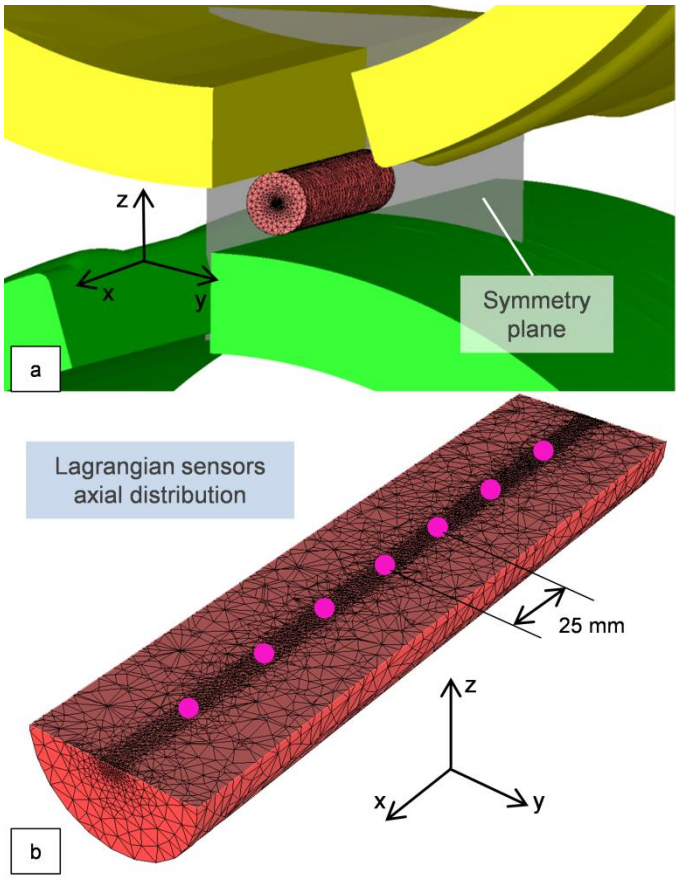

Figure 4. 9 – Plane of symmetry (a) and lagrangian sensors (b).

IV.4 PRELIMINARY SIMULATIONS RESULTS

Preliminary process simulations were run in order to investigate:

- the temperature distribution evolution during the process;
- the stress and strain fields evolution; in particular the triaxiality and deviatoric parameter evolution were assessed in order to provide a complete stress tensor description, as well as the strain rate distribution.

The resulting temperature distribution for an initial temperature of the part equal to 445°C is displayed in Figure 4.10. It is clear that the uneven deformation and contact conditions cause sharp temperature and strain rate gradients in the part during the process.

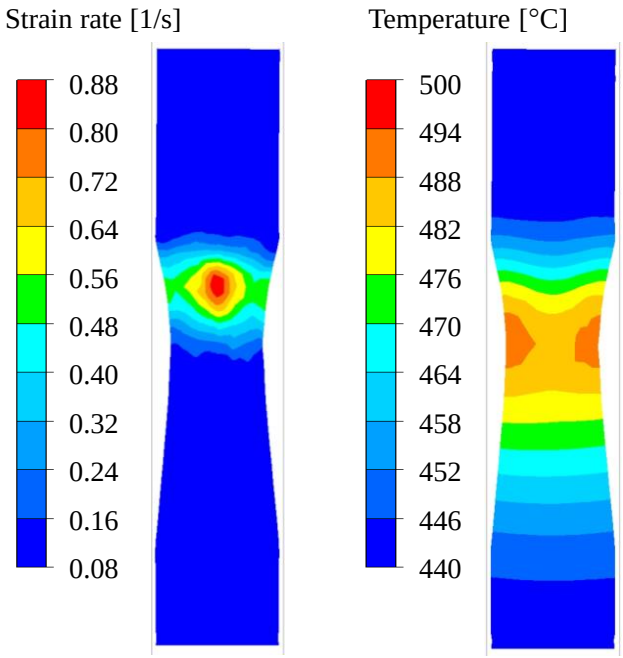

Figure 4. 10 – Temperature and strain rate distributions.

On the other hand the stress triaxiality and deviatoric parameter (defined in Equation (2.44)) trends measured by the lagrangian sensors were assessed. An example of them is shown in Figure 4.11 and Figure 4.12 compared with the equivalent strain evolution.

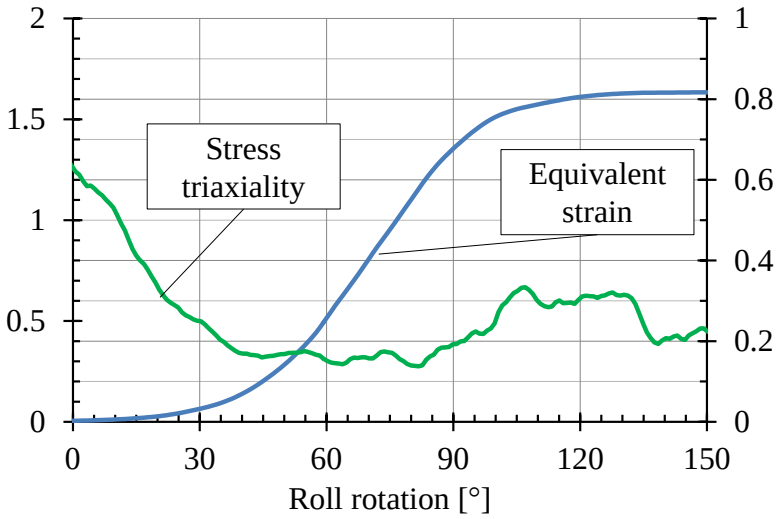

Figure 4. 11 – Stress triaxiality evolution during the process.

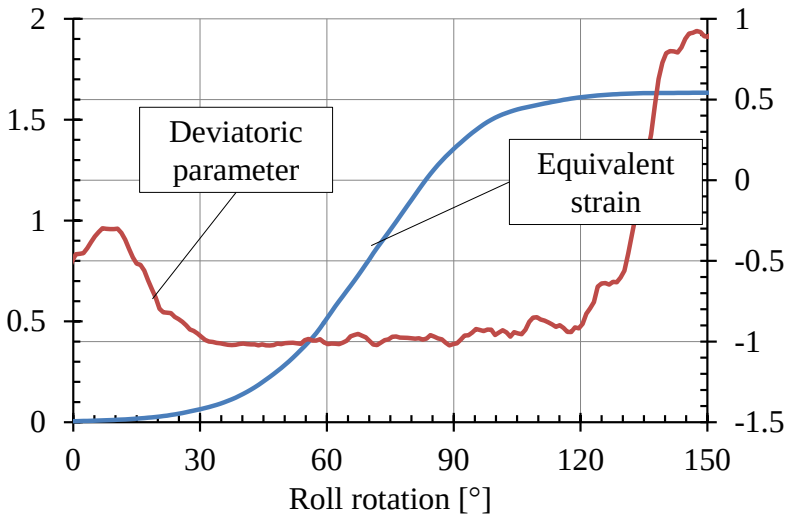

Figure 4. 12 – Deviatoric parameter evolution during the process.

The results can be summarized as follows:

- the stress triaxiality value during the deformation is comprised in the 0.15÷0.35 range;
- the deviatoric parameter is almost constant around the -1 value.

An average X value was calculated following the Wierzbicki method [4] as showed in Equation (4.2). A global average was calculated for the seven sensors and it was found equal to 0.97.

(4.2) $$X_{avg} = \int_0^{\varepsilon_f} X d\bar{\varepsilon}$$

This finding corresponds to the quite surprising fact that the stress state at the bar axis is axi-symmetrical and namely, following the definition reported by Graham [60], of *generalized compression*. This is a stress state corresponding to a uni-axial stress state with a hydrostatic tensile one superimposed.

A deeper analysis on the stress tensor components highlighted the fact that the stress axis of symmetry does not correspond to the bar axis, since one of the shear stress components in the cartesian reference system is non-zero (see Figure 4.13).

However, passing to the principal stress system, it can be seen, as reported in Figure 4.14, that two out of the three principal components are almost equal (green and red curve), confirming the fact that the stress tensor is circular in one direction.

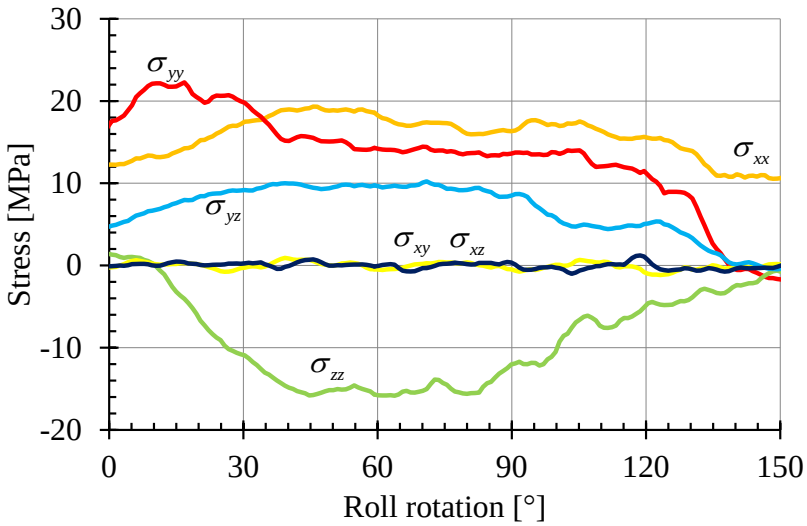

Figure 4. 13 – Cartesian components of the stress tensor evolution at the bar axis.

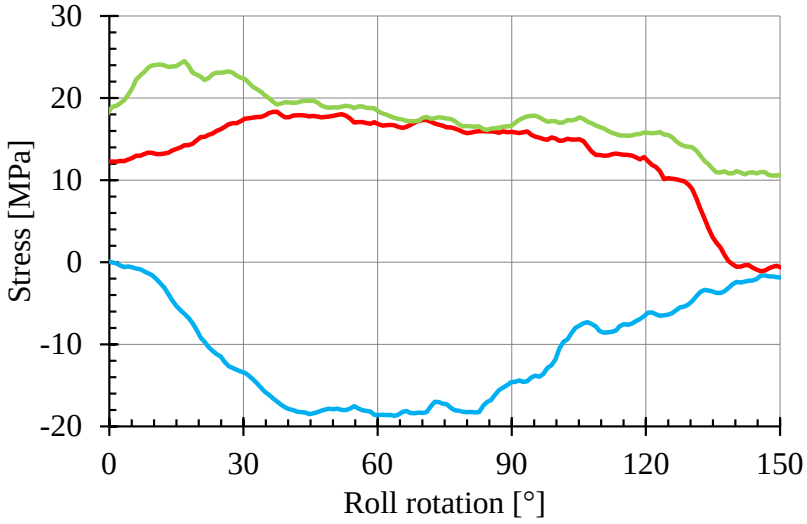

Figure 4. 14 - Principal components of the stress tensor evolution at the bar axis.

V CHAPTER

EXPERIMENTS

V.1 INTRODUCTION

This chapter is devoted to the description of the experimental campaign that was carried out to make the material model formulation and calibration as well as for investigating the fracture mode changes reasons.

In the first part the data provided by the preliminary process simulations are discussed and, together with the information about the industrial process parameters, are used to define the experimental plan.

In the second paragraph the material rheological characterization is described: the hot compression test experimental apparatus is firstly shown together with the raw experimental outputs. The data elaboration procedure to obtain the material flow curves is then described and at last the non-linear regression technique to calibrate the material rheological model is presented.

The third part concerns the formability characterization by means of a hot tensile test campaign carried out in the same conditions as those of the compression test campaign. The unexpected results are then investigated by means of SEM fractographic and EDS-micro-chemical analysis in order to provide the microstructural mechanisms that cause the fracture mode change.

The last paragraph is dedicated to a wider tensile test campaign that was carried out in order to have a large and sound experimental basis to support the formulation of the new fracture criterion. The experimental result of this last part consists in the material fracture locus expressed in the $(T\dot{\varepsilon}, \varepsilon_f)$ space.

V.2 EXPERIMENTAL PLAN DEFINITION

The simulations of Chapter IV highlighted several important facts about the thermo-mechanical conditions at the bar axis during the cross wedge rolling process:

- the strain rate distribution is very uneven and is localized in a zone on the axis moving towards the direction of elongation of the bar during the process; in that zone the strain rate is in the $0.3 \div 0.9\ s^{-1}$ range;
- the temperature distribution keeps quite uniform at the initial value in the unstrained zone, while in the zone which undergo the deformation there is a positive temperature gradient that can lead up to 60÷90°C differences if compared with the initial temperature;
- the stress triaxiality at the bar axis is not constant but it swings in the 0.15÷0.35 range, namely the medium triaxiality levels;

- the deviatoric parameter trend is almost constant during most of the deformation and equal to -1, indicating an axi-symmetric stress state.

These considerations were then used to define the experimental campaign. The axi-symmetry of the stress state allowed to search for experimental tests showing the same mechanical conditions, in order to keep as close as possible to the industrial process. The choice was then easy:

- compression test was chosen for rheological characterization, due to axi-simmetry of the stress state;
- tensile test on smooth specimen was chosen for formability characterization; in this case, besides the stress axi-symmetry, the need to avoid high triaxiality values led to discard the notched-specimen option.

As a last consideration, the most representative thermal conditions were considered and in particular:

- considering the temperature increases displayed by the FE simulations, a maximum test temperature about 50°C higher than the maximum furnace process temperature was chosen;

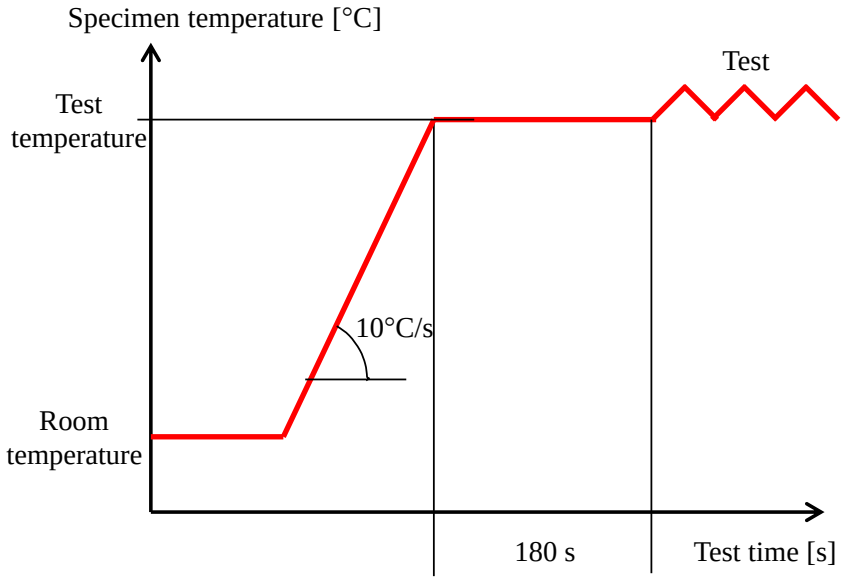

Figure 5. 1 – Test temperature profile.

- following the heat treatment guidelines provided in [65], a soaking time of 180s was set in order to simulate the homogenization time that the bars pass in the

furnace, without triggering any solubilisation phenomenon that would cancel the previous press hardening treatment of the alloy.

Thus it was stated to keep the same thermal conditions for both the compression and tensile test campaign. The test thermal profile is shown in Figure 5.1.

Finally the experimental plan common parameter are shown in Table 5. 1.

Table 5. 1 – Experimental plan

Test type	Compression test	Tensile test (smooth specimen)
Temperature [°C]	400, 500, 550	400, 500, 550
Strain rate [1/s]	0.1, 1	0.1, 1
Soaking time [s]	180	180
Heating ramp [°C/s]	10	10

Table 5. 1 – Experimental plan common parameters.

V.3 RHEOLOGICAL CHARACTERIZATION

V.3.1 Compression test apparatus and procedure

The compression tests have been carried out on the thermo-mechanical simulator Gleeble 3800™ illustrated in Figure 5.2. This is a hydraulic horizontal servo-press with accurate load, punch displacement and temperature measurement devices. The system is also provided by a servo-direct-conduction heating system capable to attain a wide range of temperatures and heating rates and by an automatic control on the punch displacement speed that allows to carry out tests at constant strain rate.

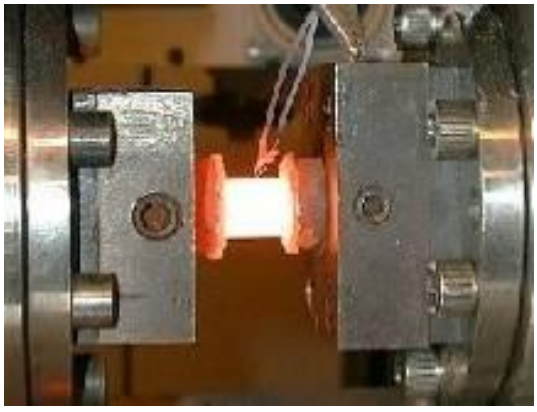

Figure 5. 2 - Gleeble 3800™ system in compression configuration.

Hot compression testing best practices have been followed and in particular at the interfaces between the punch and the specimen a proper interface has been set to minimize the effect of friction and the axial thermal gradient that can arise due to the fact that the punches act as heat sinks. A combination of two alternate foils of graphite and tantalum, acting respectively as lubricant and thermal barrier, has then been applied at the specimen-punch interfaces.

To provide accurate temperature measurement, which is also used by the system for the feedback temperature control, a K-thermocouple has been spot-welded on the specimen lateral surface. Figure 5.3 shows the compression test setup.

Raw material bar provided by the same production batch was used to realize the standard cylindrical specimens recommended for the Gleeble system: 12 mm diameter and 14 mm height.

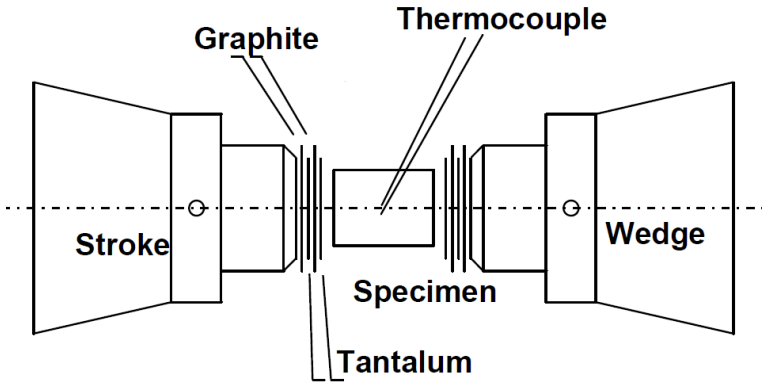

Figure 5. 3 – Schematic illustration of the compression test setup.

V.3.2 Rheological model calibration

Raw experimental compression tests data are provided by the system in terms of load-displacement curves. The standard elaboration in order to obtain the material stress-strain curves was carried out assuming uni-axial stress state and uniform deformation:

$$\varepsilon = \ln\left(\frac{h}{h_0}\right) = \ln\left(\frac{h_0 - displacement}{h_0}\right) \tag{5.1}$$

$$\sigma = \frac{F}{A} = \frac{F}{A_0 e^{\varepsilon}} \tag{5.2}$$

The flow curves where finally elaborated by means of a non-linear regression technique on the full Hansel-Spittel model described in Equation (4.1). The best fitting

model coefficients were found and are summarized in Table 5. 2. These data will be afterwards implemented in the process FE numerical model as material mechanical model. The flow curves are shown in Figure 5.4. The material mechanical behaviour presents the expected thermal softening and strain rate hardening behaviour. The experimental curves are compared with the model fitting curves showing good fitting for all the tested conditions.

Coefficient	**Value**
A	522.7
m_1	-0.0051
m_2	-0.1299
m_3	-0.1589
m_4	-0.0113
m_6	-0.0014
m_7	0.5123
m_8	0.00066
m_9	-0.0409

Table 5. 2 – Material rheological model constants.

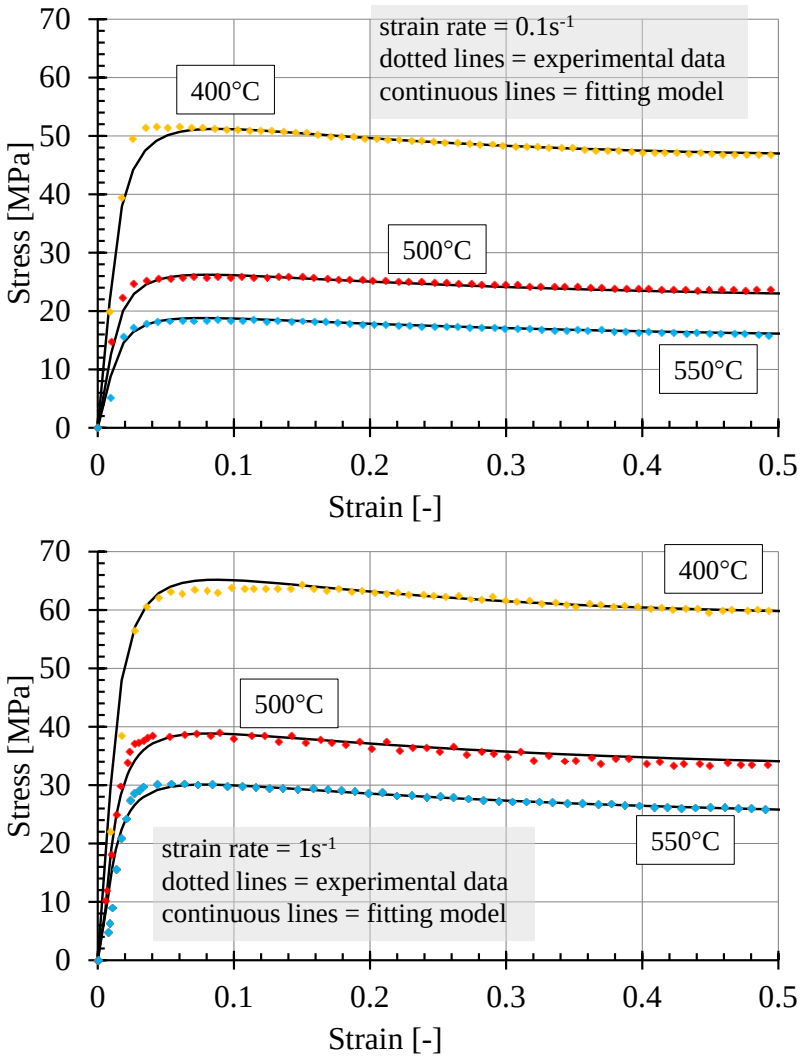

Figure 5. 4 – Experimental flow curves compared with Hansel-Spittel model fitting.

V.4 FORMABILITY CHARACTERIZATION AND MICRO-STRUCTURAL ANALYSIS

V.4.1 Tensile test apparatus and procedure

The tensile tests were also performed on the Gleeble 3800™ equipped with the tensile setup shown in Figure 5.5.

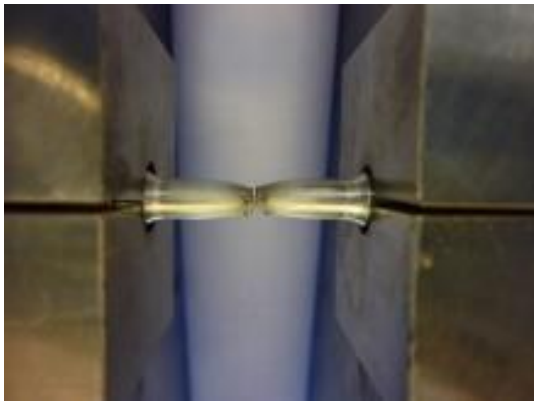

Figure 5. 5 - Gleeble 3800™ system in tensile configuration.

The tensile test specimen geometry is defined following technical guidelines [84, 85] and is presented in Figure 5.6.

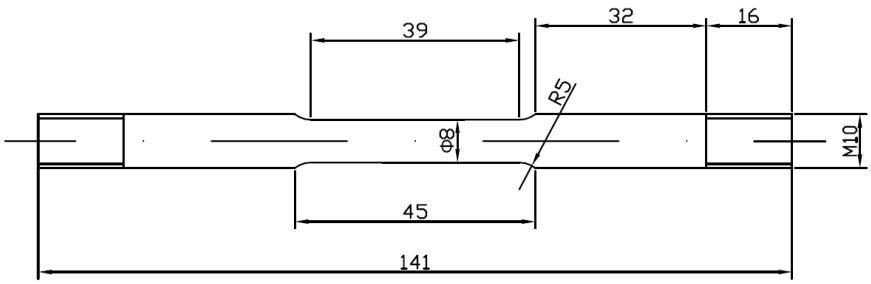

Figure 5. 6 – Hot tensile test specimen geometry.

Preliminary temperature measurements allowed identifying a *thermal gauge* length l_0 of 25 mm, in which the test temperature presented a maximum variation of 10°C. The specimen *diameter at fracture was chosen as the formability index*, which will also be used for the criterion calibration, since it is nether affected by thermal non-uniformities outside the specimen gauge length, nor by the elasticity of the machine jaws. Indeed these are all factor that would heavily affect other possible formability indexes such as the stroke at fracture.

The strain rate was calculated by means of the thermal gauge length with the following expression:

$$\dot{\varepsilon} = \frac{v}{l_0} \quad (5.3)$$

From which the constant punch displacement speed for the test was derived.

V.4.2 Tensile tests results

Tensile test campaign outcomes showed unexpected results both in terms of temperature and strain rate influence on formability:

- at the higher temperature, namely 550°C, the material formability was significantly reduced;
- a *negative strain rate influence* was highlighted at the two lower temperatures (400°C and 500°C), while the standard strain rate influence was evidenced at 550°C, entailing a *smoother thermally-induced formability drop or lower strain rates*.

The diameter at fracture was accurately measured by means of optical microscopy and the results are summarized in Table 5.3.

Temperature [°C]	Strain rate [1/s]	Diameter at fracture [mm]
400	0.1	3.79
400	1	3.60
500	0.1	3.40
500	1	2.84
550	0.1	5.06
550	1	5.62

Table 5. 3 – Fracture diameter values.

Average strain rate at fracture was derived using the expression in Equation (5.4). The resulting values are shown in Figure 5.7.

(5.4) $$\varepsilon_f = \ln\left(\frac{A_0}{A}\right) = 2\ln\left(\frac{D_0}{D}\right)$$

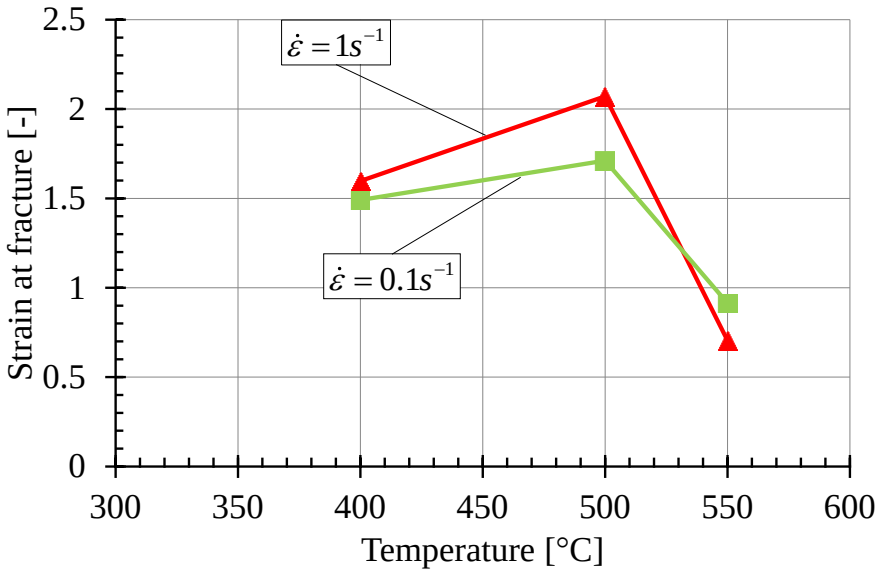

Figure 5. 7 – Strain at fracture as a function of temperature and strain rate.

V.4.3 Fractographic and Micro-chemical analysis

The microstructural reasons of the highlighted formability trend was first carried out by SEM fractographic analysis of the fracture surfaces. Figure 5.8 shows the resulting fracture features that can be discussed as follows:

- at higher strain rate (1.0 s^{-1}) the fracture mode is ductile at 400°C and 500°C, showing the typical dimpled surface. Passing to the higher test temperature, 550°C, the surface appears the one typical of hot intergranular fracture (it is evident the presence of refining grains);
- at lower strain rate ($0.1s^{-1}$) the fracture surfaces present a gradual passage from ductile characteristics, at 400°C, to intergranular fracture, at 550°C: indeed the fracture surface at 500°C shows intermediate characteristics.

These results are consistent with the sharp formability drop highlighted by the material at strain rate equal $1s^{-1}$ and also with the smoother trend at strain rate equal $0.1s^{-1}$.

To provide a further confirm and also a deeper physical insight on the fracture phenomenon, SEM EDS micro-chemical analysis war carried out on the same specimens, the results of which are highlighted in Figure 5.9, in which the Mg distribution in the Al matrix is shown.

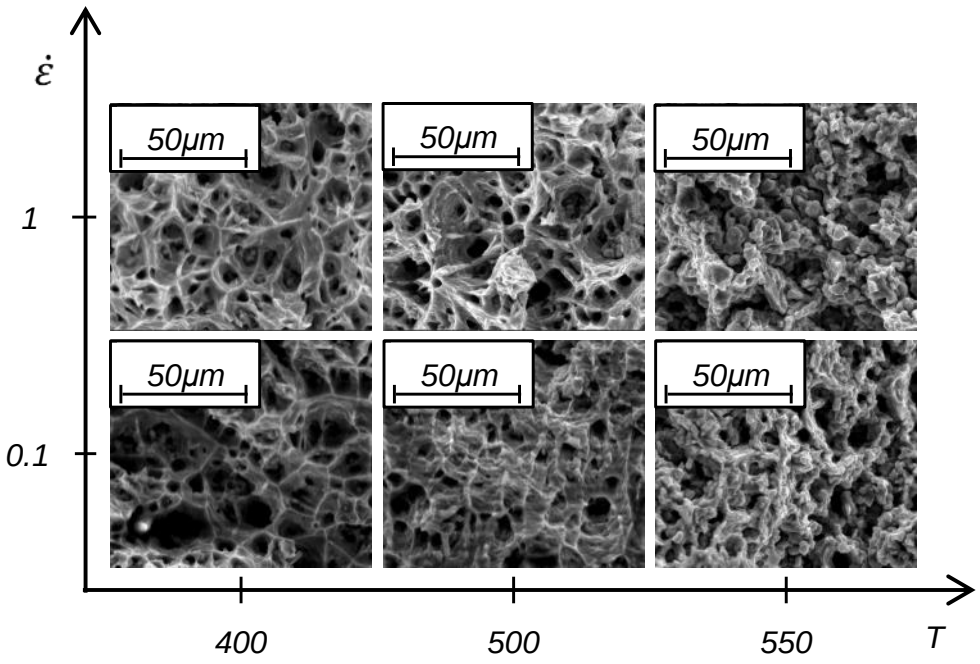

Figure 5. 8 – SEM fractographic analysis on tensile test specimens.

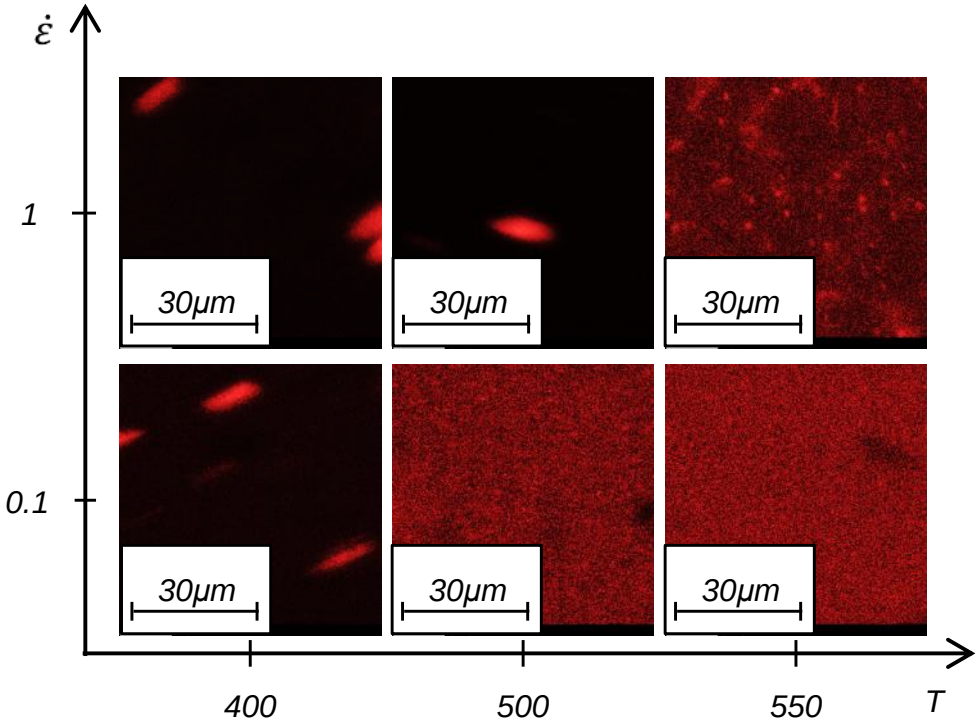

Figure 5. 9 – EDS Micro-chemical analysis on tensile test specimens, Mg distribution.

The results can be commented as follows:

- at higher strain rate (1.0 s^{-1}) and at 400°C and 500°C, the Mg is unevenly distributed as it is concentrated in some zones which can be interpreted as the Mg_2Si hardening intermetallic precipitates. At the higher test temperature, on the contrary, Mg results to be almost uniformly distributed;
- at lower strain rate ($0.1s^{-1}$) the intermetallic precipitates are highlighted only at the lower 400°C temperature, while a perfectly uniform distribution results at 500°C and 550°C.

The results confirm then the fractographic analysis, showing that the hot shortness onset is related to the hardening intermetallic precipitates diffusion in the Al matrix. An important conclusion is also that this diffusion is not only thermally-induced, but also *strain-induced* since:

- it was highlighted at lower temperature for lower strain rate;
- this fact can be explained by the *longer time that the specimen spends deforming at the set temperature*.

V.5 EXTENDED TENSILE TEST CAMPAIGN

A wider experimental tensile test campaign was then defined in order to have more data for the material formability modelling, namely to *identify the material fracture locus*. The following considerations were done:

- to confirm the strain rate influence on the diffusion mechanism, a lower tested strain rate was added;
- to provide better modelling as a function of temperature, a higher number of tested temperatures was provided, with a finer resolution in the hot shortness onset zone.

Table 5. 4 summarizes the new experimental plan.

Test variable	**Tested values**
Temperature [°C]	350, 400, 450, 500, 525, 550
Strain rate [1/s]	0.01, 0.1, 1

Table 5. 4 – Fracture locus calibration tensile test campaign.

Experimental results are shown in – Figure 5.10, which confirm the already highlighted temperature and strain influence.

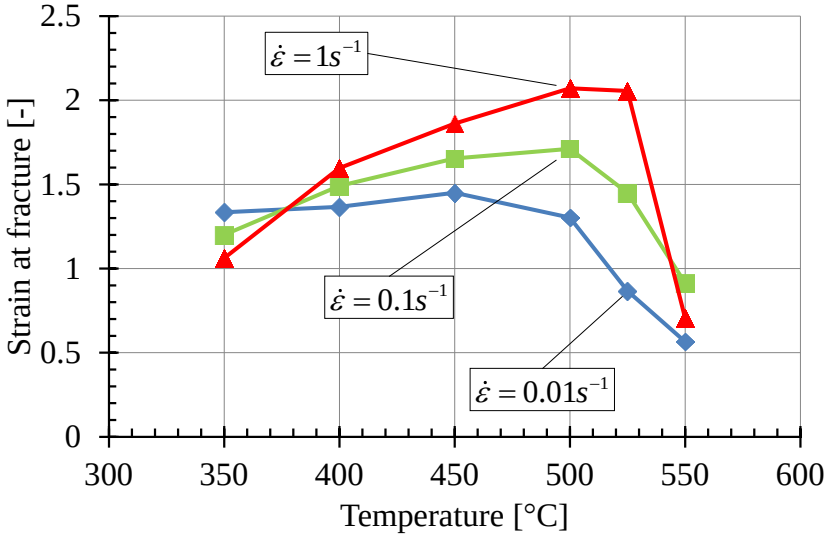

Figure 5. 10 – Strain at fracture and

Tensile test flow curves were derived from the force-displacement experimental data, using the following expressions:

$$\varepsilon = \ln\left(\frac{l}{l_0}\right) = \ln\left(\frac{l_0 + diplacement}{l_0}\right) \tag{5.5}$$

$$\sigma = \frac{F}{A} = \frac{F}{A_0 e^{-\varepsilon}} \tag{5.6}$$

This elaboration is done in order to obtain the material *peak stress* σ_P as a function of temperature and strain rate. The values of this parameter are plotted in Figure 5.11, while the stress-strain curves are reported in Figure 5.12. It can be seen that the material presents the classical temperature and strain rate dependence:

- temperature softening;
- strain rate hardening.

Which is also consistent with the compression tests results. Peak stress values are reported in Table 5. 5.

It is worth to underline the fact that there is no necessary link between peak stress and strain at fracture dependence on temperature and strain rate. Indeed the former one has the expected trend showed in Figure 5.11, while the latter has the particular non-linear behaviour displayed in Figure 5.10. This is essentially related with the fact that the peak

stress is primarily linked with the rheological characteristics of the material and not with its formability ones, since it is observed in the first part of the curve, in which neither strain localization, nor void growth have supposedly reached a relevant value. These two are, as a matter of fact, the driving factors of mechanical failure and then formability.

Peak stress [MPa]	**0.01s^{-1}**	**0.1s^{-1}**	**1s^{-1}**
350°C	54.1	77.4	99.7
400°C	36.8	47.9	58.7
450°C	27.5	33.2	41.4
500°C	21.7	25.5	34.2
525°C	17.8	21.7	29.2
550°C	15.7	18.7	23.6

Table 5. 5 – Peak stress values.

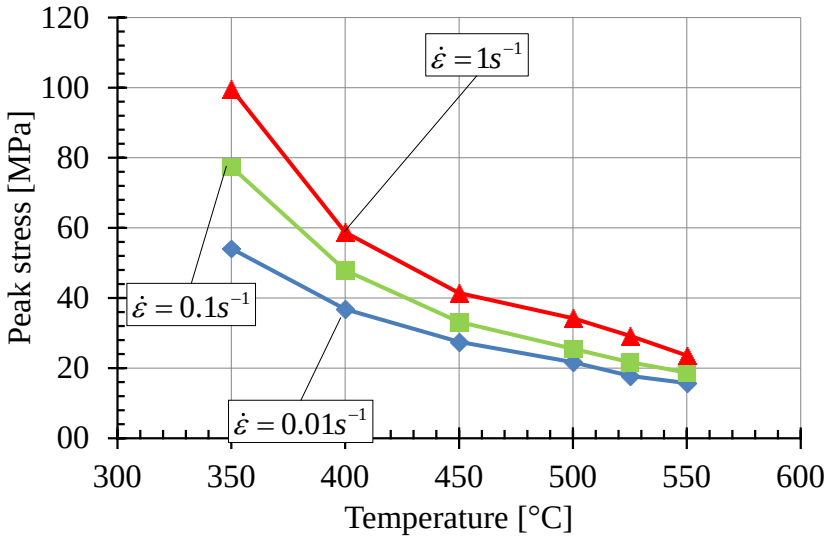

Figure 5. 11 – Peak stress in extended tensile test campaign.

Indeed this is also the reason why, from the formability numerical modelling point of view, the area reduction at fracture is a better index than elongation at fracture is. The former, indeed, is directly linked with the maximum strain at fracture the material can bear, while the latter is heavily affected by two other factors:

- the amount of uniform deformation that the material can undergo before plastic instability, which is strictly linked with the material strain hardening capability;

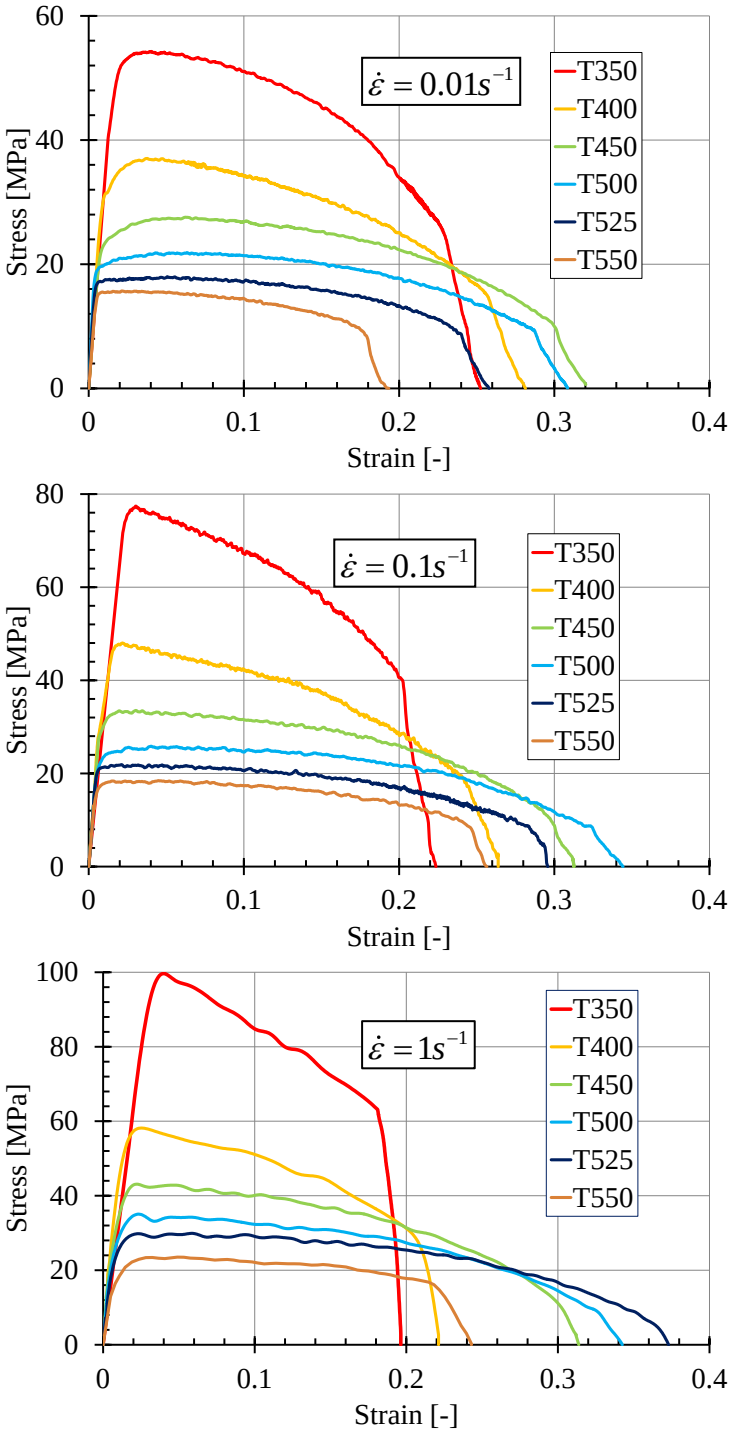

Figure 5. 12 – Stress-strain curves for extended tensile test campaign.

- the capability of the material, once plastic instability onsets, to provide a diffuse necking, which is in turn strictly dependent on the material strain rate sensitivity.

Both the just mentioned material characteristics are due to its rheological behaviour.

As a last note, this fact can also be noticed by the comparison of the strain at fracture value if calculated using Equation (5.4) or Equation (5.5). The benchmark of these is reported in Table 5. 6. From this table it can be seen that, even if the two formability measurements have somehow similar trends, there are anyway significant discrepancies, for example strain rate effect at 525°C is much more marked on area reduction than on elongation. It can also be noticed that negative strain rate effect on elongation is less evident and appears at higher temperatures, namely 500°C, than it does with are reduction (400°C). All these differences can be explained with the rheology effect on elongation.

Test conditions	**Elongation [-]**	**Reduction area [-]**
350°C, $0.01s^{-1}$	0.26	1.33
400°C, $0.01s^{-1}$	0.28	1.37
450°C, $0.01s^{-1}$	0.32	1.45
500°C, $0.01s^{-1}$	0.31	1.30
525°C, $0.01s^{-1}$	0.26	0.87
550°C, $0.01s^{-1}$	0.19	0.57
350°C, $0.1s^{-1}$	0.22	1.20
400°C, $0.1s^{-1}$	0.26	1.49
450°C, $0.1s^{-1}$	0.31	1.65
500°C, $0.1s^{-1}$	0.34	1.71
525°C, $0.1s^{-1}$	0.29	1.45
550°C, $0.1s^{-1}$	0.26	0.91
350°C, $1s^{-1}$	0.20	1.06
400°C, $1s^{-1}$	0.22	1.60
450°C, $1s^{-1}$	0.31	1.86
500°C, $1s^{-1}$	0.34	2.07
525°C, $1s^{-1}$	0.37	2.05
550°C, $1s^{-1}$	0.24	0.71

Table 5. 6 – Benchmark between elongation and area reduction.

VI CHAPTER

FRACTURE CRITERION FORMULATION AND CALIBRATION

VI.1 INTRODUCTION

In this chapter, which can be regarded as the core of this work, the numerical and experimental results obtained in Chapter 4 and 5 are put together and critically assessed to reach the formulation of the new damage law that is finally calibrated and translated into a routine to be implemented in the FE code.

The first paragraph is devoted to the assessment of the numerical and experimental data in order to provide a list of requirements that the new fracture criterion should meet. Some considerations are also exposed on the lacks that actually available models would present in this application.

In the second paragraph the particular issue of the effective strain rate estimation during the experimental tensile tests is identified as an important calibration source of error and an inverse FE analysis approach is proposed for its solution.

In the third paragraph a physically-based fracture criterion is proposed in order to satisfy all the requirements pointed out and also to overcome the lacks that are shown by the currently available models.

The fourth paragraph, finally, describes the calibration of the proposed criterion as well as that of an alternative and more empirical strategy to model the material formability, that will be used as further benchmark case for validation. Both formulations are implemented in the FE code by a dedicated routine.

VI.2 NUMERICAL AND EXPERIMENTAL OUTCOMES DISCUSSION AND ASSESSMENT

VI.2.1 Stress state

The stress state evolution at the bar axis (which is the crack onset zone) was found to have remarkable characteristics, already described in Chapter IV:

an almost constant value of the deviatoric parameter that is also equal to -1, which implies the stress state axi-symmetry;

medium values of stress triaxiality, in the 0.15÷0.35 range.

These features imply the fact that the material damage evolution is negligibly influenced by the stress deviator, but, on the other hand, fracture criteria developed for high triaxiality ranges probably are not the more suitable to be applied in this case.

VI.2.2 Temperature and Zener-Hollomon parameter dependence

Interesting conclusions can be drawn analysing the strain at fracture trend as a function of the Zener-Hollomon parameter. The activation energy Q, needed for Z calculation, can be derived by the peak stress values applied to the Arrhenius flow rule expressed in Equation (2.49):

$$N = \left.\frac{\partial \ln(\dot{\varepsilon})}{\partial \ln(\sigma_P)}\right|_{T=\text{const.}} \tag{6.1}$$

$$Q = RN \left.\frac{\partial \ln(\sigma_P)}{\partial\left(\frac{1}{T}\right)}\right|_{\dot{\varepsilon}=\text{const}} \tag{6.2}$$

Figure 6.1 presents the linear regression for the derivation of N. An average value of 9.81 was obtained. This value is then used for the linear regression illustrated in Figure 6.2, needed to obtain the value of the activation energy Q. An average value of 275300 J/mol is calculated. This allows then calculating the Zener-Hollomon parameter value for any tested condition.

The strain at fracture values as a function of Z can then be found and are displayed in Figure 6.3. It can be clearly seen that a linear trend cannot be identified for all the experimental points, but it can be for the ones which are clearly related with ductile fracture mode. Indeed in the chart three points families are highlighted with different colours:

- *black marker*; that corresponds to a thermo-mechanical regime that can clearly be related to ductile fracture. These points are those which are at lower temperature than the maximum formability highlighted (for each strain rate);

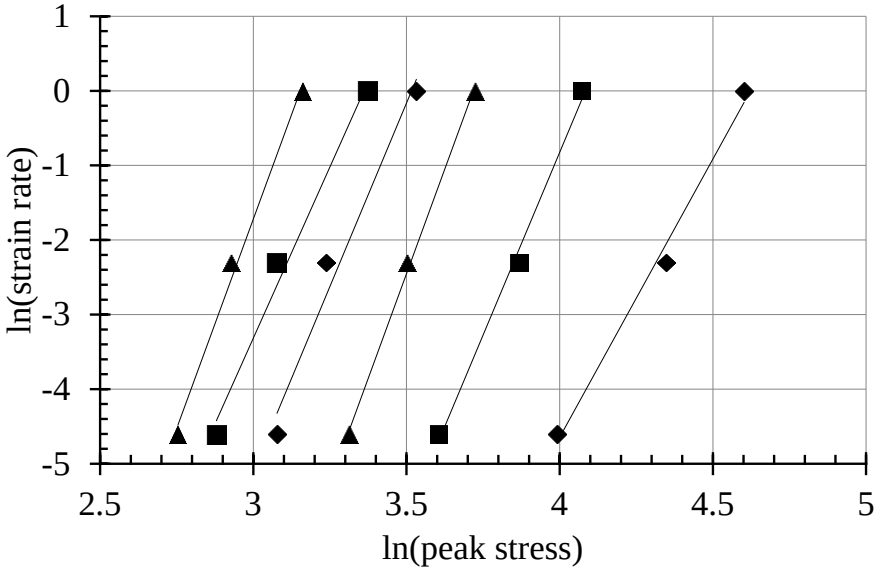

Figure 6. 1 – Linear regression for N parameter derivation.

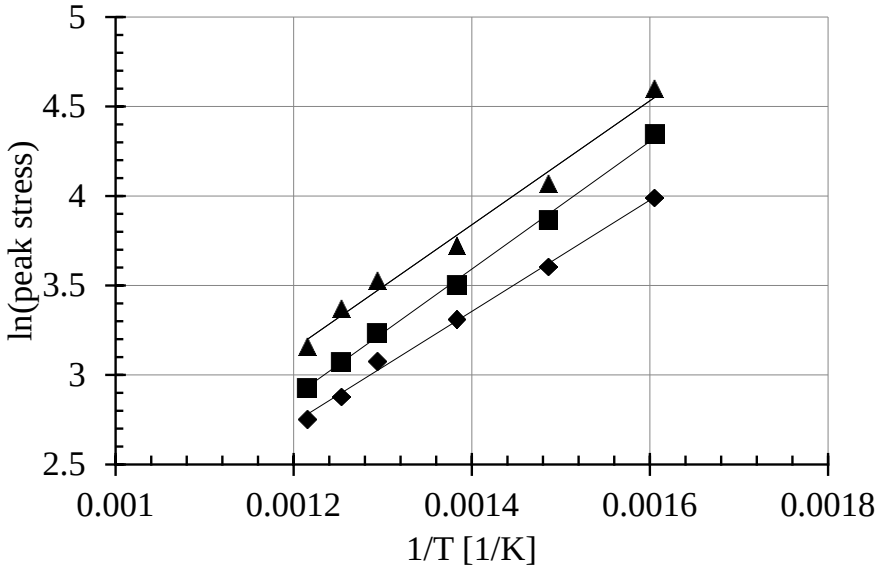

Figure 6. 2 – Linear regression for Q derivation.

- *red marker*; these are the experimental point which are closest to the maximum formability highlighted. It is assumed that this is the limit condition for fracture mode change trigger;

- *blue marker*; these are the post-maximum formability point, in the *hot shortness zone*. They are clearly the ones that offset from the linear trend.

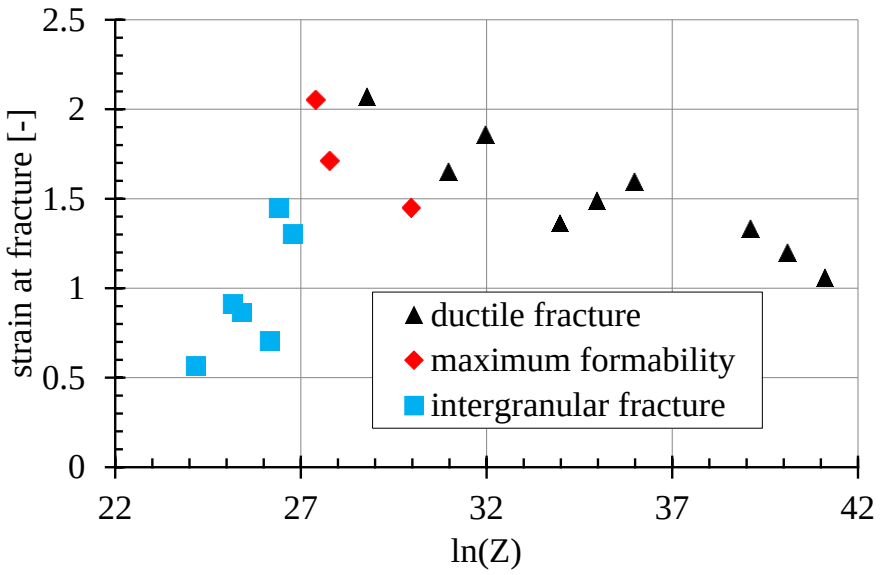

Figure 6. 3 – Strain at fracture as a function of Zener-Hollomon parameter.

These considerations are consistent with what was observed by Alexandrov et al. [29] and in general confirm the fact that fracture mode changes are linked with non-linear formability dependence on Z, as was found, for example, also by Chang et al. [28] for creep-regime fracture.

The new fracture criterion formulation, thus, should avoid complicate empirical expressions of the strain at fracture dependency on Z, since this would not provide meaningful physical insight on the fracture mode change-induced hot shortness.

One last significant remark can be done on the hot shortness modelling: the only available criterion that takes it into explicit account is that developed by He et al. [69], already described in Equation (2.48). This exponential expression is intrinsically capable of representing only slow formability drops, such as that illustrated by He in his already mentioned work (see Figure 2.30). In general the shape of the function is that of Figure 6.4**Errore. L'origine riferimento non è stata trovata.**, while in this case the formability drop is pretty sharp, especially at the highest strain rate.

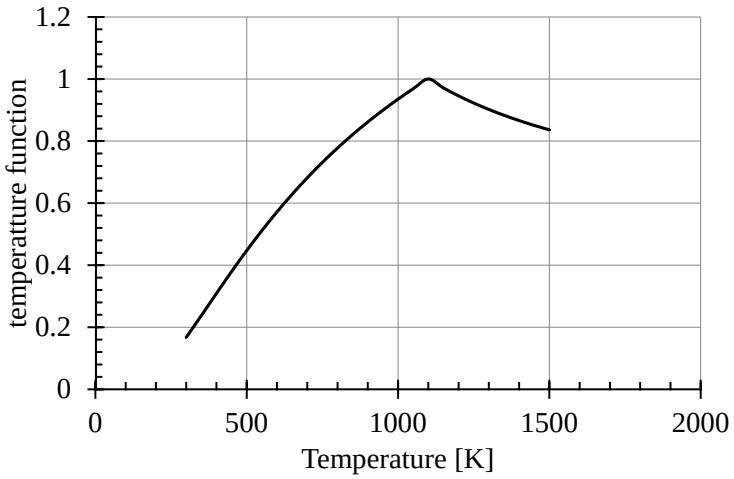

Figure 6. 4 – He function qualitative shape.

VI.2.3 Strain rate sensitivity

The formability characteristics summarized in Figure 5.11 present two relevant aspects:

- hot shortness temperature is not constant, as for example shown in the work of He el al. [69], but increases with increasing strain rate;
- strain rate dependence is negative for most of the tested conditions; this is true for all the tested conditions excluding the lower temperature 350°C, at which the standard positive strain rate dependence is displayed, and the higher temperature 550°C, at which the formability is highly deteriorated and a clear correlation cannot be established.

These two evidences have been correlated with the microstructural analysis carried out in the previous chapter. Experimental evidence shows that at lower strain rate the intermetallic precipitates are dissolved in the aluminium matrix at lower temperature. This also affects accordingly the strain at fracture and the fracture surface morphology.

Low melting second phase formation is widely recognized [7] to be one of the main reasons that induce hot shortness. However also intermetallic precipitates diffusion in the metal matrix can affect its formability. An example of this can be found in [86], from which Figure 6.5 is taken: Mg_2Si solubility equilibrium temperature is displayed as a function of concentration.

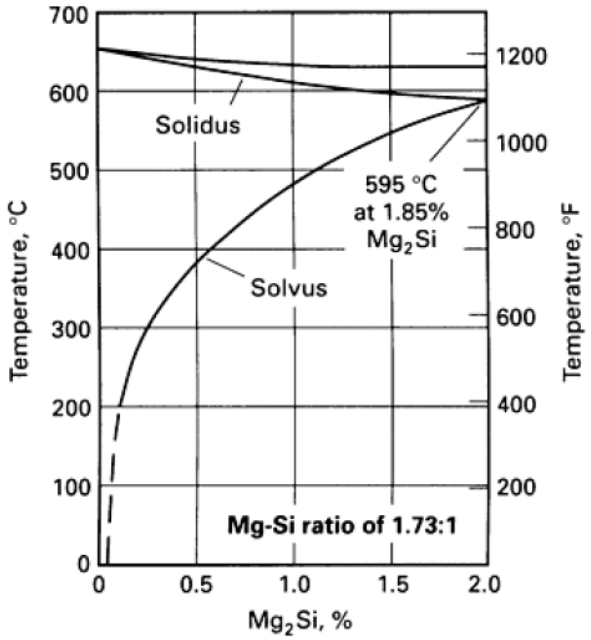

Figure 6. 5 - Equilibrium solubility of Mg_2Si in aluminium as function of temperature and concentration [86].

Zhang et al. [87] published a study in which the pseudo-binary Al-Mg_2Si diagram is investigated and a ternary phase field Al+Mg_2Si+liquid is found at 583.5°C, as shown in Figure 6.6.

In the light of these facts, then, the formability negative strain rate sensitivity can be explained in the following way: *the thermally-induced diffusion of Mg_2Si precipitates in the aluminium matrix, is also affected by a superimposed deformation process which accelerates the kinetics of the diffusion; however, fast deformations inhibit the diffusion to take place, while slow deformations favour the diffusion process*.

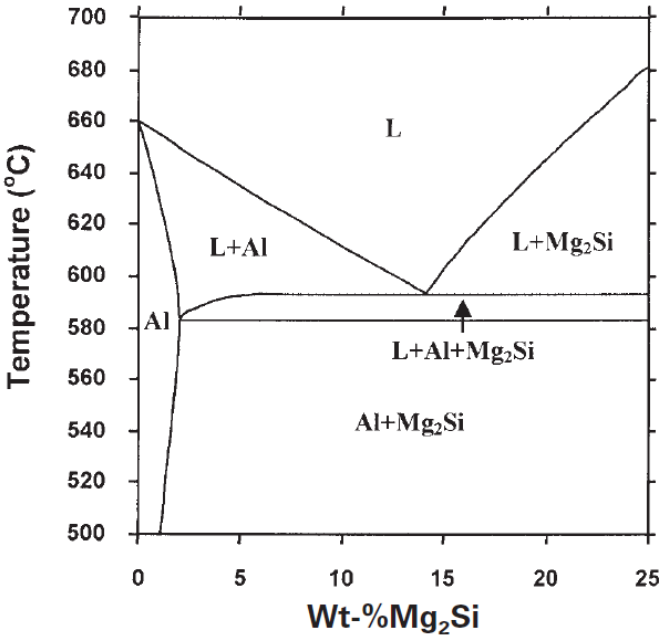

Figure 6. 6 - Pseudo-binary Al-Mg_2Si diagram [87].

The new fracture criterion formulation should then model all these aspects, and namely: negative strain rate sensitivity, strain rate-dependent hot shortness temperature and precipitates diffusion.

VI.3 AVERAGE STRAIN RATE CALCULATION

The key role played by the strain rate in the damage mechanism, suggests to provide a more accurate determination of its actual value during the tests. To this aim a FE model of the tensile tests used was implemented and run in order to investigate the actual strain rate evolution.

The outcomes showed that a significant strain rate increase takes place in the last deformation stages, due to strain localization. To take into account this fact, an *average strain rate* value was defined following the usual formulation for average values:

(6.3) $$\dot{\varepsilon}_{avg} = \int_0^{\varepsilon_f} \dot{\varepsilon} d\bar{\varepsilon}$$

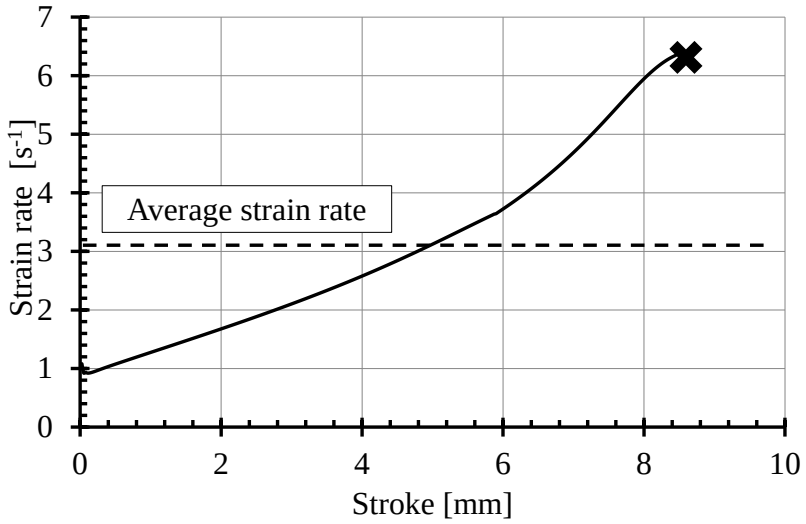

Figure 6. 7 – Strain rate evolution at the bar axis during the tensile test.

Figure 6.7 outlines an example of strain rate trend at the bar axis during a tensile test simulation. In the following analyses the nominal strain rates values will then be substituted by the average ones.

VI.4 FRACTURE CRITERION FORMULATION

The aim of this paragraph is to synthetize all the experimental evidences, analysis and considerations made up to this point to formulate a new damage criterion which can satisfy all the requirements highlighted:

(6.4) $$D = f\left(\sigma_{ij}, \varepsilon_{ij}, T, \dot{\varepsilon}_{ij}, material\ characteristics\right)$$

in which the material characteristics are assumed to be represented by the model coefficients that will be determined by the calibration, the first target is the to define the analytical shape that the function should have concerning the stress, strain, temperature and strain rate dependency.

A first and fundamental assumption consists in the *temperature damage dependence decomposition* that is to say that the damage criterion can be formulated in the following way:

(6.5) $$dD = f\left(\sigma_{ij}, \varepsilon_{ij}, T, \dot{\varepsilon}_{ij}\right) d\bar{\varepsilon} = a\left(\sigma_{ij}, \varepsilon_{ij}\right) b\left(T, \dot{\varepsilon}_{ij}\right) d\bar{\varepsilon}$$

in which the material dependence has not been mentioned.

This is, generally speaking, a widely used approach to modelling problems, since it allows significant mathematical simplifications without affecting much the model representation capabilities. For example Xue in [22] proposed such an approach to decompose stress triaxiality and deviatoric parameter contributions while He et al. [69] and Alexandrov et al. [29] decomposed the temperature dependency in a similar way.

Thus the temperature damage dependence decomposition appears to be the best approach, provided the clarification that such a decomposition does not entail a complete independence of the two factors, since the thermal conditions affect the stress and strain fields by means of the rheological model.

VI.4.1 Stress and strain state dependency – $a\left(\sigma_{ij},\varepsilon_{ij}\right)$ function

The stress state resulting by preliminary simulations imply that the stress deviator is almost constant during the damage evolution. Thus, even if its influence on damage can in general relevant, it can be neglected in this particular case, being incorporated as a constant coefficient in a deviatoric parameter-independent fracture criterion. This assumption leads to supposedly little approximation, being on the other hand of huge value, since deviatoric parameter-dependent fracture criteria need extensive experimental efforts to be calibrated.

Among the triaxiality-dependent fracture criteria the Oyane-Sato's appears to be the more suitable to be applied to this case, since it has been widely proved to be effective in the medium triaxiality range, which are those involved in the study case. Moreover it shows lower mesh size-sensitivity if compared with coupled criteria and its simple formulation allows also to avoid the use of FE numerical inverse analysis for calibration, letting room to focus on thermal factors modelling, which have been proven to be the main influence variables on the material formability.

The $a\left(\sigma_{ij},\varepsilon_{ij}\right)$ function can then be expressed as:

$$a\left(\sigma_{ij},\varepsilon_{ij}\right)=\left(1+A\eta\right) \tag{6.6}$$

VI.4.2 Temperature and strain rate dependency – $b\left(T,\dot{\varepsilon}_{ij}\right)$ function

The strategy used in this case consists in the improvement of the more advanced model currently available, which is the one developed by He et al. [69].

Since the aim of this work is to provide a model which is physically based and easy to calibrate and implement, some *simplifying assumptions* are made in order to limit the

model complexity and in particular to avoid brute-force empirical regressions on experimental data:

- the negative strain rate influence-temperature range will be the primary concern in the model formulation, since it is the more important phenomenon that affects material formability. The positive strain rate influence at 350°C is then a secondary concern;
- the Mg_2Si diffusion in the aluminium matrix is considered the only factor which causes the hot shortness and its full development is considered to nullify the material formability. Besides being a simplifying assumption, this is a safety assumption as well;
- the hot shortness temperature dependence on strain rate must be modelled in the simplest possible way.

These assumptions led to the formulation of the following expression of the strain at fracture:

$$\bar{\varepsilon}_f = f(T,\dot{\varepsilon}) = K\dot{\varepsilon}^a \left[\exp\left(-\left| \frac{1}{T_m - T} - \frac{1}{T_m - T_C} \right| \frac{Q}{R} \right) \right]^b \tag{6.7}$$

The more relevant model features are here discussed:

- the strain rate sensitivity factor a, will assume a positive value, entailing negative strain rate sensitivity;
- the hot shortness temperature T_C is not a constant value, but is expressed by a power law function of the strain rate:

$$T_C = E\dot{\varepsilon}^F \tag{6.8}$$

- the exponential form in Equation (6.6) allows to reproduce sharp formability drops, as highlighted qualitatively in Figure 6.8. Moreover it introduces another temperature constant, T_m, which is the temperature at which the expression equals zero. At the same time it also continue to have a maximum value if the temperature equals T_C, which was a characteristic of the He's formulation.

$$\exp\left(-\left|\frac{1}{T_m - T} - \frac{1}{T_m - T_C}\right|\right) \tag{6.9}$$

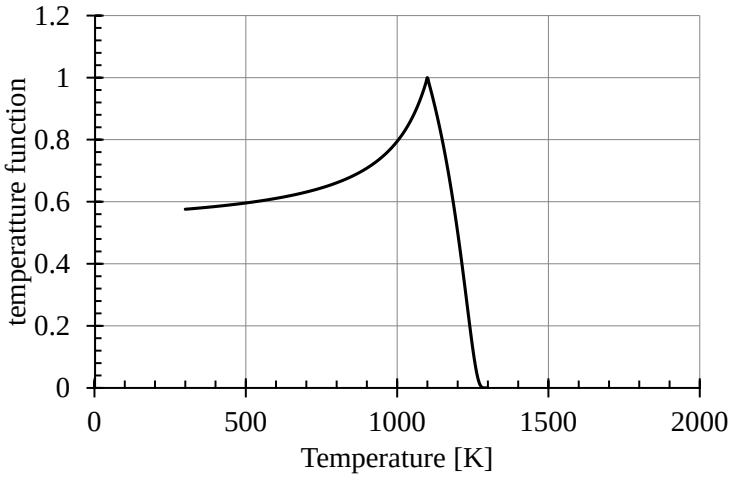

Figure 6. 8 – New model function qualitative shape.

The model described in Equation (6.4) allows then to set two *characteristic temperatures*: one at which the material shows the maximum formability, that is to say the *hot shortness temperature*, and another one, at which the material formability characteristics are so reduced that it can be assumed zero formability, which is, in the study case, the *equilibrium temperature for precipitates diffusion*.

To obtain the $b\left(T, \dot{\varepsilon}_{ij}\right)$ function the following procedure was followed:

$$D^*_{Oyane} = \int_o^{\bar{\varepsilon}_f} \left(1 + A\eta\right) d\bar{\varepsilon} = \bar{\varepsilon}_f + \int_o^{\bar{\varepsilon}_f} A\eta d\bar{\varepsilon} = \bar{\varepsilon}_f + A\tilde{\eta}\bar{\varepsilon}_f = \bar{\varepsilon}_f \left(1 + A\tilde{\eta}\right) \tag{6.10}$$

in which $\tilde{\eta}$ is the *triaxiality integral average value*.

Using the expression of the model $\bar{\varepsilon}_f = \bar{\varepsilon}_f \left(T, \dot{\varepsilon}\right)$ (Equation (6.5)), it is then possible to write the expression of the *fracture locus*:

(6.11) $$D^*_{Oyane} = \bar{\varepsilon}_f\left(T,\dot{\varepsilon}\right)\left(1+A\tilde{\eta}\right) = D^*_{Oyane}\left(T,\dot{\varepsilon}\right)$$

It is finally defined the function in this way:

(6.12) $$b\left(T,\dot{\varepsilon}\right) = \frac{1}{D^*_{Oyane}\left(T,\dot{\varepsilon}\right)}$$

VI.4.3 Overall model expression

The definition of Equation (6.10) leads to the following overall expression:

(6.13) $$dD = a\left(\sigma_{ij},\varepsilon_{ij}\right)b\left(T,\dot{\varepsilon}\right)d\bar{\varepsilon} = \frac{\left(1+A\eta\right)}{D^*_{Oyane}\left(T,\dot{\varepsilon}\right)}d\bar{\varepsilon}$$

which, integrated, leads to:

(6.14) $$D = \int_0^{\bar{\varepsilon}} \frac{\left(1+A\eta\right)}{D^*_{Oyane}\left(T,\dot{\varepsilon}\right)}d\bar{\varepsilon} = \int_0^{\bar{\varepsilon}} \frac{\left(1+A\eta\right)}{\bar{\varepsilon}_f\left(T,\dot{\varepsilon}\right)\left(1+A\tilde{\eta}\right)}d\bar{\varepsilon}$$

Which is the final expression of the damage value in the proposed approach. It can be noticed that the definition of Equation (6.10), though arbitrary, leads to a very important consequence, which is *damage normalization*:

(6.15) $$D = \int_0^{\bar{\varepsilon}_f} \frac{\left(1+A\eta\right)}{D^*_{Oyane}\left(T,\dot{\varepsilon}\right)}d\bar{\varepsilon} = \frac{1}{D^*_{Oyane}\left(T,\dot{\varepsilon}\right)}\int_0^{\bar{\varepsilon}_f}\left(1+A\eta\right)d\bar{\varepsilon} =$$

$$= \frac{1}{D^*_{Oyane}\left(T,\dot{\varepsilon}\right)}D^*_{Oyane}\left(T,\dot{\varepsilon}\right) \equiv 1$$

VI.5 FRACTURE CRITERION CALIBRATION

In this last paragraph the calibration of the proposed approach is presented first. Then an empirical calibration by means of bi-linear regression on the experimental data is proposed. At last the expressly developed routine for both criteria implementation is briefly schematized.

VI.5.1 Calibration of the criterion

To be calibrated the criterion needs seven constants and a function to be identified:

- the constants are: K, a, Q, b, T_m, A and $\tilde{\eta}$;
- the function is $T_C = \mathrm{E}\,\dot{\varepsilon}^F$.

However some of them have already been defined or are physical constants, namely:

- an average $Q = 275300 J/mol$ has been calculated or can be taken from literature;
- the value $T_m = 856.5K$ can be taken from literature [76] or handbooks;
- it can be assumed from literature [16, 41, 42] that $A = 3$;
- and finally an average value of $\tilde{\eta} \approx 0.333$ can be set from uni-axial stress state assumption (which is in favour of safety), or derived by mean values from FE analysis.

The parameter a can be derived using the definition of Equation (6.5), from which:

$$a = \frac{\partial \ln(\bar{\varepsilon}_f)}{\partial \ln(\dot{\varepsilon})} \tag{6.16}$$

however, due to the material formability non-linear behaviour, very different values result and only an average value can be set. As stated, expressing a as function of the temperature would be more precise, but also would make the model lose simplicity. The approximation taken is then to discard the values for 350°C and 550°C and obtain an average value of a for the remaining curves. In Figure 6.9 are shown the resulting regression lines. It can also be noticed that the strain rate sensitivity grows with increasing temperature. A value of $a = 0.094$ is found.

The three values of T_C can be found interpolating the experimental data with a polynomial curve and finding its maximum. In Table 6. 1 - Hot shortness temperature values.Table 6. 1 the resulting values are shown.

Strain rate [1/s]	**T_C [K]**
0.031	721
0.33	762
3.1	777

Table 6. 1 - Hot shortness temperature values.

These results are then fitted with a power law expression. See Figure 6. 10 for the fitting values.

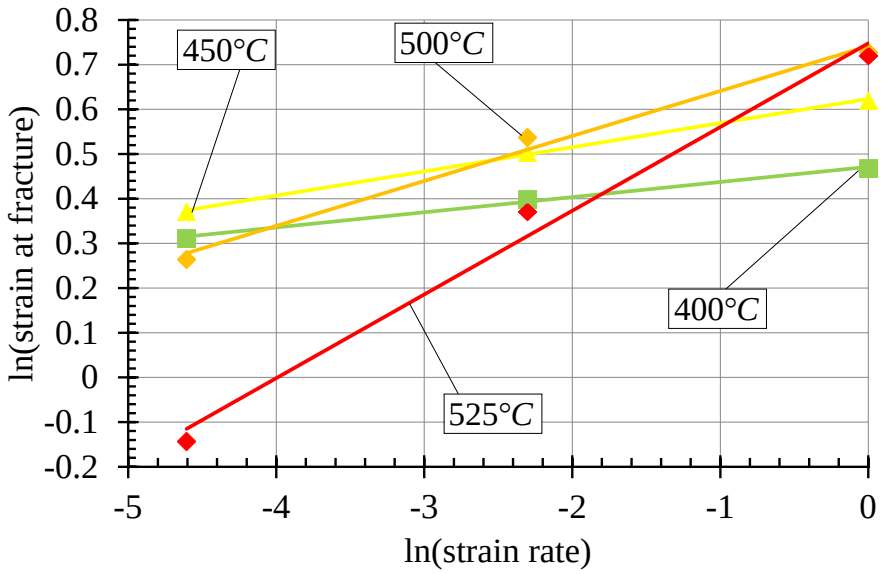

Figure 6. 9 – Regression for a calculation.

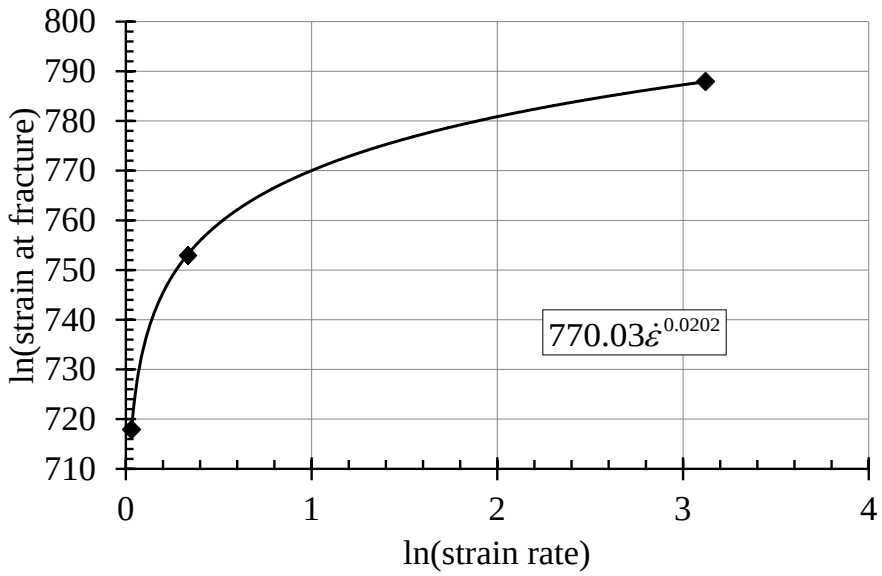

Figure 6. 10 – Regression for critical temperature expression.

The parameter K is multiplying factor and thus it can be found simply by matching one experimental point with one of the model. Making it for $T = 450°C$ and $\dot{\varepsilon} = 0.1s^{-1}$ a value of $K = 1.95$ is found.

The last parameter, b, must be found by optimizing the fracture locus fit. A value of $b = 0.001$ is found in this case.

This calibration leads to the following expression of the function:

$$\bar{\varepsilon}_f = 1.95\dot{\varepsilon}^{0.094}\left[\exp\left(-\left|\frac{1}{856.5-T}-\frac{1}{856.5-770\dot{\varepsilon}^{0.0202}}\right|\frac{275300}{8.13}\right)\right]^{0.001} \quad (6.17)$$

Errore. L'origine riferimento non è stata trovata. Figure 6.11 shows the model prediction capability comparing it with the results of the experiments. The fitting is quite good everywhere but in the two extreme temperatures. This was expected and is related to the definition of a as a constant.

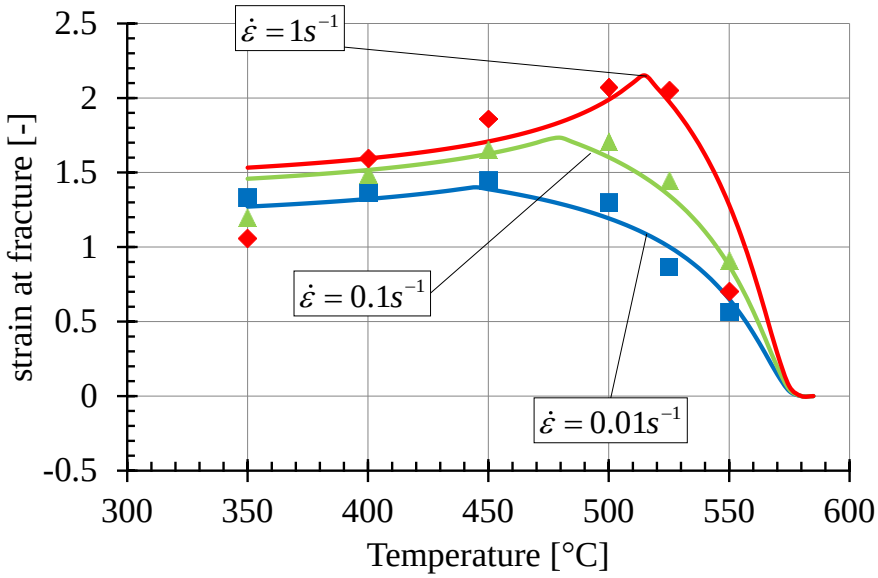

Figure 6. 11 – Strain at fracture prediction of the model, compared to experiments.

Finally, then, assuming that $A = 3$ and that $\tilde{\eta} = 0.333$ the fracture locus expression can be derived. It is worth to underline that a more precise estimation of $\tilde{\eta}$ could be done by FE inverse analysis, however:

- the purpose of this work is to develop a model very easy to calibrate and inverse analysis should be avoided to this aim;

- moreover assuming $\tilde{\eta} = 0.333$ is an approximation which tends to overestimate the damage that the material undergoes during deformation, thus it is in favour of safety.

Substituting in Equation (6.10), the term $\left(1 + A\tilde{\eta}\right)$ equals 2 and the fracture locus expression becomes:

$$D^*_{Oyane}\left(T,\dot{\varepsilon}\right) = \bar{\varepsilon}_f\left(T,\dot{\varepsilon}\right)\left(1 + A\tilde{\eta}\right) = \tag{6.18}$$

$$= 3.9\dot{\varepsilon}^{0.094}\left[\exp\left(-\left|\frac{1}{856.5 - T} - \frac{1}{856.5 - 770\dot{\varepsilon}^{0.0202}}\right|\frac{275300}{8.13}\right)\right]^{0.001}$$

Figure 6.12 shows the fracture locus shape.

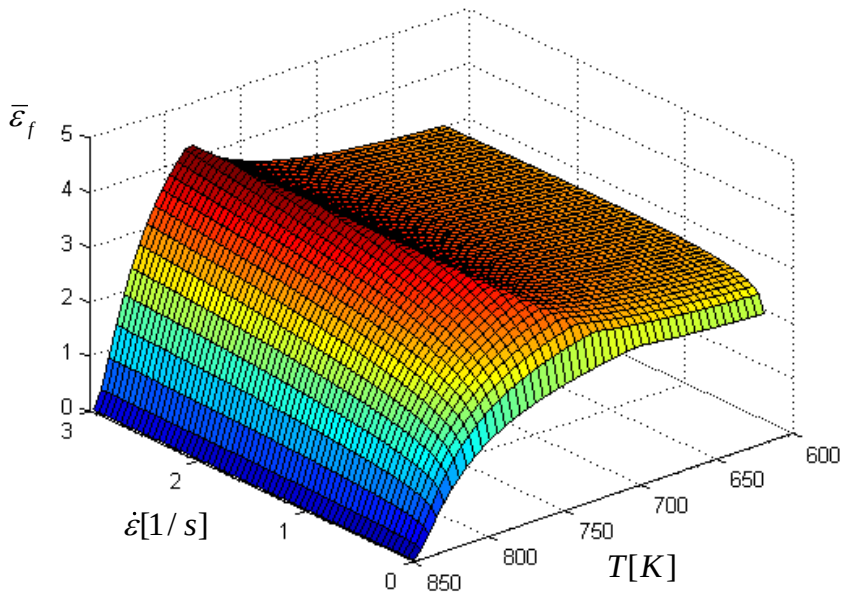

Figure 6. 12 – Analytical fracture locus surface.

VI.5.2 Empirical calibration

An alternative way to provide the fracture locus calibration consists in an empirical approach that makes also use of inverse FE analysis. The procedure is the following:

- for each experimental condition a FE simulation of the tensile test is run and the Oyane-Sato critical damage is determined by using the diameter at fracture as calibrating parameter;

- these are the experimental points of the fracture locus $D^*_{Oyane}\left(T_{test}, \dot{\varepsilon}_{test}\right)$;
- a bilinear interpolation is used in order to find the fracture locus surface $D^*_{Oyane}\left(T, \dot{\varepsilon}\right)$.

The experimental $D^*_{Oyane}\left(T_{test}, \dot{\varepsilon}_{test}\right)$ values as derived by the inverse FE analysis are shown in Table 6. 2. It must be underlined that the strain rate values are the average ones obtained with the procedure described in Paragraph 6.3.

Strain rate [1/s]	**T [K]**	**D^*_{Oyane}**
0.045	623	3.72
0.037	673	3.47
0.032	723	3.63
0.026	773	2.96
0.025	798	1.94
0.024	823	1.22
0.433	623	3.33
0.345	673	3.85
0.357	723	3.95
0.319	773	3.83
0.296	798	3.20
0.257	823	1.97
4.124	623	3.02
3.800	673	4.14
3.190	723	4.36
2.750	773	4.79
2.770	798	4.43
2.120	823	1.47

Table 6. 2 – Empirical Oyane-Sato critical damage.

The bi-linear interpolation strategy is outlined in Figure 6.13, while the resulting fracture locus is displayed in Figure 6.14.

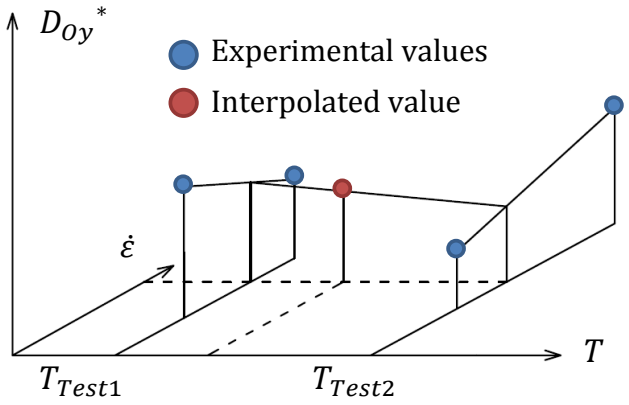

Figure 6. 13 – Bilinear interpolation scheme.

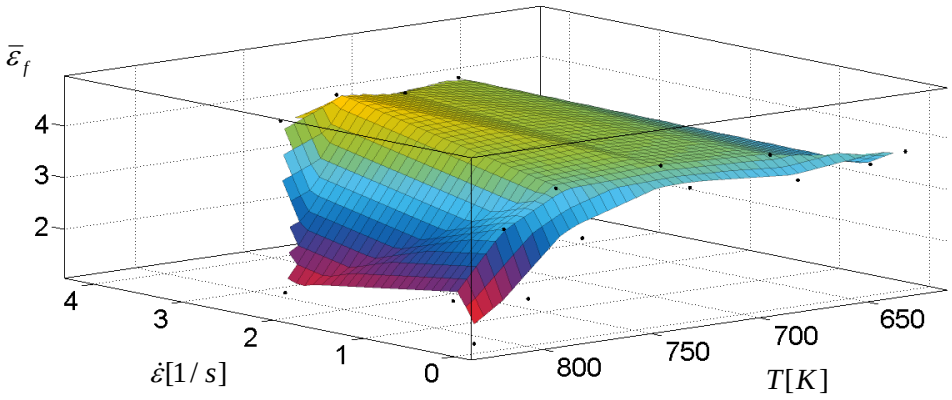

Figure 6. 14 – Empirical fracture locus surface.

VI.5.3 FE code implementation

The two damage models just described were implemented with a dedicated Fortran subroutine in the Forge 2011™ software. The standard Oyane-Sato criterion was modified in its formulation introducing the $b(T,\dot{\varepsilon})$ function, which is set, by definition of Equation (6.12), *equal the inverse value of the fracture locus* $D^*_{Oyane}(T,\dot{\varepsilon})$. The damage critical value is finally set equal to 1, as seen in Equation (6.15).

A schematic illustration of the subroutine introduced is represented in Figure 6.15.

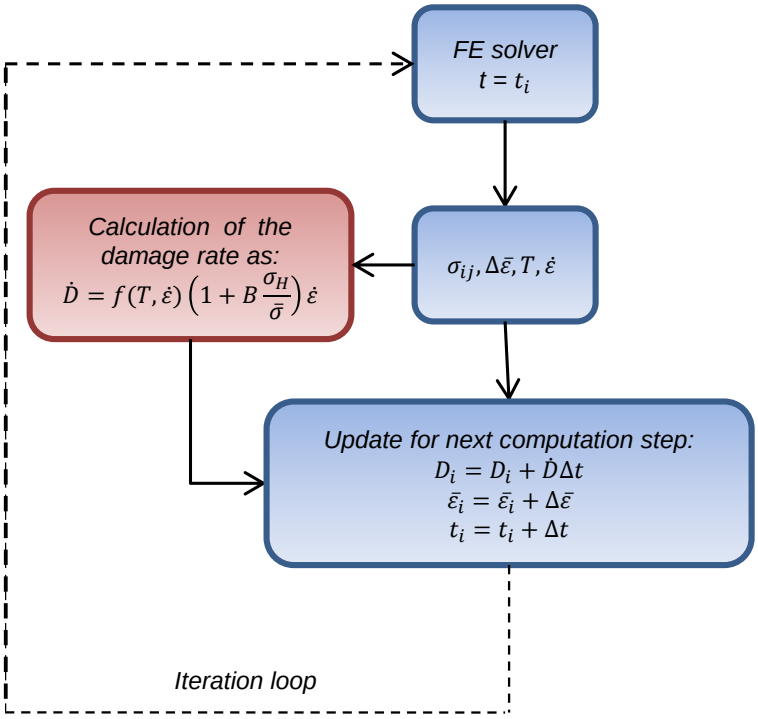

Figure 6. 15 – Scheme of the new fracture criterion routine implementation

VII CHAPTER

FRACTURE CRITERION VALIDATION AND APPLICATION

VII.1 INTRODUCTION

This chapter concerns the application of the previously developed and calibrated fracture criterion to the industrial case study described and modelled in Chapter 4.

In the first paragraph the criterion will be *validated* making a benchmark of its predictive capabilities with two references:

- the outcomes of the industrial trials, which properly provides the model experimental validation;
- the outcomes of the empirically calibrated model; which can be regarded as a reference numerical simulation since its calibration procedure allows to have a best fitting on the experimental data, though having all the practical and theoretical limits described in Chapter 6. In this sense this benchmark allows to quantify what is the error that the simplifying assumptions of the model imply.

In the second paragraph, on the other hand, a possible *application* of the calibrated criterion which aims both to *process optimization* and to *intelligent process re-design* is shown. The application consists in the systematic use of the numerical model in order to transform the *material formability window*, as it results from the experimental campaign, into a *process formability window*, which has then process variables as inputs.

VII.2 VALIDATION

The results of two industrial trials were available for the validation. The process parameters values set in the two cases are summarized in Table 7. 1 together with the trial outcomes.

The simulation numerical model as described in Chapter IV was then run with these two sets of process parameters and with implemented the routine developed in Chapter VII. **Errore. L'origine riferimento non è stata trovata.**Figure 7.1 shows the simulations results on an axial longitudinal section.

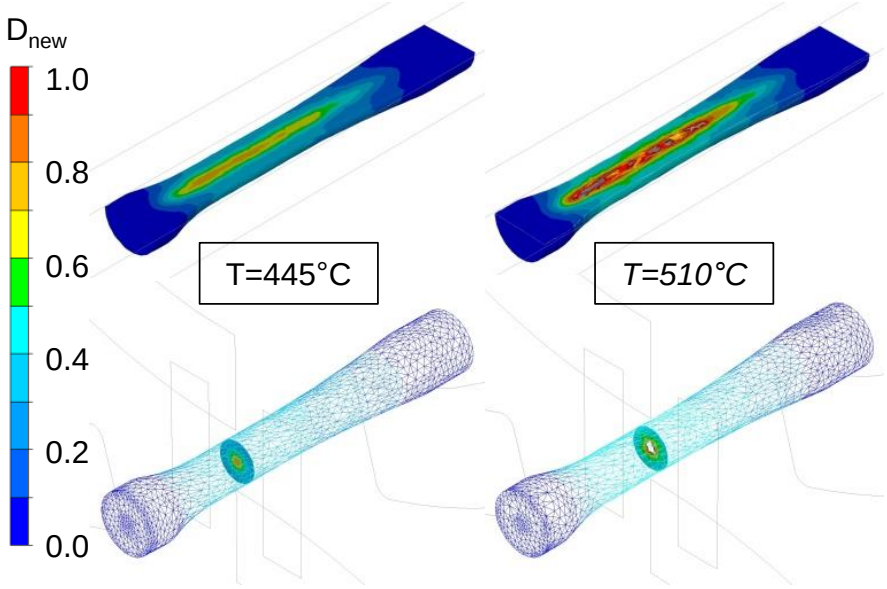

Figure 7. 1 – Validation results, crack prediction in the bar longitudinal section.

Trial identification	**Trial A**	**Trial B**
Furnace temperature [°C]	445	510
Rolls rotation speed [rpm]	3	3
Reported outcome	uncracked	cracked

Table 7. 1 – Validation reference cases.

It is clear that the model has good predictive capability of the crack onset as also shown by the bar cross sections illustrated in Figure 7.2, in which a fractografy of the axial fracture surface is also provided.

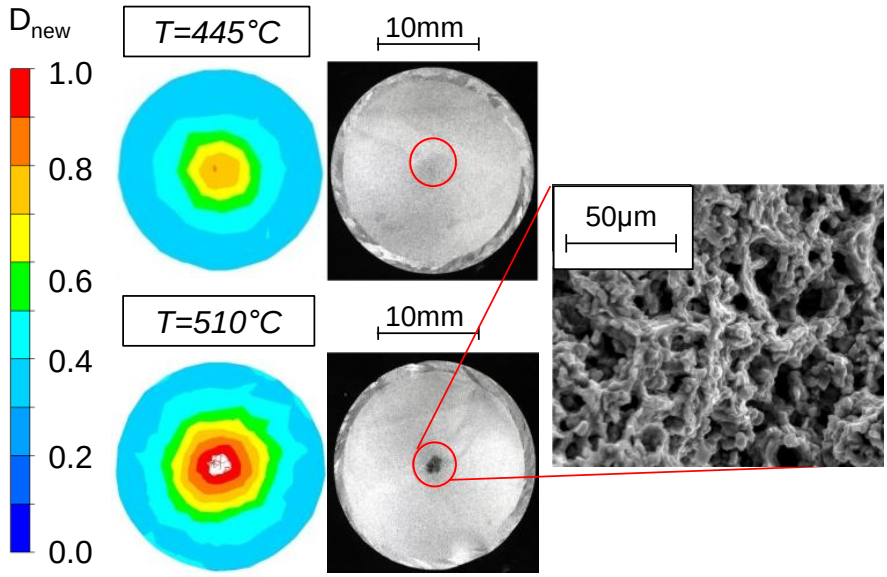

Figure 7. 2 - Validation results, crack prediction in the bar cross section.

These results prove that the developed material damage model is capable of correctly simulating the damage evolution during the process and in particular to:

- model the damage evolution in varying thermo-mechanical conditions, since its formulation allows to keep into account the effect that the thermal variables have on damage and thus representing the part thermal history;
- correctly predict the crack onset even when the thermal and strain rate paths evolve through regimes that activate microstructural changes that affect the material fracture mode;
- provide the model validation on industrial trials and not only on laboratory validation tests;

Besides this qualitative validation on the fracture onset prediction, which yet is probably the main industrial concern, a more accurate validation is here provided by using the two most representative and quantitative parameters that can be easily measured: the crack tip position and length. In Figure 7.3 a benchmark is provided between:

- actual crack length, as measured by the resulting part from Trial B;
- crack length as predicted by the empirical fracture criterion;
- crack length as predicted by the novel physically based criterion.

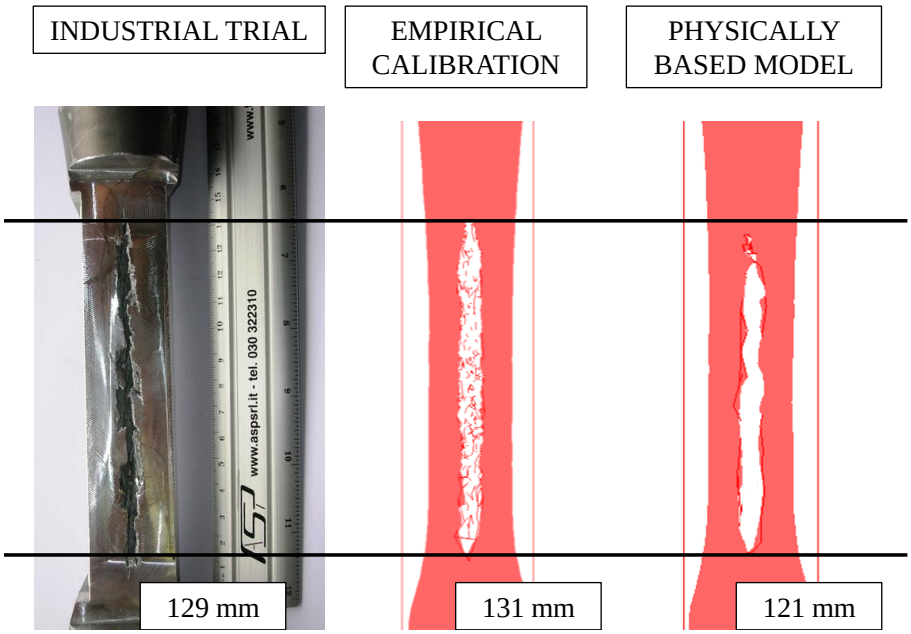

Figure 7. 3 – Crack length benchmark for the Trial B trial conditions.

The results show that:

- the empirical criterion provides excellent validation, since the difference with the experimental datum is less than 2%, which is probably less than process repeatability and also close to the intrinsic accuracy of a FE numerical simulation;
- the physically-based approach also provides good prediction of the crack geometrical features, although underestimating by ≈ 6% the crack length. This is anyway a very good result and can be easily explained by the fact that, as seen in Chapter 6, the new model slightly underestimates the damage for the highest process temperatures.

VII.3 APPLICATION TO PROCESS MAPS ELABORATION

As introduced in the first paragraph, there are two ways by which the industrial application of this criterion could be carried out:

- *process maps derivation*; which essentially consists in carrying out an extensive numerical campaign varying the input process parameters to define the process formability map. This is essentially the main way to pass from a *material formability map*, which can usually be found in technical handbooks or in the

scientific literature, to the *process formability map*, which, being process dependent, does not exist and is often replaced by wise industrial practice or expensive industrial trials. If carried out with accuracy, these process maps can be of huge industrial interest for process variables tuning;

- *process intelligent re-design*; in case of process structural modifications (e.g. dies re-design), the use of properly calibrated FE simulations can be a very useful tool for technical design choices.

A brief example of the application of the first technique is showed below: assuming for ease sake that only two process variables could be changed, namely the furnace temperature and the rolls rotation speed, the numerical campaign summarized in Table 7. 2 is defined.

Process variable	**Tested values**
Furnace temperature [°C]	445, 470, 490, 510
Rolls rotation speed [rpm]	1, 3, 5, 8

Table 7. 2 – Process map definition numerical campaign plan.

The results of the numerical campaign are illustrated in Figure 7.4. The values highlighted in the boxes correspond to the final damage value, following the new developed approach. The red crosses indicate axial cracking, thus no damage level is provided. Green boxes are defined for damage ≤ 0.7.

This process map is indicative of the capability of such a method, since two "green boxes" result for process condition which are not close. This is due to the non-linear interactive influence of temperature and strain rate (higher strain rate entails higher heating for friction and plastic deformation energy, while lower strain rate entails higher convection cooling).

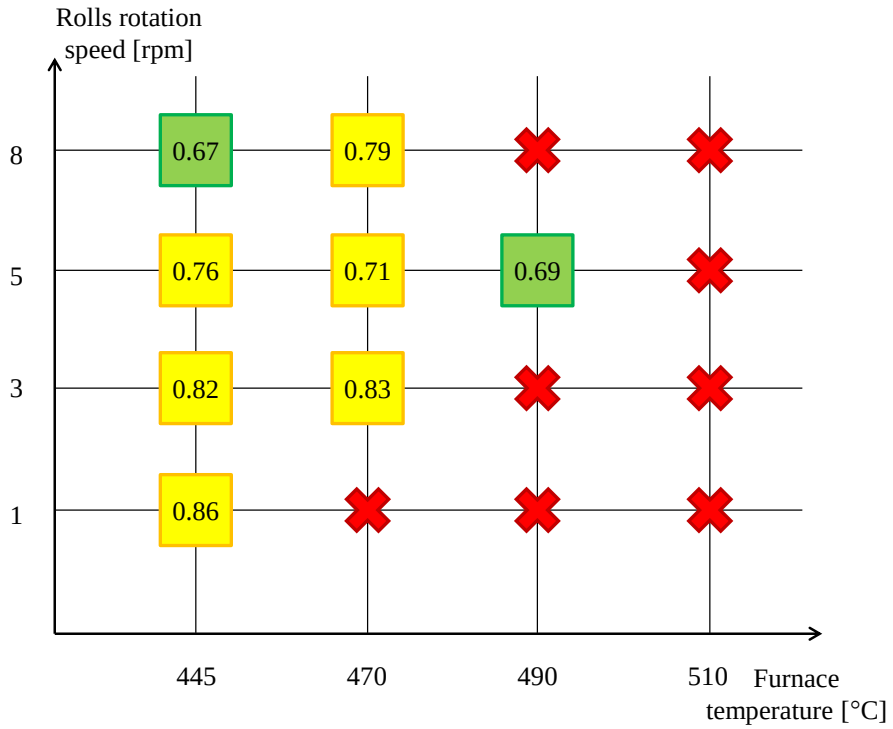

Figure 7. 4 – Example of process formability map.

As a last consideration, this approach, adopted systematically with a higher simulations number, would lead to the definition of *iso-damage* curves on the process map.

VIII CHAPTER

CONCLUSIONS

The objective of the present work has been the development of a new ductile fracture criterion for hot processes. The technical and scientific literature review highlighted that hot damage modelling has still substantial lacks in terms of representative capabilities and, probably due to the phenomenon complexity, it is still usually faced either by empirical approaches or by analytical formulations which are quite simple and are not capable to capture complex microstructure-driven fracture mode changes.

The present work provides a possible answer to these lacks by formulating a new hot fracture criterion with the following characteristics:

- explicit dependence of the formulation by temperature and strain rate; this feature allows keeping into account the thermal evolution into the damage history of the material, implying a *temperature path dependent* damage formulation;
- the extensive use in the damage model of material physical parameters; this feature provides the double advantage of allowing a deeper physical insight in the damage phenomenon and an easier model calibration, avoiding complex and unrepresentative numerical regressions as well as risky data extrapolations;
- ease of experimental calibration, avoiding time expensive FE inverse analysis.

For all these reasons, then, this can be a tool of great industrial interest as well as an innovative scientific approach. One aspect that makes this model of additional industrial interest is the choice of the industrial study case and of the material:

- the cross wedge rolling process; since it is an increasingly used forming process that provides many technological advantages such as high productivity and little to no material waste, but which can show formability issues, linked with Mannesmann cracking, that are typically difficult to detect and expensive to be managed with trial-and-error process variable tuning;
- the AA6082-T6 alloy; since it is one of the most common precipitation hardened Al-base alloys that are increasingly being employed in many industrial applications and in particular in the automotive sector. In this respect, the experimental evidences provided on the microstructural reasons of the material formability behaviour, and in particular the *negative strain rate sensitivity*, together with the similar behaviours found in literature for other precipitation hardened Al-base alloys, make this approach suitable at least for all this category of materials.

The validity of the proposed approach was finally assessed in two ways:

- *fracture criterion validation*; which was carried out comparing the model crack predictions with the industrial trials results and also with the numerical

predictions of an empirical approach (which provides by definition a best fitting on the experimental tests);

- *fracture criterion application*; in which an example of the systematic use of the model in the FE process simulation can be used either to develop formability windows in terms of process parameters, useful for process tuning, or as a tool for intelligent re-design.

.

REFERENCES

[1] E. Tekkaya, *A guide for validation of FE-simulations in bulk metal forming*, The Arabian Journal for Science and Engineering, 30 1C (2005) 113–136.

[2] VV. AA., 2001. *ASM Specialty Handbook – Copper and Copper Alloys*, pag. 454, 1st ed., ASM International, United States of America.

[3] VV. AA., 2003. *Handbook of aluminum – Vol. 1*, pag. 825, 10th ed., Marcel Dekker Inc., United States of America.

[4] T. Wierzbicki, Y. Bao, Y. Lee, Y. Bai, *Calibration and evaluation of seven fracture models*, International Journal of Mechanical Sciences, 47 (2005) 719–743.

[5] Y. Zhu, W. Zeng, F. Zhang, Y. Zhao, X. Zhang, K Wang, *A new methodology for prediction of fracture initiation in hot compression of Ti40 titanium* alloy, Materials Science and Engineering, A 553 (2012) 112–118.

[6] Q. Li, M. R. Lovell, W. Slaughter, K. Tagavi, *Investigation of the morphology of internal defects in cross wedge rolling*, Journal of Materials Processing Technology, 125–126 (2002) 248–257.

[7] VV. AA., 2002. *ASM Handbook – Vol. 11 Faiulure analysis and prevention*, 1st ed., ASM International, United States of America.

[8] VV. AA., 1987. *ASM Handbook – Vol. 12 Fractography*, 9th ed., ASM International, United States of America.

[9] T.L. Anderson, 1995. *Fracture Mechanics: Fundamentals and Applications*, 2nd ed., CRC Press.

[10] S. Fanini, 2008. *Modelling of the Mannesmans effect in tube piercing*, Ph.D. Thesis, University of Padua.

[11] P.W., Bridgman, 1952. *Studies in large plastic flow and fracture*. McGraw-Hill.

[12] Margevicius R. W., Lewandowski J. J., *The influence of hydrostatic pressure on fracture of single-crystal and polycrystalline NiAl*. Metallurgical and Material Transactions A 25A (1994) 1457–70.

[13] Liu D. S., Lewandowski J. J., *The effects of superimposed hydrostatic pressure on deformation and fracture: Part I. Monolithic 6061 aluminum*. Metallurgical and Material Transactions A 24A (1993) 601–8.

[14] Liu D. S., Lewandowski J. J., *The effects of superimposed hydrostatic pressure on deformation and fracture: Part II. Particulate reinforced 6061 composites*. Metallurgical and Material Transactions A 24A (1993) 609–15.

[15] Kao A. S., Kuhn H. A., Richmond O., Spitzig W. A., *Tensile fracture and fractographic analysis of 1045 spheroidized steel under hydrostatic pressure*. Journal of Materials Research 5 (1990) 83–91.

[16] Y. Bao, T. Wierzbicki, *On the cut-off value of negative triaxiality for fracture*. Engineering Fracture Mechanics 72 (2005) 1049–1069.

[17] J. W. Hancock, A. C. Mackenzie, *On the mechanisms of ductile failure in high-strength steels subjected to multi-axial stress-states*. Journal of the Mechanics and Physics of Solids 24 (1976) 147–160.

[18] G. R. Johnson, W. H. Cook, *Fracture characteristics of three metals subjected to various strains, strain rates, temperatures and pressures*. Engineering Fracture Mechanics 70 (1985) 31–48.

[19] Y. Bao, T. Wierzbicki, *On fracture locus in the equivalent strain and stress triaxiality space*. International Journal of Mechanical Sciences 46 (2004) 81–98.

[20] Y. Bao, T. Wierzbicki, *A Comparative Study on Various Ductile Crack Formation Criteria*. Journal of Engineering Materials and Technology 126 (2004) 314–324.

[21] Barsoum, J. Faleskog, *Rupture mechanisms in combined tension and shear—Micromechanics*. International Journal of Solids and Structures 44 (2007) 5481–5498.

[22] L. Xue, *Damage accumulation and fracture initiation in uncracked ductile solids subject to triaxial loading*. International Journal of Solids and Structures 44 (2007) 5163–5181.

[23] J. Faleskog, I. Barsoum, *Tension–torsion fracture experiments - Part I: Experiments and a procedure to evaluate the equivalent plastic strain*. International Journal of Solids and Structures 50 (2013) 4241–4257.

[24] G. E. Dieter, 1988. *Mechanical metallurgy*, McGraw-Hill, United Kingdom.

[25] Zenner, J. H. Hollomon, *Effect of strain rate upon plastic flow of steel*. Journal of applied physics 15 (1944) 22–32.

[26] J. Rösler, H. Harders, M. Bäker, 2007. *Mechanical Behaviour of Engineering Materials*, Springer-Verlag, Berlin Heidelberg.

[27] Z. Jin, A. Beaudoin, T. A. Bieler, B. Radhakrishnan, 2003. *Hot deformation of Aluminum Alloys III, Deformation and failure mechanisms in commercial AA5083 materials*, TMS.

[28] J. Chang, K. Takata, K. Ichitani , E. M. Taleff, *Ductility of an aluminum–4.4 wt. pct. magnesium alloy at warm and hot working temperatures*. Materials Science and Engineering A 527 (2010) 3822–3828.

[29] S. Alexandrov, P.T. Wang, R.E. Roadman, *A fracture criterion of aluminum alloys in hot metal forming*. Journal of Materials Processing Technology 160 (2005) 257–265.

[30] VV. AA., 1993. *ASM Handbook – Vol. 14 Forming and forging*, 3rd ed., ASM International, United States of America.

[31] G. E. Dieter, 1984. *Workability Testing Technique,* American Society for Metals.

[32] VV. AA., 1978. *Mechanics of sheet metal forming*, 1st ed., Plenum Press, New York-London.

[33] R. H. Wagoner, J.-L. Chenot, 2001. *Metal forming analysis*, Cambridge University Press.

[34] M. G. Cockroft D. J. Latham, *Ductility and the workability of metals*. Journal of the institute of metals 96 (1968) 33.

[35] J. Lemaitre, 1996. *A course on damage mechanics*, 2nd ed., Springer.

[36] S. Oh, C. Chen, S. Kobayashi, *Ductile failure in axi-symmetric extrusion and drawing*. Journal of Material Science and Engineering 101 (1979) 23–44.

[37] P. Brozzo, B. Deluca, R. Rendina, *A New Method for the Prediction of Formability Limits in Metal Sheets, Sheet Metal Forming and Formability*. Proceedings of the Seventh Biennial Conference of the International Deep Drawing Research Group, 1972.

[38] F. A. Freudenthal, 1950. *The Inelastic Behaviour of Solids.* Wiley, New York.

[39] F. A. McClintock, *A criterion for ductile fracture by the void growth*. Journal of applied Mechanics 35/2 (1968) 363–371.

[40] J. R. Rice, D. M. Tracey, *On the ductile enlargement of voids in triaxial stress fields*. Journal of the Mechanics and Physics of Solids 17 (1969) 201–217.

[41] M. Oyane, *Criteria For Ductile Fracture Strain*. Bull. JSME 15 (1972) 1507.

[42] M. Oyane, T. Sato, K. Okimoto, S. Shima, *Criteria for Ductile Fracture and Their Applications*. Journal of Mechanical Working Technology 4 (1980) 65-81.

[43] P. P. A. Gouveia, J. M. C. Rodrigues, P. A. F. Martins, *Fracture Predicting in Bulk Metal Forming*. International Journal of Mechanical Sciences 38-4 (1996) 361-372.

[44] B. P. P. A. Gouveia, J. M. C. Rodrigues, P. A. F. Martins, *Ductile Fracture in Metalworking: Experimental and Theoretical Research*. Journal of Materials Processing Technology 101 (2000) 52-63.

[45] K. Komori, *Effect of Ductile Fracture Criteria on Chevron Crack Formation and Evolution in Drawing*. International Journal of Mechanical Sciences 45 (2003) 141-160.

[46] Gurson, *Continuum Theory of Ductile Rupture by Void Nucleation and Growth: Part I – Yield Criteria and Flow Rules for Porous Ductile Media*. Journal of Engineering Materials and Technology 99 (1977) 2.

[47] V. Tvergaard, *Influence of Voids on Shear Band Instabilities Under Plane Strain Conditions*. Internation Journal of Fracture 17 (1981) 389.

[48] V. Tvergaard, A. Needleman, *Analysis of Cup-cone Fracture in Round Tensile Bar*. Acta Metallurgica 32 (1984) 157.

[49] J. Lemaitre, *A continuous damage mechanics model for ductile fracture*. Journal of Engineering Materials and Technology 107 (1985) 83.

[50] J. Lemaitre, R. Desmorat, 2005. *Engineering damage mechanics*, Springer.

[51] L. M. Kachanov, *Rupture Time Under Creep Conditions*. International Journal of Fracture 97 (1999) 11-18.

[52] N. Bonora, *A nonlinear CDM model for ductile failure*. Engineering Fracture Mechanics 58 (1997) 11-28.

[53] P.-O. Bouchard, L. Bourgeon, S. Fayolle, K. Mocellin, *An enhanced Lemaitre model formulation for materials processing damage computation*. International Journal of Material Forming 4 (2011) 299-315.

[54] M. L. Wilkins, R. D. Streit, J. E. Reaugh, *Cumulative-strain-damage model of ductile fracture: simulation and prediction of engineering fracture tests.* Technical Report UCRL-53058, Lawrence Livermore National Laboratory, 1980.

[55] L. Xue, T. Wierzbicki, *Ductile fracture initiation and propagation modelling using damage plasticity theory*. Engineering Fracture Mechanics 75 (2008) 3276–3293.

[56] von Lode, W., *Versuche uber den einflub der mittleren hauptspannug auf die fliebgrenze*. Zeitschrift fur angewandte mathematic und mechanik 5 (2) (1925) 142–144.

[57] T. Coppola, L. Cortese, P. Folgarait, *The effect of stress invariants on ductile fracture limit in steels.* Engineering Fracture Mechanics 76 (2009) 1288–1302.

[58] M. Simionato, 2009. *Damage modelling in cold forging process chains*, Ph.D. Thesis, University of Padua.

[59] P. F. Bariani, S. Bruschi, A. Ghiotti, M. Simionato, *Ductile fracture prediction in cold forging process chains.* CIRP Annals - Manufacturing Technology 60 (2011) 287–290.

[60] S. M. Graham, T. Zhang, X. Gao, M. Hayden, *Development of a combined tension–torsion experiment for calibration of ductile fracture models under conditions of low triaxiality.* International Journal of Mechanical Sciences 54 (2012) 172–181.

[61] Y. Bai, T. Wierzbicki, *Application of extended Mohr-Coulomb criterion to ductile fracture.* International Journal of Fracture 161 (2010) 1-20.

[62] Y. Lou, H. Huh, S. Lim, K. Pack, *New ductile fracture criterion for prediction of fracture forming limit diagrams of sheet metals* . International Journal of Solids and Structures 49 (2012) 3605–3615.

[63] Y. Lou, H. Huh, *Extension of a shear-controlled ductile fracture model considering the stress triaxiality and the Lode parameter*. International Journal of Solids and Structures 50 (2013) 447–455.

[64] Y. Lou, J. W. Yoon, H. Huh, *Modeling of shear ductile fracture considering a changeable cut-off value for stress triaxiality.* International Journal of Plasticity 54 (2014) 56–80.

[65] X. Zhang, W. Zeng, Y. Shu, Y. Zhou, Y. Zhao, H. Wu, H. Yu, *Fracture criterion for predicting surface cracking of Ti40 alloy in hot forming processes*. Transactions of Nonferrous Metals Society of China 19 (2009) 267-271.

[66] O. V. Bocharov, A. M. Galkin, A. A. Kabanov, D. D. Sinel'nikov, *Formability of an aluminium alloy at high temperatures*, Tsvetnye Metally 6 (1997) 57 (in Russian).

[67] S. Khan, H. Liu, *Strain rate and temperature dependent fracture criteria for isotropic and anisotropic metals*. International Journal of Plasticity 37 (2012) 1–15.

[68] S. Khan, H. Liu, *Deformation induced anisotropic responses of Ti-6Al-4V alloy. Part I: Experiments*. International Journal of Plasticity 38 (2012) 1-13.

[69] J. He, Z. Cui, F. Chen, Y. Xiao, L. Ruan, *The new ductile fracture criterion for 30Cr2Ni4MoV ultra-super-critical rotor steel at elevated temperatures.* Materials and Design 52 (2013) 547–555.

[70] G. Mrówka-Nowotnik, J. Sieniawski, M. Wierzbińska, *Analysis of intermetallic particles in AlSi1MgMn aluminium alloy.* Journal of achievements in materials and manufacturing engineering 20 (2007) 155-158.

[71] G. Mrówka-Nowotnik, *Damage mechanism in AlSi1MgMn alloy*. Archives of material science and engineering. 29 2 (2008) 93-96.

[72] G. Mrówka-Nowotnik, *The effect of intermetallics on the fracture mechanism in AlSi1MgMn alloy*. Journal of achievements in materials and manufacturing engineering 30 1 (2008) 35-42.

[73] Lassance, D. Fabregue, F. Delannay, T. Pardoen, *Micromechanics of room and high temperature fracture in 6xxx Al alloys*. Progress in Materials Science 52 (2007) 62–129.

[74] P. F. Bariani, S. Bruschi, A. Ghiotti, F. Michieletto, *Hot stamping of AA5083 aluminium alloy sheets*. CIRP Annals - Manufacturing Technology 62 (2013) 251–254.

[75] Z.H. Hu, X.H. Xu, D.Y. Sha, 1985. *Skew Rolling and Cross Wedge Rolling—Principles*, Processes and Machines, Metallurgy and Industry Press, Beijing, China.

[76] W. Johnson, A.G. Mamalis, *A survey of some physical defects arising in metal working processes*. Proceedings of the 17th International MTDR Conference London UK 1977 607–621.

[77] Z. Pater, *A study of cross wedge rolling process*. Journal of Materials Processing Technology 80 (1998) 370–375.

[78] Z. Pater, *Theoretical and experimental analysis of cross wedge rolling process.* International Journal of Machine Tools & Manufacture 40 (2000) 49–63.

[79] Z. Pater, *Tools optimisation in cross-wedge rolling.* Journal of Materials Processing Technology 138 (2003) 176–182.

[80] T. Awano, A. Danno, *Metal flow on rolled shafts — a study of hot rolling of stepped shaft: Part 1*. J. JSTP 88 (1968) 285–295.

[81] G. Fang, L. P. Lei, P. Zeng, *Three-dimensional rigid-plastic finite element simulation for the two-roll cross-wedge rolling process.* Journal of Materials Processing Technology 129 (2002) 245-249.

[82] H. W. Lee, G. A. Lee, D. J. Yoon, S. Choi, K.H. Na, M. Y. Hwang, *Optimization of design parameters using a response surface method in a cold cross-wedge rolling.* Journal of Materials Processing Technology 201 (2008) 112–117.

[83] G. Liu, Z. Zhong, Z. Shen, *Influence of reduction distribution on internal defects during cross wedge-rolling process.* Procedia Engineering 81 (2014) 263 – 267.

[84] M. L. N. Silva, G. H. Pires, S. T. Button, *Damage evolution during cross wedge rolling of steel DIN 38MnSiVS5*. Procedia Engineering 10 (2011) 752–757.

[85] Forge ® User's Manual, Transvalor.

[86] ASTM E8-96a, *Standard Test Methods for Tension Testing of Metallic Materials.*

[87] ASTM E21-92, *Standard Test Methods for Elevated Temperatures Tension Test of Metallic Materials*.

[88] VV. AA., 1991. *ASM Handbook – Vol. 4 Heat treating*, 1st ed., ASM International, United States of America.

[89] J. Zhang, Z. Fan, Y. Q. Wang, B. L. Zhou, *Equilibirum pseudobinary Al-Mg_2Si phase diagram.* Materials Science and Technology 17 (2001) 494-496.